THE EFFECT OF PARTICLE DEFORMATION ON THE RHEOLOGY AND MICROSTRUCTURE OF NONCOLLOIDAL SUSPENSIONS

A Thesis
Presented to
The Academic Faculty

by

Jonathan R. Clausen

In Partial Fulfillment
of the Requirements for the Degree
Doctor of Philosophy in the
School of Mechanical Engineering

Georgia Institute of Technology
August 2010

THE EFFECT OF PARTICLE DEFORMATION ON THE RHEOLOGY AND MICROSTRUCTURE OF NONCOLLOIDAL SUSPENSIONS

Approved by:

Dr. Cyrus Aidun, Advisor
School of Mechanical Engineering
Georgia Institute of Technology

Dr. Marc Smith
Mechanical Engineering
Georgia Institute of Technology

Dr. G. Paul Neitzel
Mechanical Engineering
Georgia Institute of Technology

Dr. Victor Breedveld
Chemical and Bioengineering
Georgia Institute of Technology

Dr. Jeffrey Morris
Chemical Engineering
The City College of New York

Date Approved: June 2010

ACKNOWLEDGEMENTS

I would like to thank my advisor, Dr. Cyrus Aidun, and my committee for their guidance and input on my research. I would also like to thank the many excellent colleagues I had the opportunity to work with while at Georgia Tech. These include Robert MacMeccan, whose help during the early development of the simulation method was indispensable, and Daniel Reasor, whose help in porting the method to large-scale supercomputers was greatly appreciated. I would also like to thank the National Science Foundation's support through TeraGrid grant TG-CTS100012 using resources provided by Purude, the Texas Advanced Computing Center, and LSU.

TABLE OF CONTENTS

LIST OF TABLES

LIST OF FIGURES

LIST OF SYMBOLS OR ABBREVIATIONS

ANL	Argonne National Lab
BGP	BlueGene/P
FE	Finite element
GB	Gigabytes
HPC	High performance computing
LB	Lattice-Boltzmann
MB	Megabytes
MPI	Message Passing Interface
a	Particle radius
A_c	Contact scaling constant
A_{ij}	Jeffery's coefficients in matrix form
c	Lattice-Boltzmann spacing
c_s	Lattice-Boltzmann pseudo sound speed
C	Finite element damping matrix
Ca_G	Capillary number
$\mathrm{Ca}_{G,\mathrm{eff}}$	Effective capillary number
df	Link-wise lubrication force proposed by Ding & Aidun (2003)
dF_{lub}	Link-wise correction to lubrication force
D	Diffusion tensor
D_{xy}	Taylor-deformation parameter
$\boldsymbol{e}_i$	Lattice-Boltzmann discrete velocity vectors
E	Rate of strain tensor
E_b	Reduced bending ratio
E_y	Young's modulus

f_i	Lattice-Boltzmann fluid distribution function
$f_i^{(eq)}$	Equilibrium lattice-Boltzmann fluid distribution function
f_i^{GS}	Lattice-Boltzmann distribution adjusted to correct Galilean invariance
$f_i^{\Delta\rho}$	Density correction to lattice-Boltzmann nodes
$f_i^{\Delta P}$	Pressure correction to conserve particle
$\boldsymbol{F}$	Finite element force vector
$\boldsymbol{F}^b$	Body stresses
$\boldsymbol{F}^{(b)}$	Bounce-back force
$\boldsymbol{F}^{link}$	Force on a given boundary link
$\boldsymbol{F}^{(c)}$	Force associated with node (un)covering
F_{lub}	Lubrication force from two approaching spheres (Cox, 1974)
$\boldsymbol{F}^{total}$	Summed force on particle
$\boldsymbol{F}^{tr}$	Traction forces on the surface
$\boldsymbol{F}^{(err)}$	Force error caused by Galilean effects
g	Gap between particles for a given surface element
g'	Gap along a given lattice link
$g(\boldsymbol{r})$	Pair distribution function
g_c	Contact scaling constant
g_{grav}	Gravity acceleration
g_α, g'_α, g''_α	Integral types found in Jeffery (1922)
G_M	Membrane shear modulus
G_S	Solid shear modulus
H	Height of domain
H_i	Finite element shape function
$\mathbf{I}$	Identity matrix
$\mathbf{I}^{inertia}$	Inertial tensor
$\boldsymbol{j}$	Particle flux

k_B	Boltzmann's constant
K	Finite element stiffness matrix
l_{FEA}	Average finite element edge length
$\boldsymbol{n}_{avg}$	Average surface normal
N	Number of particles
N_1	First normal stress difference
N_2	Second normal stress difference
N_{se}	Shearoelastic number
M	Finite element mass matrix
Ma	Lattice-Boltzmann Mach number
p_o	Far-field pressure
$P_{1\|1}(\boldsymbol{r})$	Probability of finding particle at $\boldsymbol{r}$ given a particle at the origin
P_f	Fluid pressure
$\bar{q}$	Lubrication weighting coefficient
$\boldsymbol{r}$	Position vector
$\boldsymbol{r}_0$	Particle center of mass
$\boldsymbol{s}$	Vector connecting finite element surfaces
S	Particle stresslet
$\boldsymbol{S}$	Finite element natural coordinates
$\boldsymbol{S}^{(err)}$	Stresslet error caused by Galilean effects
t	Time
T_i	Surface forces on ellipsoid
$\boldsymbol{T}_{surf}$	Tangent vector to the surface
$\boldsymbol{T}^{total}$	Summed torque on particle
$\boldsymbol{T}_V$	Torque per unit volume
$\mathcal{T}$	Lattice-Boltzmann time steps/second
$\boldsymbol{u}^{\infty}$	Ambient flow field

U_{app}	Approach velocity
$\boldsymbol{u}_b$	Boundary velocity
$\boldsymbol{U}$	Particle translational velocity
U_s	Velocity scale
V	Domain volume
V_p	Volume of particle
w_i	Lattice-Boltzmann direction weights
$\boldsymbol{x}$	Finite element nodal displacement
$\dot{\boldsymbol{x}}$	Finite element nodal velocity
$\ddot{\boldsymbol{x}}$	Finite element nodal acceleration
$\bar{\boldsymbol{X}}$	Elemental virtual displacements
α_D	Rayleigh damping coefficient
β_n	Newmark's method coefficient
β_D	Rayleigh damping coefficient
$\dot{\gamma}$	Shear rate
γ_n	Newmark's method coefficient
Δt	Time discretization for numerical simulation
$\bar{\boldsymbol{\epsilon}}$	Elemental virtual strains
ε	Gap between particles
η_r	Spin viscosity
θ	Orientation angle of particle
κ_b	Bending modulus
λ	Curvature parameter
μ	Fluid viscosity
$[\mu]$	Intrinsic viscosity
μ_{eff}	Effective viscosity
μ_r	Relative viscosity

ν_p	Poisson Ratio
Π_p	Particle pressure
ρ	Density
ρ_s	Solid density
$\boldsymbol{\sigma}$	Local stress tensor
$\boldsymbol{\sigma}_{\mathbf{p}}$	Local stress in solid phase
$\boldsymbol{\Sigma}$	Stress in the suspension
$\boldsymbol{\Sigma}^f$	Stress in the fluid phase
$\boldsymbol{\Sigma}^p$	Stress in the particle phase
τ	Lattice-Boltzmann relaxation time
ϕ	Volume fraction
ϕ_m	Maximum packing fraction
ω_n	Modal circular frequency
$\boldsymbol{\Omega}^\infty$	Ambient flow vorticity
$\boldsymbol{\Omega}$	Particle angular velocity

SUMMARY

In order to study suspensions of deformable particles, a hybrid numerical technique was developed that combined a lattice-Boltzmann (LB) fluid solver with a finite element (FE) solid-phase solver. The LB method accurately recovered Navier-Stokes hydrodynamics, while the linear FE method accurately modeled deformation of fluid-filled elastic capsules for moderate levels of deformation. The LB/FE technique was extended using the Message Passing Interface (MPI) to allow scalable simulations on leading-class distributed memory supercomputers.

An extensive series of validations were conducted using model problems, and the LB/FE method was found to accurately capture proper capsule dynamics and fluid hydrodynamics. The dilute-limit rheology was studied, and the individual normal stresses were accurately measured. An extension to the analytical theory of Roscoe (1967) for viscoelastic spheres was proposed that included the isotropic pressure disturbance found in the solution of Jeffery (1922). Single-body deformation was found to have a small negative (tensile) effect on the particle pressure.

Next, the rheology and microstructure of dense suspensions of elastic capsules were probed in detail. As elastic deformation was introduced to the capsules, the rheology exhibited rapid changes. Moderate amounts of shear thinning were observed, and the first normal stress difference showed a rapid increase from a negative value for the rigid case, to a positive value for moderate levels of deformation. The particle pressure also demonstrated a decrease in compressive stresses as deformation increased. The corresponding changes in microstructure were quantified. Changes in particle self-diffusivity were also noted.

CHAPTER I

INTRODUCTION

1.1 Motivation

Particle suspensions play an important role in many industrial and biological situations as varied as paper slurries, arterial flow, and cosmetics. Even though the particles may be suspended in a Newtonian fluid, the resultant suspension exhibits much more complex and non-Newtonian flow characteristics. For example, suspensions of deformable particles are shear-thinning, not unlike colloidal suspensions. Also, normal stresses play a more prominent role and can create concentration gradients in the suspended phase. Understanding the complex rheology of these suspensions is important in optimization of industrial processes, reduction of cost and waste, and in the biological case, saving lives.

The analytical description of suspensions is confined primarily to the dilute limit, where only the effect of two-body interactions is considered. For a hard-sphere suspension, Einstein (1906, 1911) derived the dilute limit effect of volume concentration on suspension viscosity, and Batchelor & Green (1972a) extended this analysis for two-body interactions; however, strictly analytical work becomes intractable when the extension to dense, multibody interactions is attempted. Further understanding of particle suspensions requires using a combination of experimental techniques and numerical simulations, and the information garnered from these techniques must span the multiple scales inherent in a suspension. First, the macroscopic effect of the particles must be ascertained through rheological measurements such as suspension viscosity and stress under simplified flow conditions. Second, the microstructure of the suspension must be analyzed to understand the mechanistic effects driving the macroscopic changes in flow. Using these tools allows an advancement in the fundamental understanding of suspensions and the ability to create accurate constitutive models for suspension flow. The development of a novel method to simulate particle suspensions—particularly deformable particle suspensions—would advance the fundamental understanding of suspension rheology and microstructure.

The purpose of this research is to study the effect of elastically deformable capsules on the rheology and microstructure of noncolloidal suspensions. These capsules are filled with a Newtonian fluid and surrounded by an elastic membrane. Accordingly, a simulation technique has been developed that couples a lattice-Boltzmann (LB) method fluid and a finite-element (FE) analysis solid (MacMeccan et al., 2009). The LB method has been previously coupled to rigid particles, and the method offers an efficient framework for the inclusion of different solid-phase models, such as the FE model in this research. FE methods are a mature field in applications for solid mechanics and, with linear assumptions, can provide an efficient means for simulating motion and deformation. Corrections to the LB method are necessary to remove Galilean errors in the rheology calculations (Clausen & Aidun, 2009) and pressure errors caused by the pseudo-compressible nature of the LB method (Clausen & Aidun, 2010).

Several key contributions are made in this thesis, in addition to the development of the LB/FE simulation method. The particle pressure for a capsule in the dilute limit is accurately resolved (see also Clausen & Aidun, 2010). The analytical model of Roscoe (1967) is extended to model the particle pressure by including the appropriate isotropic pressure disturbance terms from Jeffery (1922). This research is the first to accurately simulate dense 3-dimensional capsule suspensions and recover bulk rheological properties. The transition in rheology from that of rigid spherical particles to deformable capsules is captured, even in the rapid transition seen in the near-rigid limit. The normal stresses, including the isotropic portion are recovered through simulation.

Correctly describing the normal stresses in capsule suspensions has a practical significance in understanding particle migration. Shear-induced migration is commonly seen in suspensions that have a gradient in shear and can create gradients in particle concentration. The suspension balance model (Nott & Brady, 1994) relates this migration along shear gradients to changes in particle-phase normal stresses; however, current studies using the suspension balance model have focused on suspensions of rigid spherical particles (Nott & Brady, 1994; Morris & Boulay, 1999; Deboeuf, Gauthier, Martin, Yurkovetsky & Morris, 2009). Describing the migration of deformable cells is of medical importance. For example, in blood flow, the transport of white blood cells and platelets from the core arterial flow to the wall region and the associated process of platelet deposition is being actively researched (Aarts et al., 1988; Konstantopoulos, Kukreti & McIntire, 1998; Freund, 2007; MacMeccan, 2007). This study is a starting point to understanding migration effects in deformable particle suspensions under the suspension balance framework.

Also, the impact of deformation on particle self-diffusion is examined, with the diffusion calculated for the shear-gradient and flow directions. The investigation of diffusion in deformable particle suspensions also has biological motivation because reduced mass transport has been implicated in the formation of atherosclerotic plaque (Ethier, 2002; Tarbell, 2003). Plaque formation, when it ultimately ruptures, causes myocardial infarction—a heart attack. Heart disease is the leading cause of death in the United States: one American dies of heart disease every minute (Lloyd-Jones et al., 2009).

1.2 Suspensions of rigid spherical particles

The relevant parameters in the simulation of rigid-sphere suspensions are the Péclet number, Pe, volume concentration, ϕ, and the particle Reynolds number, Re_p. Due to the small size of the suspended particles, in many situations inertial effects are negligible and Re_p is not a relevant parameter in determining suspension rheology and microstructure. For shear flow, the particle Reynolds number is defined by

$$\mathrm{Re}_p \equiv \frac{\rho\dot{\gamma}a^2}{\mu},$$

where a is the particle radius, ρ is the fluid density, μ is the fluid dynamic viscosity, and $\dot{\gamma}$ is the shear rate. With the assumption of incompressibility and $\mathrm{Re}_p \ll 1$, the flow is governed by the Stokes and continuity equations, shown as

$$\nabla P_f = \mu\nabla^2\boldsymbol{u}, \tag{1a}$$

$$\nabla\cdot\boldsymbol{u} = 0, \tag{1b}$$

where $\boldsymbol{u}$ is the fluid velocity and P_f is the fluid pressure.

The Péclet number characterizes the ratio of viscous to Brownian forces and is defined as

$$\mathrm{Pe} \equiv \frac{6\pi\mu\dot{\gamma}a^3}{k_B T},$$

where k_B is Boltzmann's constant, and T is the temperature. In the case of a rigid particle suspension only subject to Brownian motion, i.e., $\mathrm{Pe} = 0$, the suspension is referred to as colloidal, and the suspension microstructure is symmetric. This symmetry is a direct consequence of the reversibility of Stokes flow. For suspensions of rigid spherical particles, the microstructure is dictated entirely by the the pair-distribution function, $g(\boldsymbol{r})$, defined as

$$g(\boldsymbol{r}) \equiv \frac{P_{1|1}(\boldsymbol{r})}{n}, \tag{2}$$

where $P_{1|1}(\boldsymbol{r})$ describes the probability of finding another particle at position $\boldsymbol{r}$ assuming a particle resides at the origin, and n is the number density of particles (for example Morris & Katyal, 2002). As a result of the symmetry, the suspension behaves in a Newtonian manner, and the viscosity is only a function of the volume concentration, i.e., $\mu_r = \mu_r(\phi)$, where μ_r is the relative viscosity, defined as

$$\mu_r \equiv \frac{\mu_{eff}}{\mu},$$

and μ_{eff} is the effective or measured viscosity of the suspension. This behavior is commonly referred to as the low-shear viscosity (Stickel & Powell, 2005).

At finite Pe, hydrodynamic forces caused by the imposed flow create asymmetry in the pair-distribution function, which has been shown experimentally (Parsi & Gadala-Maria, 1987) and through numerical simulations (Phung, 1993; Morris & Katyal, 2002). The suspension microstructure begins to form sliding layers, leading to the phenomenon known as shear-thinning. The asymmetry in $g(\boldsymbol{r})$ causes measurable normal stress differences, also demonstrated in experiments by Gadala-Maria (1979), Zarraga et al. (2000), and in simulations by Phung, Brady & Bossis (1996). Both normal stress differences and shear-thinning, shown in the microstructure through asymmetry in the pair-distribution function, are non-Newtonian effects that cannot be described by a simple Newtonian fluid model. As Pe $\to \infty$, shear-thinning ceases, and the viscosity again becomes a function of only the volume fraction. This region is called the high-shear viscosity. As shear rates increase beyond this plateau, shear thickening of suspensions ensues, which has been shown experimentally (Hoffman, 1972; So, Yang & Hyun, 2001), and through computer simulations (Foss & Brady, 2000; Sierou & Brady, 2002). Figure 1 from Stickel & Powell (2005) shows the relative trends in relative viscosity as ϕ and $\dot{\gamma}$ are altered. The high- and low-shear viscosity plateaus are clearly shown, along with regions of shear thinning and shear thickening.

The simulations in this thesis are noncolloidal, i.e., the effects of Brownian motion are negligible. Mathematically this is expressed as $\mathrm{Pe}^{-1} \to 0$, i.e., the strictly hydrodynamic limit, and Batchelor & Green (1972b) have shown analytically that $g(\boldsymbol{r})$ is symmetric for rigid spherical particles in this limit, a result in qualitative disagreement with observations. A symmetric pair-distribution function implies Newtonian behavior, no self-diffusion, and negligible normal stress differences. Brady & Morris

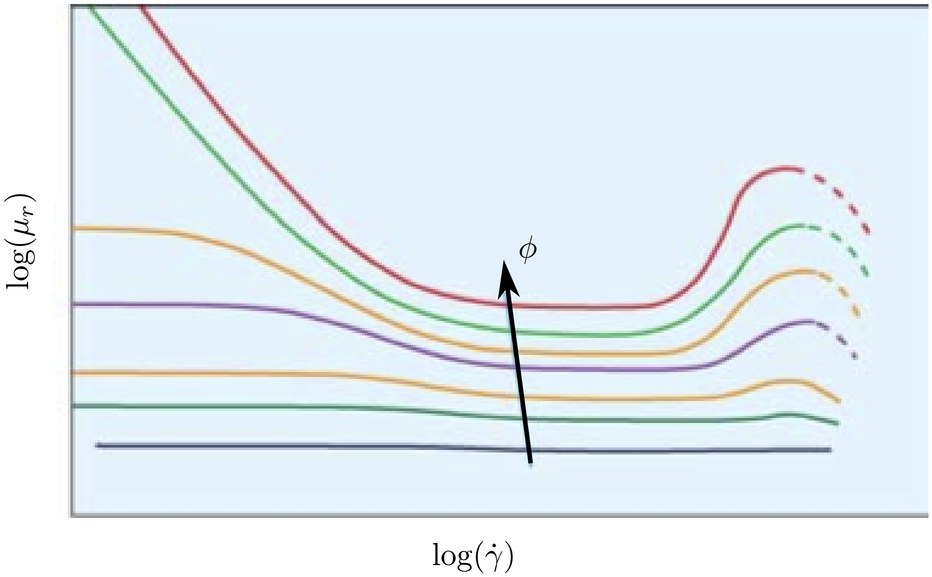

Figure 1: General trends in rigid-particle suspension viscosity as a function of the shear rate, $\dot{\gamma}$, and volume fraction, ϕ. Figure from Stickel & Powell (2005).

(1997) resolved this paradox with an asymptotic analysis showing the effect of residual Brownian motion existing in a boundary layer of size $O(a\mathrm{Pe}^{-1})$. This residual Brownian motion creates local asymmetry in $g(\boldsymbol{r})$, which is then propagated throughout the fluid. In the singular hydrodynamic case, the boundary layer decays resulting in a symmetric pair-distribution; however, any surface roughness or interparticle forces break this symmetry. This asymmetry can be seen in the pair distribution function obtained via Stokesian dynamics simulation of spherical particles, as shown in Figure 2. Eliminating all interparticle forces and having perfectly smooth particles is not possible in experiments, and can be difficult in simulations owing to numerical error and the singular nature of lubrication. As a direct consequence of this asymmetry, the interaction of particle pairs is nonconservative causing particles to cross streamlines, as opposed to the strictly hydrodynamic case analyzed by Batchelor & Green (1972b). The result is the well documented shear-induced self-diffusion in noncolloidal suspensions, which is shown experimentally (Breedveld, van den Ende, Jongschaap &

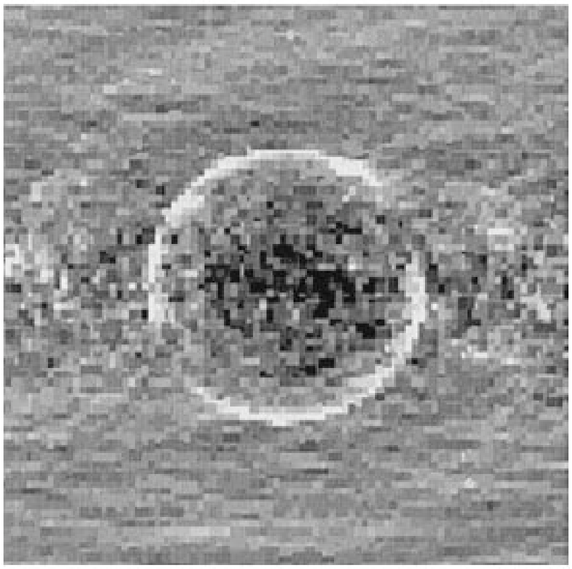

Figure 2: Asymmetry in the pair-distribution function from the simulation of monodisperse hard-sphere suspension at $\phi = 0.45$ and $\mathrm{Pe} = 10^5$; Brady & Morris (1997)

Mellema, 2001b; Breedveld, van den Ende, Bosscher, Jongschaap & Mellema, 2002), and through numerical simulations (Sierou & Brady, 2004).

Rigid particle motion is governed by Newton's equations of motion. In the cases examined here, particle inertia is negligible, thus the hydrodynamic force and torque on a suspended particle must be in balance with external forces, i.e., torque and force free. Owing to the no-slip fluid boundary condition on the suspended particles, the hydrodynamic force is shape dependent. For a rigid spherical particle in an unbounded domain, the relationship between hydrodynamic force and torque and particle velocity is given by Faxen's laws:

$$\left.\begin{aligned} \boldsymbol{F}^H &= 6\pi\mu a\left(1+\frac{a^2}{6}\nabla^2\right)\boldsymbol{u}^\infty - 6\pi\mu a\boldsymbol{U} \\ \boldsymbol{T}^H &= -8\pi\mu a^3\left(\boldsymbol{\Omega}^\infty - \boldsymbol{\Omega}\right) \end{aligned}\right\}, \tag{3}$$

where $\boldsymbol{u}^\infty$ is the ambient flow field, $\boldsymbol{\Omega}^\infty$ is the vorticity vector, $\boldsymbol{U}$ is the particle's translational velocity, and $\boldsymbol{\Omega}$ is the particle's angular velocity. Extension of these results to two spherical particles is analytically possible using a variety of methods including asymptotic analysis for small separations, multipole expansions, and singularity solutions (see Kim & Karilla, 1991, for review). The difficulty when attempting to use these techniques to describe a dense suspension comes in the many-body interactions which are dependent on the particle configuration.

1.3 Suspension rheology and normal stresses

Analysis of suspension rheology typically hinges on an averaging procedure to obtain the averaged averaged suspension stress, which is an average of both fluid and particles stresses in the suspensions. The averaged stress, using angle brackets to denote averages, can be written as

$$\langle \boldsymbol{\Sigma} \rangle = \left\langle \boldsymbol{\Sigma}^{f} \right\rangle + \langle \boldsymbol{\Sigma}^{p} \rangle , \tag{4}$$

where superscripts f and p refer to the fluid- and particle-phase stresses. Strictly speaking, the averaging procedure is an ensemble average, which is defined as averaging over all possible particle configurations, weighted by the probability that each configuration will occur. In situations where the stress is homogeneously distributed, for example in shear flow away from walls, the averaging over particle configurations can be simplified by replacing it with a volume average. Thus, the effective stress can be expressed as a volume integral of the form

$$\langle \boldsymbol{\Sigma} \rangle = \frac{1}{V} \int \boldsymbol{\sigma} \, dV,$$

where V is the domain volume and $\boldsymbol{\sigma}$ is the local stress (either fluid or solid). Following the analysis of Batchelor (1970), the integration can be split into regions of fluid and regions occupied by the solid particles. After using the divergence theorem to replace the volume integrals over the particles with appropriate surface integrals, replacing the stress in the fluid phase with the constitutive relationship for a Newtonian fluid, and neglecting inertial terms, the suspension stress can be written as

$$\langle \boldsymbol{\Sigma} \rangle = -\langle P_f \rangle \mathbf{I} + 2\mu \langle \mathbf{E} \rangle + \frac{1}{V} \sum_{i=1}^{N} \mathbf{S}, \tag{5}$$

where $\mathbf{I}$ is the identity matrix, $\mathbf{E}$ is the rate of strain tensor, N is the number of particles, and $\mathbf{S}$ is the particle stresslet, which is the symmetric portion of the first moment of the traction vectors on the particle surface . Using summation notation, the particle stresslet, $\mathbf{S}$, is given by

$$S_{ij} = \int_A \frac{1}{2} \left(\sigma_{ik} n_k r_j + \sigma_{jk} n_k r_i \right) - \mu \left(u_i n_j + u_j n_i \right) \, dA, \tag{6}$$

where $\boldsymbol{n}$ is a surface normal vector. Equation (5) can be nondimensionalized by scaling the lengths by the particle radius, time by the inverse shear rate, and stresses by the viscous stress in the suspension ($\mu\dot{\gamma}$) to give

$$\langle \boldsymbol{\Sigma}^* \rangle = - \left\langle P_f^* \right\rangle \mathbf{I} + 2 \left\langle \mathbf{E}^* \right\rangle + \phi \left\langle \mathbf{S}^* \right\rangle , \tag{7}$$

where starred quantities are dimensionless. Note, the traction vectors $\sigma_{ik} n_k$ are external to the capsule, i.e., the surface of integration lies just outside the particle border, and membrane tension effects are properly captured within this term and do not need to be handled explicitly (Batchelor, 1970). Alternate formations of (6) exist that account for the stress discontinuity of the membrane directly (see for example Ramanujan & Pozrikidis 1998). Angled brackets will be dropped for the rest of this thesis for clarity, with the averaging procedure implied.

The components of the effective stress tensor are related to the common rheological quantities of interest. The relative suspension viscosity can be expressed as

$$\mu_r = \frac{\Sigma_{12}}{\mu \dot{\gamma}} = \Sigma_{12}^* = \Sigma_{12}^* = 1 + \phi \left\langle S_{12}^* \right\rangle , \tag{8}$$

where S_{12}^* is called the intrinsic viscosity, denoted $[\mu]$, of a suspension, and was determined to be 5/2 for an isolated sphere (Einstein, 1911). The intrinsic viscosity frequently enters into empirical relationships for the viscosity of suspensions, such as the Krieger–Dougherty relationship (Krieger & Dougherty, 1959),

$$\mu_r = \left(1 - \frac{\phi}{\phi_m} \right)^{-[\mu]\phi_m} \tag{9}$$

where ϕ_m is the maximum packing ratio; $\phi_m \approx 0.63$–0.64 for spheres (Onoda & Liniger, 1990). The first and second normal stresses are related to $\boldsymbol{\Sigma}$ by

$$\left.\begin{aligned} N_1 &= \Sigma_{11} - \Sigma_{22} \\ N_2 &= \Sigma_{22} - \Sigma_{33} \end{aligned}\right\}. \tag{10}$$

Normal stresses differences are difficult to measure experimentally, and results for spherical suspensions show large deviations between investigators (Zarraga et al., 2000; Singh, 2000). Normal stress differences have been described in detail using Stokesian dynamics (Brady & Bossis, 1988; Sierou & Brady, 2001, 2002).

Also of interest is the particle pressure, which is a subtle quantity that has only recently garnered interest because of the role of normal stress in particle migration. Historically, the stress tensors were treated as traceless quantities with an arbitrary isotropic contribution owing to the incompressibility of both fluid and solid phases; however, a two-phase averaging procedure (Drew & Lahey, 1993) shows that, although the suspension-averaged pressure is an arbitrary quantity, a relative difference in pressure can exist between the two phases. The particle pressure is typically defined as

$$\Pi_p = -\frac{1}{3}\Sigma^p_{ii} = -\frac{1}{3V}\sum_{i=1}^{N} S_{ii}, \tag{11}$$

Taking the trace of (4) shows the balance between fluid and particle pressures, $P_f = \Pi_p$ (Prasad & Kytömaa, 1995; Yurkovetsky & Morris, 2008). The particle pressure is analogous to the osmotic pressure induced in colloid suspensions, but the oscillations in the particle trajectories are driven by shear instead of Brownian motion. For rigid spherical suspensions, the particle pressure has been shown analytically for pair-wise interactions of spheres (Jeffrey, Morris & Brady, 1993), calculated through Stokesian dynamics simulations (Sierou & Brady, 2002), and demonstrated experimentally (Zarraga et al., 2000; Deboeuf et al., 2009).

Particle migration has been observed to occur along gradients in shear (Leighton & Acrivos, 1987), thus early phenomenological models proposed a constitutive law of the form $\boldsymbol{j} \sim -\nabla\dot{\gamma}$, where $\boldsymbol{j}$ represents the flux of particles. More advanced shear-gradient-based models were proposed (Phillips, Armstrong, Brown, Graham & Abbott, 1992) that could predict particle migration in certain circumstances; however, these models lacked a firm physical basis. Furthermore, these models failed to predict particle migration in curvilinear flows (Morris & Boulay, 1999).

The suspension balance model (Nott & Brady, 1994), which is based on gradients in the particle-phase normal stresses, has been proposed to explain particle migration. This model is dependent on the accurate determination of the normal stresses in suspensions, which requires the calculation of the particle pressure. Neglecting inertia, the suspension-averaged stress must satisfy the momentum conservation $\nabla \cdot \boldsymbol{\Sigma} = 0$, which upon expanding with (4) gives

$$\nabla \cdot \boldsymbol{\Sigma}^f + \nabla \cdot \boldsymbol{\Sigma}^p = 0. \tag{12}$$

It is these gradients that create a relative motion between the two phases and drive the migration of particles with a flux $\boldsymbol{j} \sim \nabla \cdot \boldsymbol{\Sigma}^p$ (Morris & Boulay, 1999; Morris, 2009). The suspension balance model has been used to explain a variety of particle migration phenomena including resuspension (Leighton & Acrivos, 1986; Morris & Brady, 1998), particle migration in pressure driven flows (Nott & Brady, 1994), and particle migration in curvilinear flows (Morris & Boulay, 1999). A recent review highlighting recent research on the interplay between normal stresses and suspension microstructure can be found in Morris (2009).

1.4 Suspensions of deformable particles

Deformable particles can be drops, viscoelastic solids, or capsules, in which the latter are composed of an elastic membrane surrounding a viscous fluid interior. Deformable particle exhibit much more complex dynamic behavior than rigid particles. In suspensions, these complex dynamics affect the rheology of the bulk flow, creating non-Newtonian flow characteristics, even in the dilute and semidilute regimes.

Dynamic behavior of capsules and vesicles shows rich, nonlinear behavior that has not been fully explored. For example, nonspherical capsules demonstrate at least two dynamical regimes: a tank-treading regime in which the particle assumes a fixed orientation around which the membrane rotates, and a tumbling regime in which the particle tumbles periodically (Keller & Skalak, 1982). In addition to complex dynamics, suspensions of deformable particles require a more sophisticated description of the microstructure. Capsule suspensions present both a single-particle microstructure associated with the particle's deformation and orientation and a configurational microstructure associated with the relative positions of the particles. As a result, the study of suspensions involving deformable particles is somewhat less advanced.

For the deformable particles, the solid phase momentum is governed by Cauchy's equation, which in the limit of negligible inertia can be expressed as

$$\nabla \cdot \boldsymbol{\sigma}_p = 0, \tag{13}$$

where $\boldsymbol{\sigma}_p$ is the stress field present in the solid. For solid particles, the entirety of the particle is governed by (13), with the requirement of continuity of the stress at the fluid–solid interface. For capsules, the finite membrane is governed by (13) while the internal fluid remains incompressible and Newtonian. Again, continuity of the stress field must be preserved on either side of the solid membrane, with the net result being a discontinuity in stress between the internal and external fluids. More detail in the solid modeling can be found in section 2.2.

For the noncolloidal, low-Reynolds-number suspensions in this research, deformability introduces several new nondimensional parameters describing the elasticity. The nondimensional parameter for a solid, elastic particle is the shearoelastic number, defined as

$$\mathrm{N}_{se} \equiv \frac{\mu\dot{\gamma}}{G_S}, \tag{14}$$

where G_S is the solid shear modulus (Pal, 2003). For a fluid-filled capsule surrounded by an elastic membrane, the relevant nondimensional parameter is the capillary number, which is defined as

$$\mathrm{Ca}_G \equiv \frac{\mu\dot{\gamma}a}{G_M}, \tag{15}$$

where G_M is the membrane shear modulus. This capillary number is analogous to that of droplets, except membrane forces are elastic in nature rather than driven by surface tension effects. The membrane shear modulus is related to the shear modulus through $G_M = G_s t_m$, where t_m is the thickness of the membrane. The solid shear modulus is also related to Young's modulus, E_y through the Poisson ratio, ν_p, shown as

$$G_S = \frac{E_y}{1+\nu_p}, \tag{16}$$

which gives rise to a capillary number based on Young's modulus, shown as

$$\mathrm{Ca}_E \equiv \frac{\mu\dot{\gamma}a}{E_M}, \tag{17}$$

where $E_M = E_y t_m$. Membranes can also have an associated resistance to bending, which is made nondimensional by a reduced bending ratio,

$$E_b = \frac{\kappa_b}{a^2 E_y}, \tag{18}$$

where κ_b is the bending modulus of the material.

Capsule dynamics are further complicated by the inclusion of a membrane, with some common membrane models including the simple elastic, Neo-Hookean, Mooney–Rivlin, and Skalak models. Membrane models provide, to various degrees, resistance to surface area changes, in-plane shear, and bending. The presence of an incompressible internal fluid results in conservation of capsule volume and increased energy dissipation. Biological particles are typically referred to as vesicles, a form of capsule, in which a lipid layer (or bilayer) forms a membrane between internal and external fluids. The bilipid layer of a red blood cell strongly resist in-plane dilatation, which enforces area conservation, and the finite thickness of the lipid layers resists bending.

Early analytical work for drops (Cox, 1969) and elastic spheres (Goddard & Miller, 1967; Roscoe, 1967) determined the dilute-limit impact of particle deformation on the suspension rheology; however, these simplified models, although providing qualitative insight, did not fully account for the complex membrane mechanics present in capsules. Keller & Skalak (1982) extended Roscoe's results to describe the tank-treading and tumbling motion of an ellipsoidal particle, which gave some qualitative prediction of dynamics; however, the particle's shape must be described *a priori*, and the particle deformation tensor is uniform, thus neglecting local surface area conservation. In a perturbation about the nearly spherical limit, Barthès-Biesel (1980) analyzed the orientation angle and deformation of capsules with a variety of membrane models (Barthès-Biesel, Diaz & Dhenin, 2002). Small-deformation theories also exist for vesicles, in which surface area is strictly conserved and becomes a specified parameter (Seifert, 1999; Misbah, 2006; Danker & Misbah, 2007). Results capture both tank-treading and tumbling regimes, and dilute-limit rheology results include viscosity and both normal stress differences (Danker & Misbah, 2007; Vlahovska & Gracia, 2007)

A semi-empirical equation derived by Pal (2003) was developed by using the differential effective medium approach (DEMA) using the dilute-limit relationship derived by Goddard & Miller (1967). This extension to high concentrations is given by

$$\mu_r \left[\frac{1 - \frac{3}{2}\mu_r^2 \mathrm{N}_{se}^2}{1 - \frac{3}{2}\mathrm{N}_{se}^2} \right]^{-5/4} = \left[1 - \frac{\phi}{\phi_m} \right]^{-[\mu]\phi_m} . \tag{19}$$

This expression has the same limitations as the Krieger-Dougherty equation: The suspension viscosity is only dependent upon a scalar function involving volume fraction, which implies a Newtonian behavior that precludes the existence of normal stress differences. The relationship by Pal (2003) does, however, predict deformation-induced shear-thinning.

Much of the recent numerical work has explored the role of the viscosity ratio (Biben & Misbah, 2003; Beaucourt, Rioual, Séon, Biben & Misbah, 2004), bending stiffness (Sui, Chew, Roy, Chen & Low, 2007b), and unstressed shape (Kessler, Finken & Seifert, 2008) on the transition between tank-treading behavior and tumbling. Experiments have routinely demonstrated tank-treading (de Haas, Blom, van den Ende, Duits & Mellema, 1997; Kantsler & Steinberg, 2005) and the tank-treading to tumbling transition (Kantsler & Steinberg, 2006; Mader, Vitkova, Abkarian, Viallat & Podgorski, 2006).

Experimentally, solid elastic spheres have been approximated by solid spheres with steric layers grafted onto the surface (Mewis, Frith, Strivens & Russel, 1989) and microgels (Senff & Richtering, 1999). In both cases, defining material properties is problematic, and results were primarily focused on fitting a hard-sphere empirical model to the data using a fitting parameter. Although the steric layer influences the interparticle force to make it "soft", it does little to alter the single-body microstructure, i.e., the particle's shape is still spherical. Furthermore, these researches did not publish data for normal stresses.

1.5 Existing numerical techniques

Numerical techniques have contributed considerably to the fundamental understanding of suspensions. As mentioned in Section 1.3, Stokesian dynamics (Brady & Bossis, 1988) is of particular importance. This method allows the simulation of both colloidal and noncolloidal suspensions of rigid spheres in the Stokes flow limit. Stokesian dynamics (SD) is based on expressing the integral form of the Stokes equations as a multipole expansion about the particle's center and solving the linear system of equations that results. Recently, a more efficient method for simulation within the framework of SD has been developed by Sierou & Brady (2001). Simulations on the scale of 1,000 particles for > 100 strain units have been performed, and they allow accurate calculations of long-time self-diffusivities with calculations that scale as $O(N \log N)$, where N is the number of particles (Sierou & Brady, 2004). The quantities describing microstructure are easily calculated from this method (Morris & Katyal, 2002). Some advantages of SD include its robustness, proven agreement with experimental results, and relative computational efficiency. Its principle and somewhat serious disadvantage is the limitation to simulating rigid spheres. Also, simulations in arbitrary flow domains can be problematic.

The integral form of the Stokes equation can be solved using boundary integral methods that allow the simulation of deformable and nonspherical particles; however, these techniques are even more computationally intensive than SD. Several groups were able to perform simulations of emulsions large enough to obtain normal stress results (Loewenberg & Hinch, 1996; Loewenberg, 1998; Zinchenko & Davis, 2000, 2002); however, in these simulations, drop deformation is governed by a surface tension, and not the elastic tensions found in capsules. Much of the literature capsule methods are focused on the dilute-limit dynamics and rheology. A few methods explore normal stresses; however, no method recovers the particle pressure, even in the dilute case. These simulations typically rely on the boundary integral method (Pozrikidis, 1993, 1995; Ramanujan & Pozrikidis, 1998; Breyiannis & Pozrikidis, 2000), although some groups have used immersed boundary methods (Eggleton & Popel, 1998) or LB methods (Sui et al., 2007b; Sui, Chew & Low, 2007a; Sui, Chew, Roy & Low, 2008).

Dense simulations of elastic capsules are rare, but several research groups are having recent success. Two-dimensional simulations exist with large numbers of capsules (Bagchi, 2007), with investigators reporting the normal stress difference (Breyiannis & Pozrikidis, 2000). Simulations of 3-dimensional capsules are just becoming feasible. For example, Bagchi (2007) has simulated 350 deformable capsules in a square channel using a front-tracking method and Neo-Hookean capsule membrane. More recent results by the group remain focused on flow in microvessels (Doddi & Bagchi, 2009). Other groups are also focused on microcirculation and migration effects in microchannels, and these groups have reported simulations of hundreds of deformable red blood cells (Dupin, Halliday, Care, Alboul & Munn, 2007; Dupin, Halliday, Care & Munn, 2008). In contrast to these results, this thesis represents a systematic study of the bulk rheology of these suspensions. Such a study is required to extend the computational results seen in microvessels to continuum-level models necessary to handle larger flow domains.

1.6 Hybrid approach

The primary focus of this thesis is not on recreating the full range of dynamics exhibited by a capsule in shear, since these have been studied extensively by more accurate membrane models, but to closely analyze the rheology of capsules in both the dilute and concentrated regimes. To date, simulations of a large enough sample of particles to obtain accurate rheology are scarce, and in all cases, the proper description of the particle pressure has not been made. To simulate the large number of particles, several trade-offs must be made: First, the fidelity of the capsule membrane is coarse as compared with isolated studies, and the membrane is a simple linear-elastic FE model. The reduced complexity of the membrane model allows the simulation of a large enough sample of particles to obtain detailed suspension rheology. Owing to the initially spherical shape and linearity of the membrane, the particles display a tank-treading, not tumbling, behavior. The approach outlined in Section 2 develops the hybrid method necessary to simulate these suspensions. The LB and FE methods are outlined in detail, as well as the fluid–solid coupling. Subgrid modeling is discussed. Several corrections to the LB method that are needed to recover the full particle contribution to the suspension stress are presented.

CHAPTER II

METHODOLOGY

2.1 Lattice-Boltzmann method

The lattice-Boltzmann (LB) method was introduced over two decades ago to resolve several shortcomings in lattice-gas models including smoothing statistical fluctuations and imposing Galilean invariance (Frisch, d'Humières, Hasslacher, Lallemand, Pomeau & Rivet, 1987; McNamara & Zanetti, 1988; Higuera & Jimenez, 1989). The LB method can be rigorously shown to converge to the Navier–Stokes solution using a diffusive scaling (Junk & Yong, 2003) or the more traditional Chapman–Enskog expansion (see for example Chen & Doolen, 1998). Since those early investigations, the LB method has developed into a mature computational method for the investigation of a wide variety of fluid dynamics problems including turbulence (Chen, Chen & Matthaeus, 1992; Chen, Kandasamy, Orszag, Shock, Succi & Yakhot, 2003; Keating, Vahala, Yepez, Soe & Vahala, 2007), multiphase flow (Nourgaliev, Dinh, Theofanous & Joseph, 2003), microfluidics (Karniadakis & Beskok, 2005; Kim, Pitsch & Boyd, 2008), and particle suspensions (Ladd, 1994a,b; Aidun & Lu, 1995; Aidun, Lu & Ding, 1998; Ladd & Verberg, 2001). Although developed via an averaging procedure on particles in lattice-gas automata, the LB method has been rigorously reconnected with the original Boltzmann equation. Several books and review articles can be found for further information on the LB method including Chen & Doolen (1998), Succi (2001), and more recently by Aidun & Clausen (2010).

The LB method is well suited for the simulation of particle-fluid suspensions. First, although it is possible to use an unstructured mesh (Nannelli & Succi, 1992), the LB method is most efficiently used on a structured lattice. Thus, the method is most applicable in situations in which the necessary solution resolution is fairly homogeneous, suspensions being one example. Unlike SD and boundary element methods, the hydrodynamic interactions are not assumed to be fully developed. Instead, these interactions are allowed to propagate on time scales below those of particle motion resulting in a spatial locality and an $O(N)$ dependence on the number of particles. Additionally, spatial locality allows for easy and efficient parallel execution of the method, which is important for transitioning to distributed memory cluster computing.

In the LB method, the Boltzmann equation is discretized in velocity space in terms of lattice velocity vectors, $\boldsymbol{e}_i$ where $i = 1 \ldots Q$, which results in the formation of discrete lattice nodes represented by the position vector $\boldsymbol{r}$. A distribution of fluid particles, f_i, exists at each lattice node for each lattice direction, and the time evolution of these distributions are governed by collision and streaming operations. These operations can be expressed as

$$f_i(\boldsymbol{r} + \boldsymbol{e}_i, t+1) = f_i(\boldsymbol{r}, t) - \frac{1}{\tau}\left(f_i(\boldsymbol{r}, t) - f_i^{(eq)}(\boldsymbol{r}, t)\right). \tag{20}$$

The collision operator, $1/\tau$, relaxes the distribution functions towards an equilibrium distribution function, $f_i^{(eq)}$, which is related to the continuum-level fluid viscosity by $\tau = \nu/c_s^2 + 1/2$, where ν is the macroscopic fluid viscosity, and c_s is the LB pseudo sound speed. As in kinetic theory, the fluid distribution functions are related to continuum variables through moments of the distribution functions, shown as

$$\sum_{i=1}^{Q} f_i^{(eq)}(\boldsymbol{r}, t) = \rho \quad \sum_{i=1}^{Q} f_i^{(eq)}(\boldsymbol{r}, t)\boldsymbol{e}_i = \rho\boldsymbol{u} \quad \sum_{i=1}^{Q} f_i^{(eq)}(\boldsymbol{r}, t)\boldsymbol{e}_i\boldsymbol{e}_i = c_s^2\rho\mathbf{I} + \rho\boldsymbol{u}\boldsymbol{u}, \tag{21}$$

where ρ and $\boldsymbol{u}$ are the macroscopic fluid density and velocity, respectfully. The Mach number is related to the velocity through c_s, by $\mathrm{Ma} = u/c_s$. The general form of the equilibrium distribution function, a low-Mach-number expansion of the Maxwellian distribution found, can be expressed as

$$f_i^{(eq)} = w_i\rho\left[1 + \frac{1}{c_s^2}(\boldsymbol{e}_i \cdot \boldsymbol{u}) + \frac{1}{2c_s^4}(\boldsymbol{e}_i \cdot \boldsymbol{u})^2 - \frac{1}{2c_s^2}u^2\right]. \tag{22}$$

where w_i are lattice constants set by the lattice geometry, isotropy, and the constraints in (21). For the 3-dimensional lattice geometry used in this thesis, referred to as D3Q19, the lattice constants (w_i) are 1/3, 1/18, and 1/36 for the rest, non-diagonal, and diagonal directions, respectively, and c_s is $\sqrt{1/3}$.

2.2 Finite element method

The suspended particles are modeled using a linear-elastic FE model. This model is capable of simulating solid elastic particles or fluid-filled capsules surrounded by an elastic membrane. As discussed in the previous chapter, the governing equation is Cauchy's equation (13), and the relevant nondimensional elasticity parameters are the shearoelastic number, N_{se}, for solid particles and the capillary number, Ca_G, for capsules. This method has been published in MacMeccan et al. (2009) with some developments in MacMeccan (2007).

The object is described by an FE mesh which is generated by the commercial software package ANSYS. Solid particles are meshed using tetrahedral elements, while the capsules are meshed using triangular surface elements. The particle's size and relative mesh resolution are described by its radius, a, and the average edge length of the individual mesh elements, l_{FEA}, where both of these quantities are nondimensionalized by the lattice mesh spacing, c. Representatively meshed particles can be seen in Figure 3. Except where noted otherwise, the particle's radius a is dictated by the maximum extent of the FE nodes, i.e., the meshed particle fits entirely within a sphere of radius a. Thus, especially at coarse meshes, the particle's volume is slightly less than that of an ideal sphere.

The transient FE method chosen for this research is derived using an integration on virtual work over a solid element, which is then mapped onto elemental displacements through appropriate shape functions (Bathe, 1996). The integration over virtual work

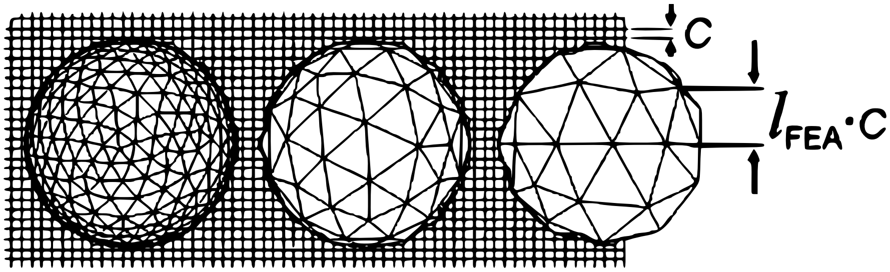

Figure 3: Description of spherical particles with elemental mesh length ratios ranging from $l_{FEA} = 2.0$ (finely meshed) to $l_{FEA} = 6.2$ (coarsely meshed). For all particles, $a = 10$. Figure from MacMeccan et al. (2009).

can be expressed as

$$\int \bar{\boldsymbol{\epsilon}} : \boldsymbol{\sigma} dV = \int \bar{\boldsymbol{X}} \cdot \boldsymbol{F}^{tr} dA + \int \bar{\boldsymbol{X}} \cdot \boldsymbol{F}^{b} dV, \tag{23}$$

where $\bar{\boldsymbol{X}}$ are the elemental virtual displacements, $\bar{\boldsymbol{\epsilon}}$ is an elemental virtual strain due to virtual displacements, $\boldsymbol{F}^{tr}$ are traction stresses on the surface, $\boldsymbol{F}^{b}$ are body stresses such as inertia, A is surface area, and V is volume. The relationship between elemental and nodal quantities is calculated through an interpolation or shape function, H_i, by

$$\boldsymbol{X} = \sum_{i=1}^{N} H_i \boldsymbol{x}_i \quad \boldsymbol{r} = \sum_{i=1}^{N} H_i \boldsymbol{r}_i \tag{24}$$

where $\boldsymbol{r}$ is a global position vector, and $\boldsymbol{x}_i$ and $\boldsymbol{r}_i$ are the nodal displacement and global position vectors of the i^{th} node, respectively. The summation is over all nodes in a given element. A representative linear-elastic solid element is shown in Figure 4(a) with four nodes, and the linear-elastic shell element is shown in Figure 4(b) with three nodes. The coordinates $\boldsymbol{S} = (S_1, S_2, S_2)$ are defined such that for any given direction i, $-1 \leq S_i \leq 1$ with the coordinate origin at the element center, as shown in Figures 4. For a solid tetrahedral element, the shape function is defined as

$$\left.\begin{aligned} H_1 &= \frac{1}{8}\left[(1-S_1)(1-S_2)(1-S_3)\right] \\ H_2 &= \frac{1}{8}\left[(1+S_1)(1-S_2)(1-S_3)\right] \\ H_3 &= \frac{1}{8}\left[(1+S_1)(1+S_2)(1-S_3)\right] \\ H_4 &= \frac{1}{8}\left[(1-S_1)(1+S_2)(1-S_3)\right] \end{aligned}\right\}. \tag{25}$$

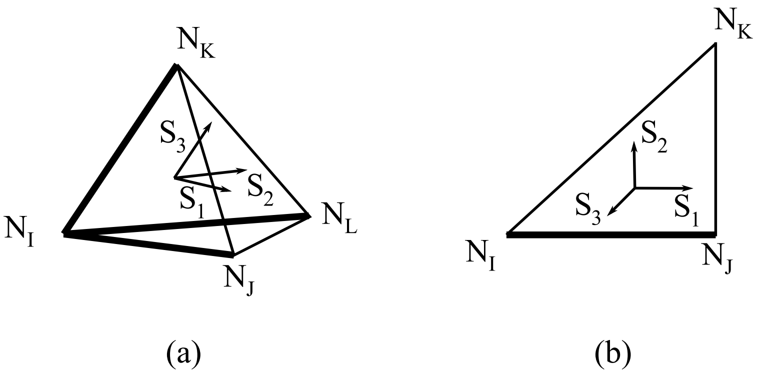

Figure 4: (a) Linear-elastic solid element with four nodes (tetrahedron) and (b) linear-elastic shell element with 3 nodes (triangle). Shell elements have a constant thickness and rotational degrees of freedom along elemental coordinates at each node for bending stiffness. Figure from MacMeccan et al. (2009).

Nodes I, J, K, L in Figure 4(a) correspond to shape function subscripts $1, 2, 3, 4$. The shell elements are shown in Figure 4(b) with three nodes and rotational degrees of freedom for bending stiffness. The shape function for shell elements is formed by truncating the solid shape function and taking $i =$ 1–3 in (25), where shape function subscripts $1, 2, 3$ refer to the nodes I, J, K in Figure 4(b). The coordinates are always orthogonal for shell elements where the out-of-plane normal coordinate, S_3, is chosen to make the coordinate system right-handed, and S_2 is orthogonal in the direction of N_K.

Differentiating the elemental displacements, $\boldsymbol{\epsilon} = d\boldsymbol{X}/d\boldsymbol{r}$ yields elemental strains, which can be related to nodal quantities using (24). Elemental stiffness and mass matrices are constructed from elemental material properties such as density and elasticity, and (23) is evaluated in terms of nodal virtual displacements using the shape function. A detailed derivation of this process can be found in Bathe (1996). Summing over all elements in the FE object gives the transient FE equation,

$$\mathsf{M}\ddot{\boldsymbol{x}} + \mathsf{C}\dot{\boldsymbol{x}} + \mathsf{K}\boldsymbol{x} = \boldsymbol{F}, \tag{26}$$

which determines the time-evolution of the nodal displacement vector, $\boldsymbol{x}$, and its time derivatives, $\dot{\boldsymbol{x}}$ and $\ddot{\boldsymbol{x}}$. The nodal-displacement vector is defined as the deformed node location minus the undeformed node location. The global mass, M, and stiffness, K, matrices are constructed from summing the elemental matrices, and the force vector, $\boldsymbol{F}$, is calculated from traction forces resulting from the fluid–solid coupling as described later.

In the present code, construction of the mass and stiffness matrices in (26) is calculated using the commercial software ANSYS. Owing to the linearity of the model, this information can be imported into our code once at the beginning of the simulation. For the damping matrix, C, Rayleigh damping is used to introduce a minimal amount of material damping, in which C is constructed as a linear combination of both M and K, expressed as

$$\mathsf{C} = \alpha_D \mathsf{M} + \beta_D \mathsf{K}. \tag{27}$$

The Rayleigh damping coefficients, α_D and β_D are related to the solid damping ratios for a given modal circular frequency, ω_n, as $\zeta\left(\omega_n\right) = 1/2\left(\alpha_D \omega_n^{-1} + \beta_D \omega_n\right)$. Rayleigh damping is minimal, such that $\zeta\left(\omega_n\right) \ll 1$ for all simulations. Viscous damping caused by the fluid is much higher than that introduced into the FE method.

Newmark's method, commonly employed in transient FE analysis (Bathe, 1996), is chosen to integrate (26), where Newmark's equations are listed as

$$\ddot{\boldsymbol{x}}_{t+\Delta t} = \beta_n^{-1} \Delta t^{-2} \left[\boldsymbol{x}_{t+\Delta t} - \boldsymbol{x}_t - \Delta t \dot{\boldsymbol{x}}_t - \Delta t^2 \left(0.5 - \beta_n\right) \ddot{\boldsymbol{x}}_t\right] \tag{28}$$

and

$$\dot{\boldsymbol{x}}_{t+\Delta t} = \dot{\boldsymbol{x}}_t + \Delta t \left[\left(1 - \gamma_n\right) + \gamma_n \ddot{\boldsymbol{x}}_{t+\Delta t}\right]. \tag{29}$$

These relationships can be substituted into (26) and, with some manipulation (Bathe, 1996), produce a solid phase time-evolution equation of the form

$$\mathsf{K'}_{t+\Delta t} \boldsymbol{x}_{t+\Delta t} = \boldsymbol{F}'_{t+\Delta t}, \tag{30}$$

where

$$\mathsf{K'} = \mathsf{K} + \frac{1}{\beta_n \Delta t^2} \mathsf{M} + \frac{\gamma_n}{\beta_n \Delta t} \mathsf{C},$$

$$\boldsymbol{F}'_{t+\Delta t} = \boldsymbol{F}_{t+\Delta t} + \frac{\mathbf{M}}{\beta_n \Delta t^2}\left[\boldsymbol{x}_t + \Delta t \dot{\boldsymbol{x}}_t + \Delta t^2 \left(0.5 - \beta_n\right) \ddot{\boldsymbol{x}}_t\right] + \mathbf{C}\left[\frac{\gamma_n}{\beta_n \Delta t}\boldsymbol{x}_t + \left(\frac{\gamma_n}{\beta_n} - 1\right)\dot{\boldsymbol{x}}_t + \Delta t\left(0.5\frac{\gamma_n}{\beta_n} - 1\right)\ddot{\boldsymbol{x}}_t\right], \quad (31)$$

and the t subscripts denote time. The choice of $\beta_n = 1/6$ and $\gamma_n = 1/2$ yields a constant acceleration method that is unconditionally stable assuming the forces are known at $t + \Delta t$. Unfortunately, the coupling between LB and FE schemes precludes the knowledge of $\boldsymbol{F}_{t+\Delta t}$ thus making the method conditionally stable; however, the short time steps inherent to the LB method cause the integration to be stable with a pure LB coupling. Stability issues have arisen during subgrid modeling, and these will be discussed in Section 2.3.2. Furthermore, an FE time step equal to the LB time step, $\Delta t = 1$, adequately resolves all FE modes. For particle capillary numbers $O(0.01)$, the highest natural frequency modes are approximately 40 LB time steps. The key to the efficient simulation particle dynamics using (30) is the use of a body-fixed coordinate system such that the FE matrices ($\mathbf{M}$, $\mathbf{C}$, $\mathbf{K}$) are invariant during a simulation. Thus, the inversion of $\mathbf{K}'$ can be performed once upon initialization, and the subsequent time evolution of the particle computationally efficient, consisting of several matrix-vector products. The body-fixed coordinates are tracked using Eulerian angles and updated based on the particle's center of mass and the average rotation of all FE nodes.

2.3 Fluid–solid coupling

2.3.1 Bounce-back method

Coupling between the fluid and solid phases is performed using the bounce-back method detailed by Aidun et al. (1998). In the bounce-back operation, the momentum of the fluid distribution adjacent to a moving boundary is adjusted along boundary links that cross the solid boundary connecting lattice sites. The bounce-back operation, one of the oldest methods of imposing the no-slip boundary condition in the LB method, has its roots in lattice gas methods and is well studied (Cornubert, d'Humières & Levermore, 1991; Ladd, 1994a,b; Aidun & Lu, 1995; Aidun et al., 1998). For a solid boundary exactly at the midpoint of the link, the bounce-back method is second-order accurate in space (Ziegler, 1993); however, arbitrary boundary placements degrade the accuracy to first-order (Ginzbourg & Adler, 1994; Noble, Chen, Georgiadis & Buckius, 1995). More accurate versions of the bounce-back operation are available including linear and quadratic interpolation methods (Bouzidi, Firdaouss & Lallemand, 2001; Mei, Yu, Shyy & Luo, 2002; Lallemand & Luo, 2003) and the third-order spatially accurate multireflection method by d'Humières, Ginzburg, Krafczyk, Lallemand & Luo (2002). These methods depend on multiple layers of LB nodes adjacent to the solid surface, which may not be present in dense suspension simulations. Furthermore, Junk & Yang (2005) have shown that using the standard bounce back when these extra nodes do not exist introduces errors that propagate throughout the domain destroying the additional accuracy. Recent developments attempt to circumvent these limitations; however, issues remain, particularly the lack of stringent mass conservation (Chun & Ladd, 2007), which make these methods unsuitable for this study.

The development of non-link-based methods (Feng & Michaelides, 2004; Wu & Aidun, 2009) provides an exciting opportunity to incorporate higher-order boundary conditions in the future. These methods avoid the costly determination of links crossing an arbitrary 3-dimensional surface, instead relying on interpolation functions from the immersed boundary method (Peskin, 2002). These methods exhibit much less temporal fluctuation in the force applied to the particles (Wu & Aidun, 2009), and simulations require fewer LB nodes to resolve a solid surface (Wu & Aidun, 2010).

A model boundary link crossing a FE surface can be seen in Figure 5. These links are determined via a projection of rays along the LB direction vectors, $\boldsymbol{e}_i$. Intersections with the triangular FE surfaces are calculated using a minimal storage triangle–ray intersection routine developed for ray-tracing, a 3-dimensional computer modeling application (Möller & Trumbore, 1997). This method relies on projecting the ray in barycentric coordinates relative to the surface triangle, and it returns a distance along the ray where intersection occurs. Aggressive caching and filtering is used to eliminate redundant computations; however, this routine still accounts for a sizable portion of computation (roughly 40%). The bounce-back procedure adjusts distributions on the link endpoints according to

$$f_i(\boldsymbol{r}, t+1) = f_{i'}(\boldsymbol{r}, t^+) + 6\rho w_i \boldsymbol{u}_b \cdot \boldsymbol{e}_i \tag{32}$$

for a link in the i' direction, where i' is the direction opposite of i, t^+ denotes the time post collision but prior to streaming in (20), and $\boldsymbol{u}_b$ is the local solid velocity at the link intersection point Assuming a time step of one and uniform distribution of force over a single time step, the adjustment in (32) corresponds to a traction force on the object of

$$\boldsymbol{F}^{(b)}(\boldsymbol{r} + \tfrac{1}{2}\boldsymbol{e}_{i'}, t) = -2\boldsymbol{e}_i \left[f_{i'}(\boldsymbol{r}, t^+) + 3\rho w_i \boldsymbol{u}_b \cdot \boldsymbol{e}_i \right]. \tag{33}$$

Total force and torque on the particles are given by summations over all boundary links according to

$$\left.\begin{aligned} \boldsymbol{F}^{total} &= \sum_{BL} \boldsymbol{F}_{i'}^{(b)}(\boldsymbol{r} + \tfrac{1}{2}\boldsymbol{e}_{i'}, t) \\ \boldsymbol{T}^{total} &= \sum_{BL} \left(\boldsymbol{r} + \tfrac{1}{2}\boldsymbol{e}_{i'} - \boldsymbol{r}_0\right) \times \boldsymbol{F}_{i'}^{(b)}(\boldsymbol{r} + \tfrac{1}{2}\boldsymbol{e}_{i'}, t) \end{aligned}\right\}, \tag{34}$$

where $\boldsymbol{r}_0$ is the particle's center of mass. For a rigid particle, dynamics are calculated using Newtonian mechanics, with typical schemes including explicit integration (Aidun et al., 1998; Ding & Aidun, 2003) or implicit integration (Nguyen & Ladd, 2002).

For the FE objects in this study, the boundary force from (33) must be interpolated to the nearest FE nodes, also shown in Figure 5. In this study, a simple linear interpolation is found to be adequate provided that $l_{FEA} > c$. Also, a distinction

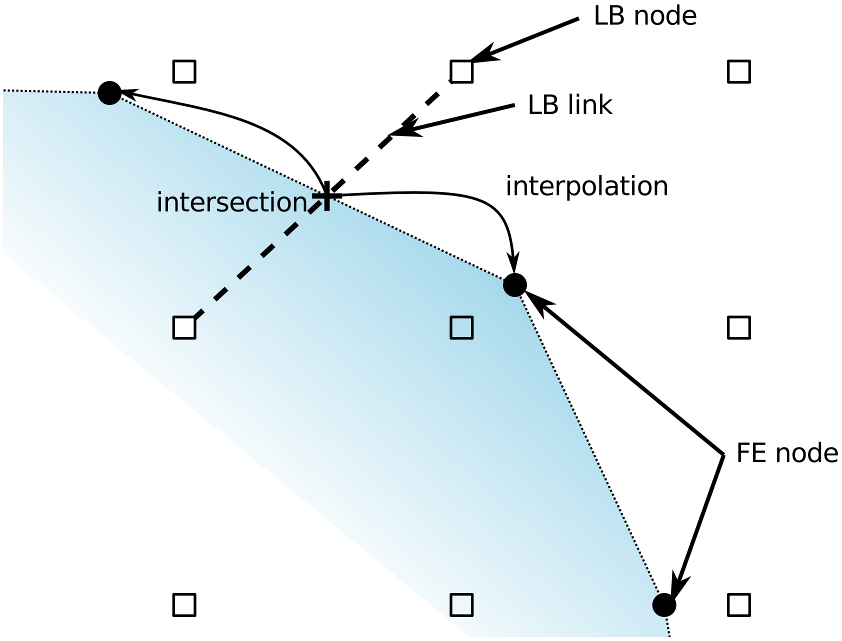

Figure 5: Depiction of a link crossing the solid boundary and subsequent interpolation to neighboring FE solid nodes.

must be made between solid (rigid or elastic) and fluid-filled (shell or membrane) particles. For solid particles, the interior fluid nodes have no impact on the dynamics of the particle. As the particle covers and uncovers LB fluid nodes, an adjustment to the momentum of the particle must be made, which for the case of covering a node can be expressed as

$$\boldsymbol{F}^{(c)}(\boldsymbol{r}, t+\tfrac{1}{2}) = \rho(\boldsymbol{r}, t)\left[\boldsymbol{u}(\boldsymbol{r}, t) - \boldsymbol{u}_b(\boldsymbol{r}, t)\right]. \tag{35}$$

Uncovering takes the opposite sign of (35). For shell particles this adjustment is not needed. The results in this thesis focus exclusively on fluid-filled capsules.

2.3.2 Subgrid modeling

As particles approach to within one lattice unit of one another, no intervening fluid nodes exist, and the LB method fails to capture lubrication hydrodynamics. As such, subgrid modeling may be necessary to capture the large forces as particles come into near contact. The method employed here is based the model originally developed by Ding & Aidun (2003); however, the implementation details left some ambiguity leading to several errors in the implementation used in MacMeccan et al. (2009). As a result, the link-wise method in MacMeccan et al. (2009) overpredicts the tangential or shear component of the lubrication force, while underpredicting the normal or squeezing flow component. Ladd & Verberg (2001) and Nguyen & Ladd (2002) also developed lubrication models for use in LB simulations, but these methods are restricted to spherical particles.

According to lubrication theory (Cox, 1974; Jeffrey & Onishi, 1984; Kim & Karilla, 1991), the normal (squeezing) component of force between two spheres scales to leading order as $1/\varepsilon$, where ε is the gap between particles, while the tangential (shear) components scale as $\ln(1/\varepsilon)$. Consequently, the much larger squeezing flow component of the lubrication interactions is modeled while the tangential and rotational interactions are neglected. Such a strategy still results in fairly accurate results owing to the weak singular nature of $\ln(1/\varepsilon)$ as compared with the strong singular nature of $1/\varepsilon$ present in the squeezing flow situation. The modeling introduced here will reproduce the leading order singularity, and the LB method will resolve the far-field interactions.

The analytical force between two spheres is given in Cox (1974) as

$$F_{lub} = \frac{3\pi\mu U_{app}}{2\lambda^2\varepsilon} + O\left(ln(\varepsilon^{-1})\right), \tag{36}$$

where U_{app} is the approach velocity between the spheres, and λ is a curvature parameter defined as

$$\lambda = \frac{1}{2}\left(\frac{1}{a} + \frac{1}{b}\right),$$

and a and b are the particle radii. This solution is a result of an asymptotic expansion of the hydrodynamic equations at small gaps. Ding & Aidun (2003) proceed by defining an surface stress element of

$$df = \frac{3\mu U_{app}}{2\lambda g^2}, \tag{37}$$

where g is the gap between two particles at the given surface element. Upon integration over the particle surface, this differential element of force recovers (36). Next, the integration is approximated via a summation over the links, with a weighting coefficient $\bar{q}$ that is determined via simulation. This leads to a link-wise force $dF_{lub} = \bar{q}df$.

Since U_{app} is calculated as the centerline approach velocity when using spherical particles, links crossing the particle's surface diagonally provide no net torque on the particle. When translating the method to arbitrarily shaped FE particles, the approach velocity was based on the local surface velocity projected along the link (MacMeccan et al., 2009), which for particle surfaces shearing past one another, resulted in scaling the shear component of the lubrication force according to the strong singular nature of $1/\varepsilon$. Accordingly, a new link-wise lubrication model that projects the approach velocity, gap, and applied force along the surface normal, thus reducing erroneously applied shear, is shown as

$$d\boldsymbol{F}^{lub} = -\left(\frac{3\bar{q}\mu U_{app}}{2\lambda g^2}\right)\boldsymbol{n}_{avg}. \tag{38}$$

In the following relationships, the parenthetical subscripts a and b distinguish between the two spheres near contact. The average surface normal is defined as

$$\boldsymbol{n}_{avg} = \frac{\boldsymbol{n}_{(a)} - \boldsymbol{n}_{(b)}}{\|\boldsymbol{n}_{(a)} - \boldsymbol{n}_{(b)}\|},$$

the approach velocity as

$$U_{app} = -\left(\boldsymbol{u}_{\boldsymbol{b}(b)} - \boldsymbol{u}_{\boldsymbol{b}(a)}\right) \cdot \boldsymbol{n}_{avg},$$

and the local gap as

$$g = (g'\boldsymbol{e}_i) \cdot \boldsymbol{n}_{avg},$$

where g' is the gap between surfaces along the link. The curvature calculation is unchanged from MacMeccan et al. (2009), and is calculated by

$$\lambda = \frac{1}{N}\sum_{i=1}^{N}\left|\frac{\mathrm{d}\boldsymbol{T}_{surf}}{\mathrm{d}\boldsymbol{s}}\right|,$$

where $\boldsymbol{T}_{surf}$ is the tangent vector to the surface in the direction of $\boldsymbol{s}$, and $\boldsymbol{s}$ is a vector connecting finite-element surface centroids. The summation is performed over all neighboring surfaces, with $N = 3$ for triangles. For the model proposed in (38), a fitting parameter of $\bar{q} = 0.4$ is determined experimentally, which differs from the value of 0.6 in Ding & Aidun (2003). Thus, the total force exerted on the FE particle is equal to the combined effect of the bounce-back operation, node covering, and subgrid modeling, which is expressed as

$$\boldsymbol{F}^{link} = \boldsymbol{F}^{(b)} + \boldsymbol{F}^{(c)} + d\boldsymbol{F}^{lub}. \tag{39}$$

Some important differences between (40) and the models in Ding & Aidun (2003) and MacMeccan et al. (2009) include the lack of a scaling parameter for diagonal links and the lack of a smoothing function that subtracted the lubrication force at $g = c_i$ from the solution in (38). The scaling parameter is no longer needed since the gap and velocities are projected along $\boldsymbol{n}_{avg}$, which inherently scales diagonal links. The smoothing function is not necessary since the force recovered via the LB bounce-back goes from an accurate value for gaps with an intervening fluid node to zero for gaps without an intervening fluid node. Thus, the smoothing term degrades accuracy and serves no purpose since the bounce-back method is inherently not smooth. The summation over all links still results in a relatively smooth growth of lubrication forces. Also, the finite discretization of the particles, combined with the discrete nature of the links, causes an uncertainty in the particle border as compared with an ideal spherical particle, as illustrated in Figure 6. Thus, lubrication is expected to break down owing to the "roughness" of the suspended particles at a certain point, with the resulting interaction between particles growing in uncertainty based on the local surface mesh and the particle's position on the underlying LB grid. It is also worth mentioning that the new lubrication model is more easily adaptable to non-link-based methods, such as the external boundary force of Wu & Aidun (2009). The model in (38) is only dependent on local surface geometry and velocity, which is

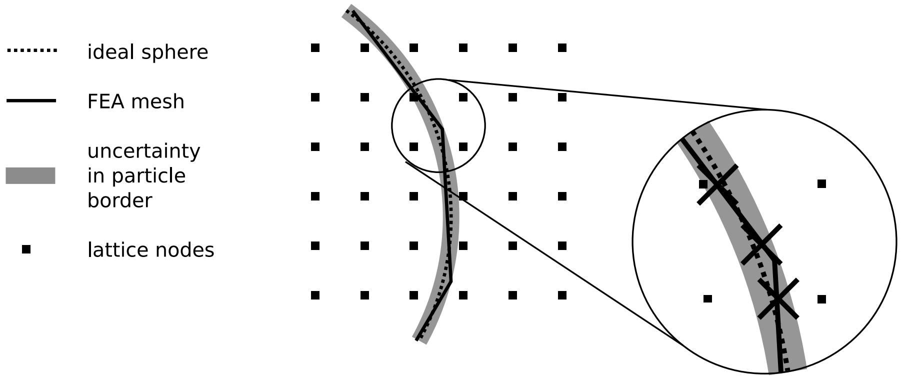

Figure 6: Uncertainty in the particle border created by the combined discretization of the solid and fluid. Discretization of the FEA mesh creates uncertainty in the particle border compared with an ideal sphere. This uncertainty is magnified by the overlay of the fluid lattice nodes and subsequent link finding shown in inset. Link intersections are marked with crosses (×). Figure from MacMeccan et al. (2009).

further abstracted from the link concept than the model of MacMeccan et al. (2009). The sole purpose of the links is to provide a convenient numerical discretization; therefore, other means of discretization to define a differential stress element are possible, which includes methods based only on the solid geometry.

Obviously, the lubrication interactions are strongly singular, which causes instabilities during the particle update procedure. This issue is seen in simulations of rigid particle suspensions for a variety of numerical schemes (Brady & Bossis, 1988; Ladd & Verberg, 2001). Without interparticle forces or Brownian motion to impose separation between particles, clustering and particle agglomeration will ensue until gaps can no longer be resolved by the numerical scheme. Accordingly, small repulsive forces are typically applied to maintain stability in the particle update procedure (Brady & Bossis, 1988; Sierou & Brady, 2002; Ladd & Verberg, 2001; MacMeccan et al., 2009). Alternatively, researchers have used a cluster-implicit update procedure to implicitly update the dynamics of all particles near contact (Nguyen & Ladd, 2002); however, these techniques are computationally prohibitive for FE particles. Instabilities in the update procedure are exacerbated by the deformability of the particle surface.

Whereas the response of a solid particle to lubrication forcing requires the entire particle to move, thus damping instability with inertia, the response of a deformable particle is only local to the point of force application. There exists some stability benefit to deformation, however, since although the surface of highly deformable particles more readily fluctuates, large deformation tends to create larger gaps between particles offsetting the decrease in stability.

To prevent instability, a short-ranged contact force is applied. The function chosen in MacMeccan et al. (2009) is adequate; however, the value of the constants could benefit from a more systematic examination. This function has the form

$$A_c \exp\left(\frac{g_c - g}{\sigma_c}\right) \quad \text{if } g \leq g_c,$$

where A_c is a contact scaling constant, and σ_c is a constant determining the range of the contact force. This quantity needs to be nondimensionalized, and an attempt was made to scale A_c by the viscous force scale, $6\pi\mu a U_s$, where U_s is a suitable velocity scale; however, this is the incorrect scaling for this function. The link-wise forces are equivalent to stresses, thus the appropriate scaling is $6\pi\mu U_s/a$. The contact function in MacMeccan et al. (2009) is not applied over the cutoff gap, which leads to discontinuities depending on the selection of contact coefficients. Since the contact force has no velocity dependence, unlike the lubrication force, the contact force can be projected along the link unit vector direction, $\boldsymbol{e}_i/||\boldsymbol{e}_i||$, as was done in MacMeccan et al. (2009). Choosing a function that decays to zero as the $g \to g_c$ and applying the contact at all gaps would eliminate this discontinuity. Nondimensionalizing all quantities and applying the contact everywhere gives a contact and lubrication equation,

$$d\tilde{\boldsymbol{F}}^{lub} = \begin{cases} 0 & \text{if } \tilde{g} > c_i/a, \\ -\dfrac{\bar{q}}{4\pi}\dfrac{\tilde{U}_{app}}{\tilde{\lambda}\tilde{g}^2}\boldsymbol{n}_{avg} - \tilde{A}_c \exp\left(\dfrac{\tilde{g}_c - \tilde{g}}{\tilde{\sigma}_c}\right)\dfrac{\boldsymbol{e}_i}{||\boldsymbol{e}_i||} & \text{if } \tilde{g}_c < \tilde{g} \leq c_i/a, \\ -\dfrac{\bar{q}}{4\pi}\dfrac{\tilde{U}_{app}}{\tilde{\lambda}\tilde{g}_c^2}\boldsymbol{n}_{avg} - \tilde{A}_c \exp\left(\dfrac{\tilde{g}_c - \tilde{g}}{\tilde{\sigma}_c}\right)\dfrac{\boldsymbol{e}_i}{||\boldsymbol{e}_i||} & \text{if } \tilde{g} \leq \tilde{g}_c, \end{cases} \tag{40}$$

where scaled variables are denoted by a tilde. Nominal values used in MacMeccan et al. (2009) were $\tilde{A}_c \sim 100$ and $\tilde{\sigma}_c = \tilde{g}_c = 0.03$. The result from these choices is a contact function that is too long-ranged, which causes a discontinuity at the cutoff gap, and too weak, which led to particles overlapping. The ideal selection for the constants should allow a repulsive force capable of keeping particle separated yet a lower gradient than the equivalent lubrication model to keep the particle update stable. Secondly, $\tilde{\sigma}_c$ should cause the contact force to approach zero at $\tilde{g}_c$. The cutoff gap is constrained by the stability of the particle update procedure. A per-link comparison of the various lubrication and contact models is shown in Figure 7, and the nondimensional force along the link, $d\tilde{F}^{lub}$ is plotted against the nondimensional gap, $\tilde{g}$. Contact constants chosen for the adjusted model are $\tilde{A}_c = 5$, $\tilde{g}_c = 0.03$, and $\tilde{\sigma}_c = 0.005$.

In Figure 7, the velocity scale was used as the approach velocity for the lubrication model, which creates the fortuitous matching at $\tilde{g} < 0.03$. In reality, (40) will overpredict the lubrication repulsive force for $U_{app} < U_s$, drastically so when the approach velocity is negative. The accuracy of the lubrication model will be investigated further in section 2.7.5 for rigid particles in model problems; however, stability when simulating deformable particles is still an issue. The impact of interparticle forces has been studied for rigid spherical particles (Sierou & Brady, 2001) and will be discussed briefly in context of suspension simulations in chapter 5; however, the effect of contact mechanics on rheology will be left as an open question for further research. This study will concentrate on the effect of deformation of the suspended

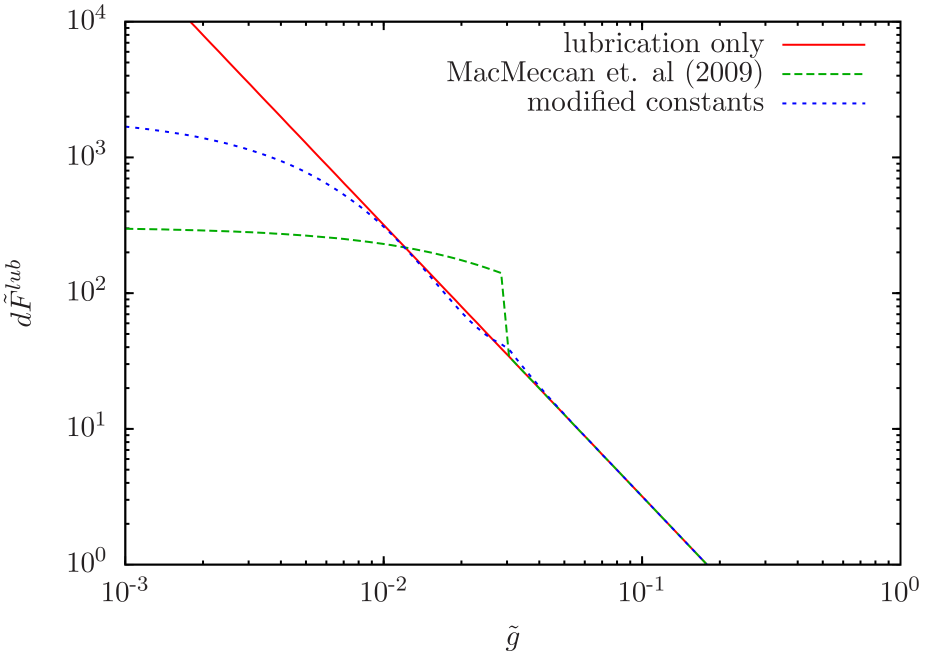

Figure 7: Lubrication and contact model for a single link. Constants for MacMeccan et al. (2009) are $\tilde{A}_c = 100$ and $\tilde{\sigma}_c = 0.03$ and for the adjusted model are $\tilde{A}_c = 5$ and $\tilde{\sigma}_c = 0.005$. In both cases $\tilde{g}_c = 0.03$.

phase.

2.4 Lees–Edwards boundary condition

Removing wall effects to determine bulk properties is desirable when probing suspension rheology, and simply increasing the domain size of a wall-bounded shear simulation to the extent that wall effects are negligible is computationally expensive. The Lees–Edwards boundary condition (LEbc), developed by Lees & Edwards (1972) for molecular dynamics, allows the simulation of bulk flows in simple shear. This method has been extended to the LB method by (Wagner & Yeomans, 1999; Wagner & Pagonabarraga, 2002). In the LEbc, the flow and vorticity directions are treated in the typical periodic manner; however, in the shear direction, periodic domains are shifted continuously in time with a velocity equal to $\pm\dot{\gamma}H$, where $\dot{\gamma}$ is the imposed shear rate and H is the domain length in the shear direction. The simulation domain is shown as a solid box in Figure 8a, with periodic images appearing as dotted

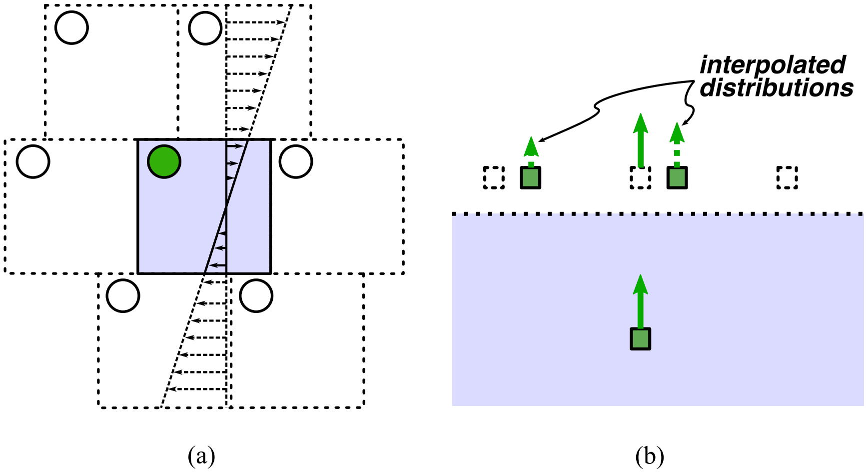

Figure 8: Lees–Edwards boundary condition for the LB method, where (a) shows periodic domain images advecting with velocity $\pm\dot{\gamma}H$, and (b) shows the required interpolation for distributions propagating from the top to bottom of the simulation domain. Figure from Aidun & Clausen (2010).

outlines. Also shown is a representative particle and its periodic images. Material crossing the top shear border, both fluid and suspended solids, must undergo a shift in position in the flow direction equal to $-\dot{\gamma}Ht$ and a shift in velocity in the flow direction of $-\dot{\gamma}H$ before reappearing in the bottom of the simulation domain.

Implementing the velocity shift in the framework of the LB method requires altering fluid distributions crossing the shear border, as shown in Figure 8b. Wagner & Pagonabarraga (2002) propose a Galilean shift to the fluid distributions expressed as

$$f_i^{GS} = f_i + f_i^{eq}(\rho, \boldsymbol{u} \pm \dot{\gamma}H) - f_i^{eq}(\rho, \boldsymbol{u}), \tag{41}$$

where f_i^{GS} is the adjusted distribution. Since the positional shift is continuously varying in time, the lattice symmetry is broken, and fluid distributions propagating across the boundary are linearly interpolated to the nearest lattice nodes. The LEbc has been successfully applied to rigid and deformable suspensions in the calculation of shear viscosity with good results (Lishchuk, Halliday & Care, 2006; MacMeccan et al., 2009).

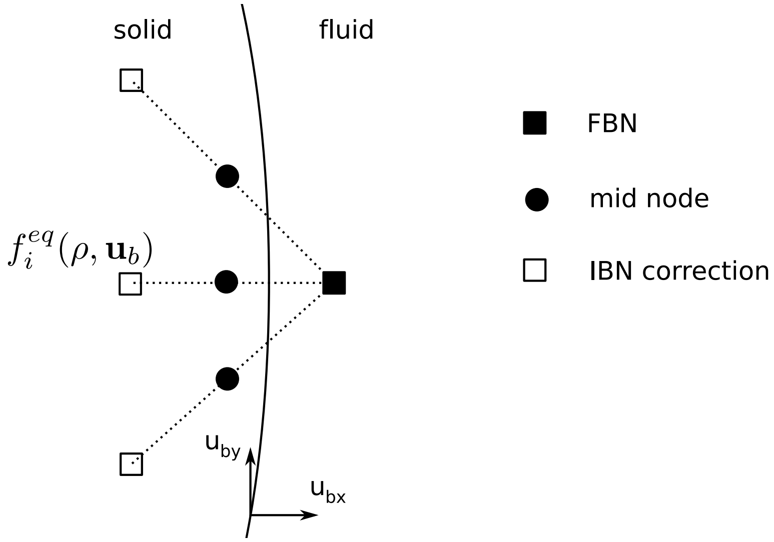

Figure 9: Fully relaxed fluid node adjacent to a moving boundary, referred to as a fluid boundary node (FBN). Boundary links shown crossing solid boundary. Figure from Clausen & Aidun (2009).

2.5 Galilean error

It is well known that the LB method approximates the incompressible Navier–Stokes equations with compressibility errors that grow as Ma^2, and the LB method is Galilean invariant with errors of $O(u^3)$. This has led to the typical statement that simulations with $\mathrm{Ma} \leq 0.1$ result in negligible error, which is appropriate in many cases; however, the recent interest in more sensitive parameters such as normal stress differences, suspension pressures, and particle diffusivity indicates that these errors may be important. The effect of these errors on the calculation of the particle stresslet is especially important.

Following Clausen & Aidun (2009), Galilean errors are calculated by considering a moving boundary adjacent to a fluid node as depicted in Figure 9. A fluid node adjacent to a solid surface is called a fluid boundary node (FBN), and the point of force application, which is the midpoint on the boundary link, is called the mid node. In a fully relaxed system in which the mesh size tends to zero, the FBNs relax to an equilibrium distribution approaching the boundary velocity, $\boldsymbol{u}_b$. Calculating the equilibrium distribution using the boundary velocity with (22) and substituting into (33) results in an error term given by

$$\boldsymbol{F}^{(err)} = -2\rho w_i \boldsymbol{e}_i \left[1 + \tfrac{9}{2}(\boldsymbol{e}_i \cdot \boldsymbol{u}_b)^2 - \tfrac{3}{2}u_b^2\right]. \tag{42}$$

Clearly, the quadratic terms in the equilibrium distribution break Galilean invariance. It is important to note that when simulating fluid-filled shells, there exists a corresponding internal fluid node which exactly cancels the error present in (42); therefore, no error in particle force and torque exists. When simulating a solid particle, however, the internal fluid has no impact on particle dynamics, thus global errors in force and torque calculations may exist. Both methods have errors in external traction force calculations typically used in the calculation of the particle contribution to suspension stress.

For a spherical particle in simple shear moving with the local fluid velocity, U_x, and rotating with the local rotation, $\dot{\gamma}/2$, an analytical description of the error in force and stresslet calculations can be derived. First, an estimate of the error due to all boundary links associated with one FBN is made by adding the associated Galilean errors. In the limit of an infinitely small lattice spacing, the boundary velocity for all links emanating from the same FBN will be equal. For the vertical wall shown in Figure 9 with a D2Q9 LBM scheme, the errors from (42) are summed to result in

$$\boldsymbol{F}_{FBN}^{(err)} = -\rho \begin{bmatrix} 1/3 + u_{bx}^2 \\ u_{bx}u_{by} \end{bmatrix}, \tag{43}$$

where u_{bx} and u_{by} are the x and y components of the boundary velocity. Also note that the length of the surface described by one FBN is a single lattice unit making the expression in (43) equivalent to a stress. A similar analysis can be performed for a horizontal wall, and the results can be generalized to handle either side of the wall via the boundary normal vector, $\boldsymbol{n}$. The resulting error terms, designated with V

and H for vertical and horizontal, are

$$\boldsymbol{F}^{(err)}_{FBN-V} = -\rho \frac{n_x}{|n_x|} \begin{bmatrix} 1/3 + u_{bx}^2 \\ \\ u_{bx} u_{by} \end{bmatrix}, \quad \boldsymbol{F}^{(err)}_{FBN-H} = -\rho \frac{n_y}{|n_y|} \begin{bmatrix} u_{bx} u_{by} \\ \\ 1/3 + u_{by}^2 \end{bmatrix}. \tag{44}$$

The goal is to extend the discrete results from (44) to arbitrarily oriented surfaces. In the LB method, a smooth object is represented by mid nodes that reside on the midpoint of links crossing the solid surface, as illustrated in Figure 10. This discretization results in a stair-stepping effect such that an inclined surface is represented by a combination of vertical and horizontal surfaces. Thus, for an arbitrarily oriented surface, the error can be approximated as a combination of errors from both horizontal and vertical surfaces, with appropriate weighting for the projected area. Such an assumption also agrees with the isotropic structure of the lattice. Thus, the boundary force on an arbitrarily aligned surface element can be expressed as

$$\delta \boldsymbol{F}^{(err)} = |n_x| \boldsymbol{F}^{(err)}_{FBN-V} + |n_y| \boldsymbol{F}^{(err)}_{FBN-H}, \tag{45}$$

which can be simplified to

$$\delta \boldsymbol{F}^{(err)} = -\rho \begin{bmatrix} n_x \left(1/3 + u_{bx}^2\right) + n_y u_{bx} u_{by} \\ \\ n_y \left(1/3 + u_{by}^2\right) + n_x u_{bx} u_{by} \end{bmatrix}. \tag{46}$$

A similar analysis can be performed for the D3Q19 lattice model, and the error in boundary force can be described as

$$\delta \boldsymbol{F}^{(err)} = -\rho \begin{bmatrix} n_x \left(1/3 + u_{bx}^2\right) + n_y u_{bx} u_{by} + n_z u_{bx} u_{bz} \\ \\ n_y \left(1/3 + u_{by}^2\right) + n_x u_{bx} u_{by} + n_z u_{by} u_{bz} \\ \\ n_z \left(1/3 + u_{bz}^2\right) + n_x u_{bx} u_{bz} + n_y u_{by} u_{bz} \end{bmatrix}. \tag{47}$$

In both the 2-dimensional and 3-dimensional cases, the normal forces created by the Galilean error can be expressed as

$$\delta \boldsymbol{F}^{(err)} \cdot \boldsymbol{n} = -\rho \left[1/3 + (\boldsymbol{u}_b \cdot \boldsymbol{n})^2\right]. \tag{48}$$

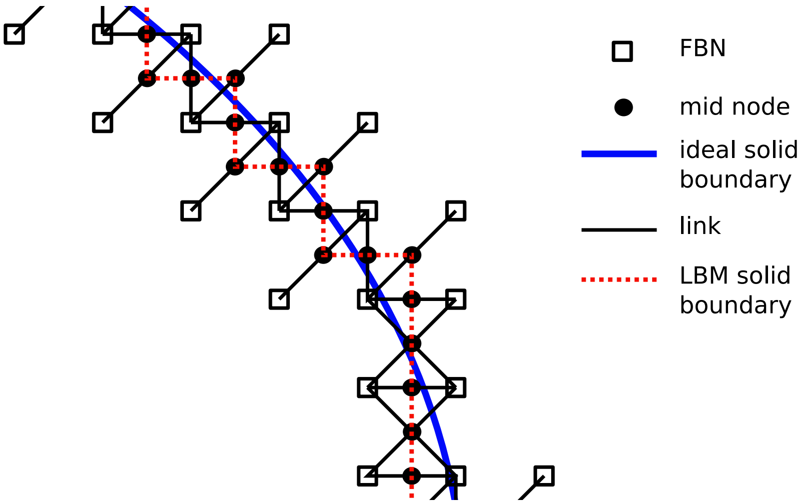

Figure 10: Discretization of smooth particle by links crossing particle boundary creating a combination of horizontal and vertical surfaces. Actual particle boundary shown by heavy blue line, and particle boundary as seen by the LBM shown by dotted red line. Figure from Clausen & Aidun (2009).

The first term is simply the hydrostatic pressure found in the LBM, where $P_f = c_s^2\rho$, and can typically be neglected. The second term breaks Galilean invariance and creates errors in normal stresses that scale as u_b^2.

By inspection, (48) creates an artificial normal stress on the fore and aft surface of a translating particle. Quantifying the impact of the normal error on the calculation of total force and particle stresslet is found by integrating over the differential error. The force and stresslet errors are calculated by integrating on the particle surface, shown as

$$\boldsymbol{F}^{(err)} = \int \delta\boldsymbol{F}^{(err)} dA \tag{49}$$

for the error in total force on the particle, and

$$\mathbf{S}^{(err)} = \int \tfrac{1}{2}\left(\delta\boldsymbol{F}^{(err)}\boldsymbol{r} + \boldsymbol{r}\delta\boldsymbol{F}^{(err)}\right) dA \tag{50}$$

for the error in particle stresslet.

Consider a spherical particle in simple shear in which the particle is traveling with the local fluid velocity, U_x, and rotating with the local rotation of the fluid, $\dot{\gamma}/2$, where $\dot{\gamma}$ is the shear rate. Such situations frequently arise during simulations,

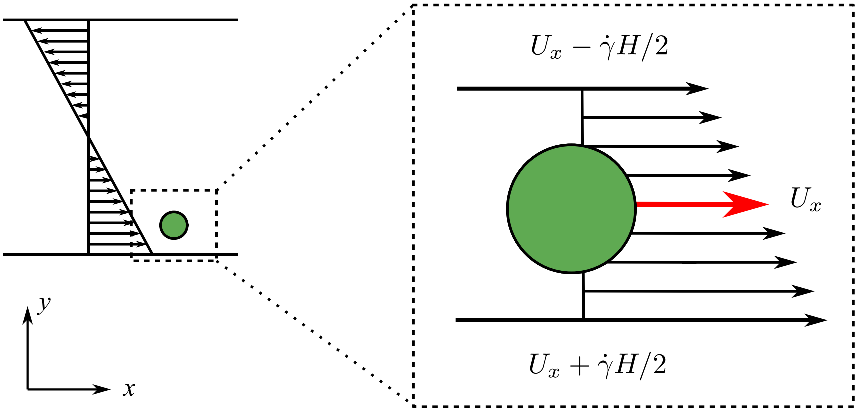

Figure 11: Particle in simple shear near the domain border in a large-scale simulation is analogous to a particle with superposed shear and translational velocity. Figure from Clausen & Aidun (2009).

such as a particle in simple shear offset from the centerline, as shown in Figure 11. Calculating the integrals in (49) and (50) with the appropriate boundary velocity and neglecting the isotropic static pressure results in error terms of

$$F_y^{(err)} = -\rho V_p \dot{\gamma} U_x / 2 \tag{51}$$

and

$$S_{11}^{(err)} = -\rho V_p U_x^2, \tag{52}$$

where V_p is the volume of the particle. All other force and stresslet errors are zero. For suspensions of rigid spheres, normal stresses are small at low concentrations ($\leq 20\%$), with magnitudes of $O(10^{-2})$ when normalized by $\mu\dot{\gamma}$ (Sierou & Brady, 2002). At these small magnitudes, errors in (52) may be significant.

The Galilean error can be canceled by creating an internal boundary node (IBN) with a distribution set to $f_i^{(eq)}(\rho, \boldsymbol{u}_b)$ at every link endpoint inside the particle, as shown in Figure 9. The distributions from the IBNs then undergo the normal bounce-back operation, and the force is applied to the particle exactly canceling the error terms (MacMeccan, 2007, pp. 57–61). This operation is in addition to the usual bounce-back force, and is only applied to external traction forces. The equilibrium distribution in these internal nodes can be calculated in a link-by-link manner and only in the necessary directions for computational efficiency. Recently, Caiazzo & Junk (2008) have analyzed the bounce back operation using a diffusive scaling for the LB method (Junk, Klar & Luo, 2005) and recovered an identical error term. They propose a corrected bounce back operation by subtracting (42) from (33) directly. Both methods are equivalent.

Comparisons have been made between the predictions in (51) and (52) and actual simulations of a rigid FE sphere. In the two cases mentioned below, the sphere has a radius of 10 lattice spacings and $l_{FEA} = 2.0$. The simplest test case is a sphere suspended centered in a wall-bounded domain, in which the fluid, walls, and sphere have the same translational velocity. Physically, this is equivalent to a stationary sphere in a quiescent fluid. Such a case does not result in a force error since $\dot{\gamma} = 0$; however, it does result in an error in the stresslet calculation. Figure 12 shows the stresslet error as a function of translational velocity, and the results scale as U_x^2 as predicted by (52). The results for the corrected bounce back are not shown, but errors are $O(10^{-11})$ or less in all cases. Inset in the figure is a graphic of the particle showing the normal stress on the particle's surface, where warm colors denote high stress areas. The simulation domain is $64 \times 64 \times 64$ lattice nodes, but the results are insensitive to domain size since the fluid distributions never depart from equilibrium. A net force of zero is recorded in all cases as predicted by (51) (not shown).

Next, a sphere is suspended centered in wall-bounded shear such that it rotates and translates, as shown on the right side of Figure 11. An error in the y-component of total force that increases linearly with both the shear rate and translational velocity is shown in the dependence of force on $U_x\dot{\gamma}$ in (51). These simulations measure the error in force directly by fixing the sphere in the y-direction only. All other degrees of freedom in motion are allowed. For the 3-dimensional simulation shown, the domain is $64 \times 128 \times 64$ lattice nodes. The top and bottom wall are initialized to

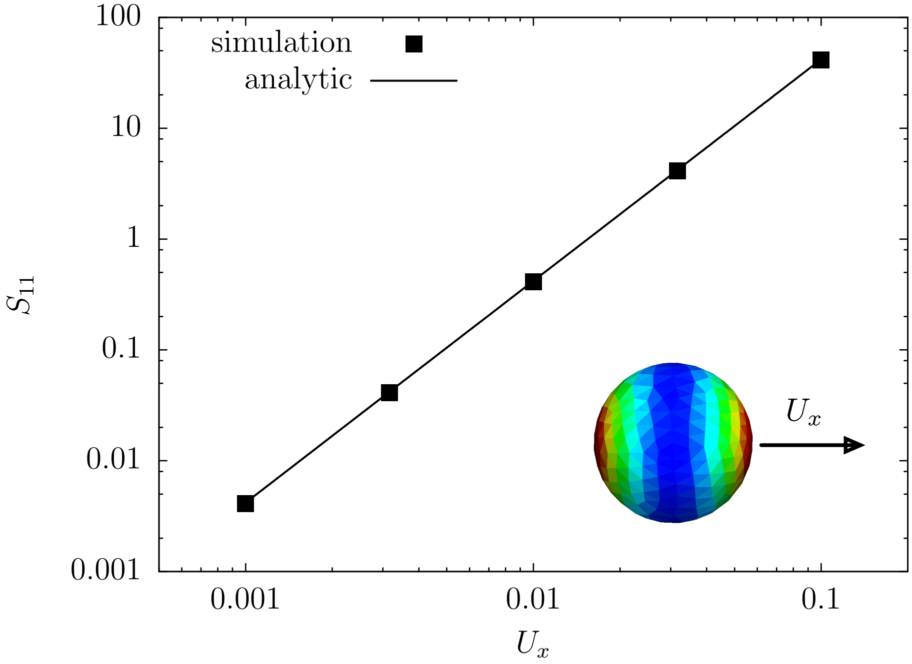

Figure 12: Effect of translational velocity on S_{11}. Inset in figure is a graphical depiction of exaggerated normal stresses on fore and aft surfaces of sphere. Not shown are results with the corrected bounce-back showing $O(10^{-11})$ error or less in all cases. Figure data from Clausen & Aidun (2009).

$U_x - \dot{\gamma}H/2$ and $U_x + \dot{\gamma}H/2$, respectively, where H is the domain height. Results for the y-component of force are shown in Figure 13(a,b) for fluid-filled particles, solid particles with corrected and uncorrected bounce-back operations, and the analytic predictions. Also shown are results for the external boundary force (EBF) method (Wu & Aidun, 2009), which is not based on the bounce-back procedure and thus does not display Galilean errors. In Figure 13a the translational velocity is held constant while the shear rate is altered, and in Figure 13b the shear rate is held constant while the translational velocity is altered. The force error shows a linear dependence on $U_x\dot{\gamma}$ in both cases, as predicted by (51). A slight drift occurs in the results, especially in Figure 13b where the translational velocity is increased. One possible explanation is the compressibility error which scales as U_x^2. Although the Galilean invariant portion of the error is corrected, compressibility artifacts still exist at high Mach number. Another possible source of error is the finite discretization of the particle. Nevertheless, the predicted scaling in the error term is demonstrated. Stresslet results agree with the scaling in (52) and echo the findings in Figure 12.

2.6 Conservation of particle volume

Although the LB method approximates the incompressible Navier–Stokes equations, the method is still weakly compressible with an equation of state of $P_f = \rho c_s^2$. For single-phase and rigid-suspension flows in which Ma $\ll 1$, the incompressible limit of the LB equation is maintained; however, the inclusion of fluid-filled deformable particles complicates the incompressible assumption. Two issues cause these complications: the lack of local mass conservation from the bounce-back method, and the mixing of fluid inside and outside the particle as LB nodes are covered and uncovered.

First, the bounce-back method results in a streaming of mass through the particle boundary for surfaces with a velocity component along the link direction. Although unintuitive, this requirement stems from the discrete velocities used in the fluid distribution. An adjustment in momentum for a given direction of the fluid distribution requires adjusting its mass; the velocity is fixed to the discrete values prescribed by $\boldsymbol{e}_i$. For rigid-body motion, the summation over all boundary links results in zero mass flux if the boundary location is taken as the link midpoint; however, the FE particles do not necessarily move in a rigid body fashion, and the boundary location is chosen as the actual intersection between link location and particle boundary. This issue is also highlighted when particles are in near contact and a mass transfer occurs, which results in slight fluctuations of the particle's mass with no long-term drift (Nguyen & Ladd, 2002). The solution proposed in Nguyen & Ladd (2002) keeps a tally of the mass transferred through the boundary followed by a correction step that adjust the mass by altering the distributions of fluid nodes adjacent to the particle border. Second, as the particle traverses the underlying Eulerian fluid lattice, fluid nodes are covered and uncovered; consequently, an intermixing between interior and

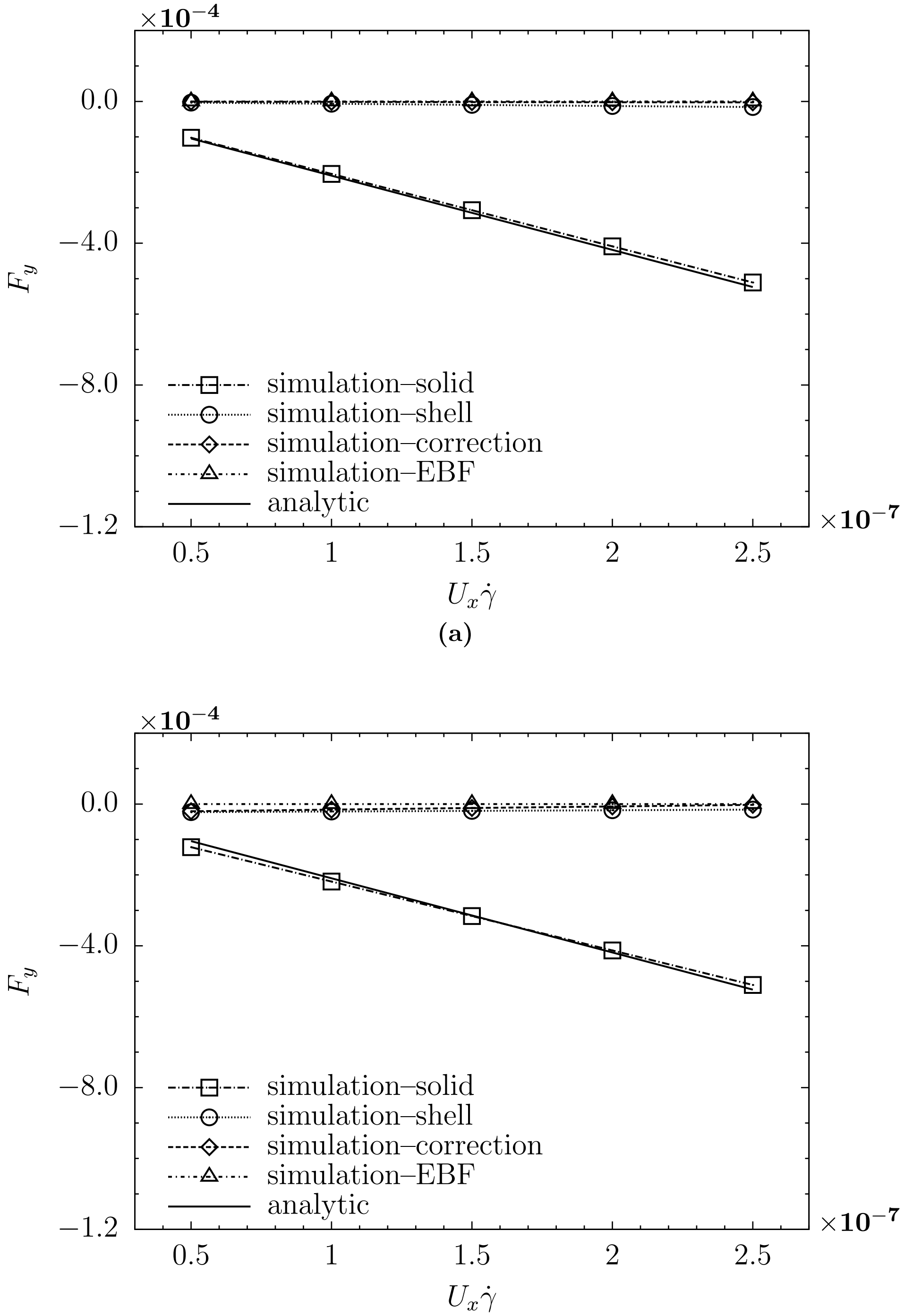

(a)

(b)

Figure 13: Force error for sphere suspended in simple shear. In (a), the translational velocity is constant at 0.01, and the shear rate is changed. In (b), the translational velocity is varied while the shear rate is held constant at 2.5×10^{-5} inverse time steps. Figure data from Clausen & Aidun (2009).

exterior fluids occurs such that a particle cannot hold a difference in density across its boundary. The timescale of this mixing is inversely proportional to the translational velocity of the particle.

The interaction of an elastic particle with these two effects requires corrections to the LB method. For an initially spherical capsule centered in shear, deformation requires either an increase in membrane surface area or decrease in particle volume. Since the LB method is weakly compressible, approximate conservation of particle volume is maintained by a slight decrease in particle volume, which increases the interior fluid density and, hence, pressure. As seen in Figure 14, this increase in pressure (density) serves to conserve volume efficiently over short timescales; however, fluid mixing that occurs during node covering and uncovering releases this pressure gradually. As a result, particle volume decreases over time. In addition to particle volume conservation, the mean interior and exterior fluid densities have a large effect on the calculation of the particle pressure. Since particle pressures are of the order $\mu\dot{\gamma}$ (Sierou & Brady, 2001; Kulkarni & Morris, 2008) or $\sim 10^{-5}$ in lattice units, a deviation in the mean of the exterior fluid density of $O(10^{-5})$, would obscure the particle pressure calculation.

To ensure proper calculation of the particle pressure, the density of both interior and exterior nodes is adjusted at every time step such that the mean density of each is unity. This normalization is achieved by summing both interior and exterior fluid nodes to calculate a mean density, then applying a per-node adjustment, $\Delta\rho$, to adjust the mean to unity. This adjustment takes the form

$$f_i^{\Delta\rho} = w_i \Delta\rho. \tag{53}$$

Recalling the following constraints on the lattice weights,

$$\sum_{i=0}^{Q} w_i = 1, \quad \sum_{i=0}^{Q} w_i \boldsymbol{e}_i = 0, \text{ and } \sum_{i=0}^{Q} w_i \boldsymbol{e}_i \boldsymbol{e}_i = c_s^2 \mathbf{I},$$

the moments of the distribution function ensure that only density and pressure are

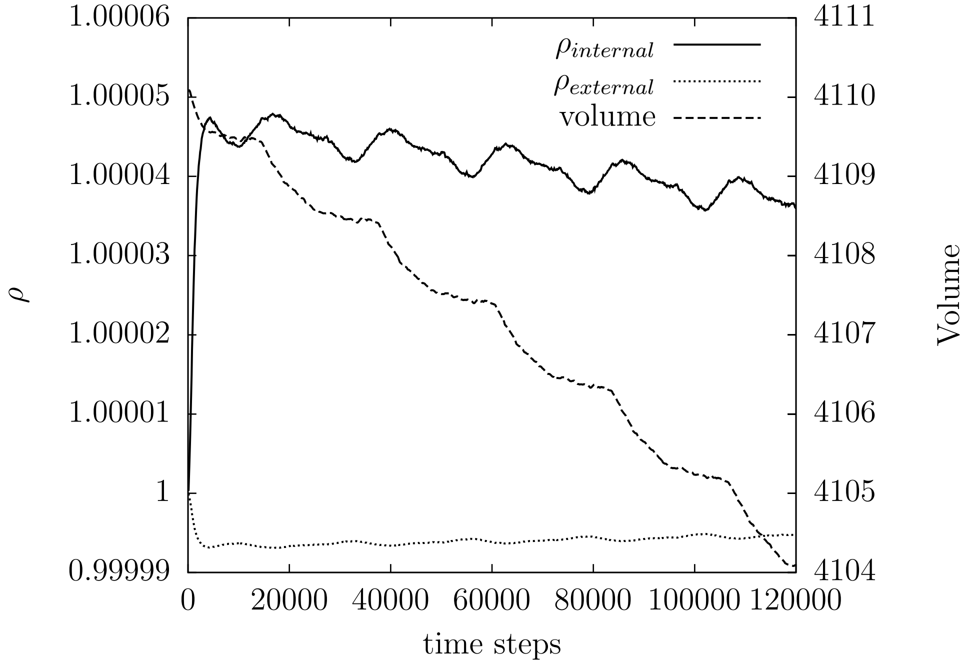

Figure 14: Isolated capsule in shear showing gradual change in volume caused by mixing of interior and exterior fluid.

altered, shown as

$$\sum_{i=0}^{Q} w_i \Delta\rho = \Delta\rho, \quad \sum_{i=0}^{Q} w_i \Delta\rho \boldsymbol{e}_i = 0, \quad \sum_{i=0}^{Q} w_i \Delta\rho \boldsymbol{e}_i \boldsymbol{e}_i = \Delta\rho c_s^2 \mathbf{I} = \Delta P \mathbf{I}.$$

Without any other steps, the density normalization results in an equal interior and exterior fluid pressure, thus particle volume conservation is not maintained. Therefore, in addition to the density normalization, a volume correction algorithm is added in which the bounce-back routine is altered to create an artificial pressure force that resists a change in volume. Thus, the boundary force calculated via the bounce-back operation (33) for the link endpoint inside the particle is altered as

$$\boldsymbol{F}^{(b,\Delta P)} = 2\boldsymbol{e}_i \left[f_i(\boldsymbol{r}, t^+) + f_i^{\Delta P} - 3\rho\omega_i \boldsymbol{u}_b \cdot \boldsymbol{e}_i \right], \tag{54}$$

where $f_i^{\Delta P}$ is a static pressure adjustment defined as

$$f_i^{\Delta P} = w_i \rho_0 \left(\frac{V_0}{V_p} - 1 \right),$$

where ρ_0 is the initial particle density, V_0 is the initial particle volume, and V_p is the instantaneous particle volume. This correction is only applied to the force acting on the particle for distributions being bounced inside the particle. The fluid distributions (32) are not altered. During an isolated capsule test identical to that in Figure 14, the volume corrected capsule experienced volume changes less than 0.003%, and at 40% volume fraction, the experienced volume change was less than 0.03%. Density normalization and constraining volume has little effect on the rheology, as shown in Figures 15(a and b), except for the large shift in particle pressure (Figure 15b). The particle pressure is incorrectly reported in the uncorrected case because the decrease in particle volume causes a decrease in external fluid density.

2.7 Model Problems

In this section several model problems are presented to demonstrate the validity of the hybrid LB/FE methodology. These model problems will probe the behavior of the fluid–solid interaction and the performance of the FE modeling. Choosing a FE mesh size small enough for accurate particle dynamics, yet coarse enough for the efficient simulation of hundreds of particles is crucial. In addition to the validation shown here, a detailed comparison of isolated capsule dynamics will be discussed in chapter 4, and dense suspension results in chapter 5.

2.7.1 Settling particle in a channel

In this problem, particles discretized with a FE mesh are allowed to settle under the influence of gravity in a large square channel. Results are compared with the experimental results of Miyamura, Iwasaki & Ishii (1981). As in the numerical simulations of Aidun et al. (1998), the inlet velocity is set to zero, and a body force accelerates the particle towards a terminal velocity, U, with an initial position > 200 lattice units from the inlet. The velocity has been normalized by the unbounded Stokes flow solution,

$$U_0 = \frac{M g_{grav}}{6\pi\mu a}, \tag{55}$$

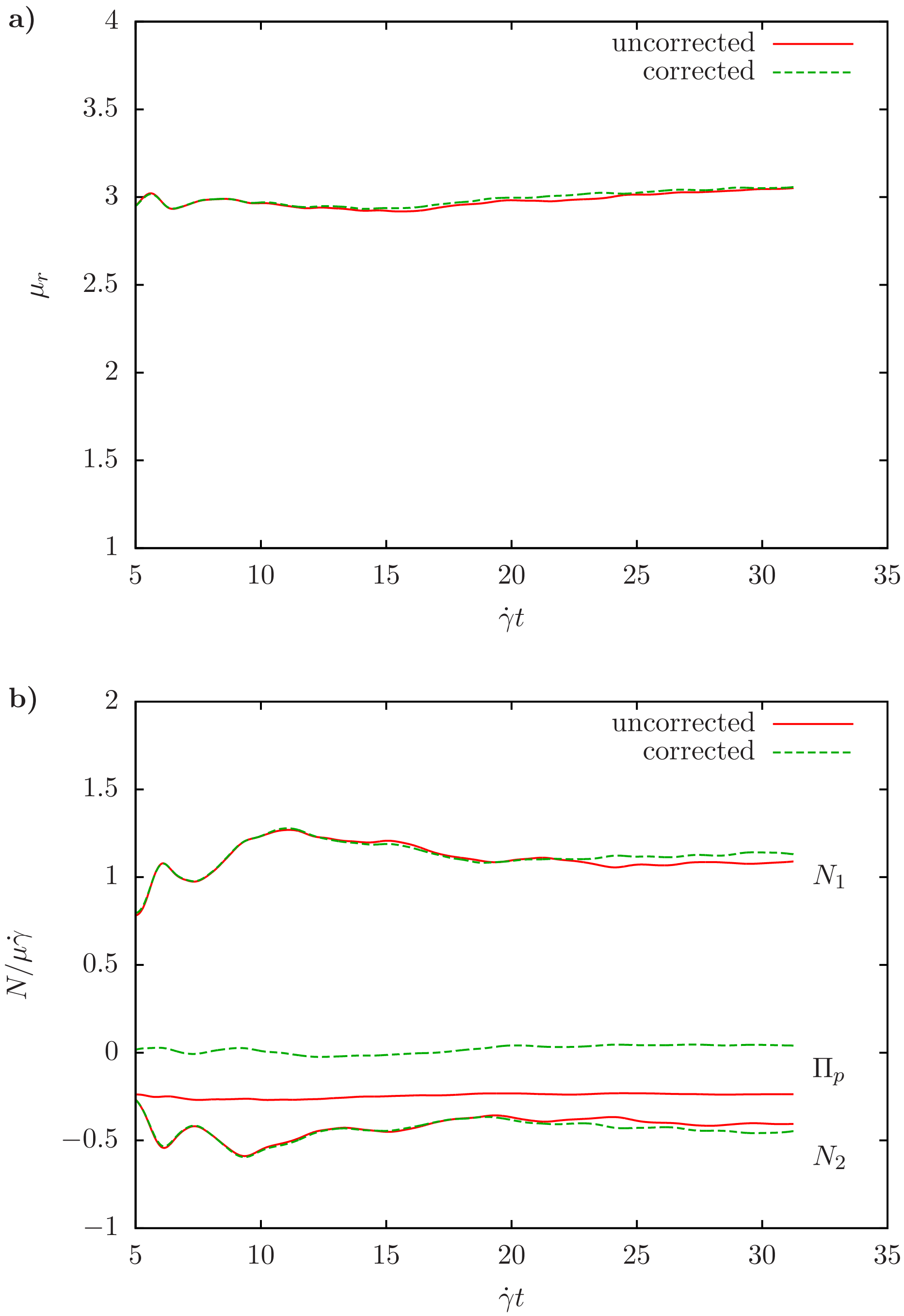

Figure 15: Time averages for 25 capsules in unbounded shear with $\mathrm{Ca}_G = 0.03$. (a) relative viscosity, (b) normal stress differences and particle pressure.

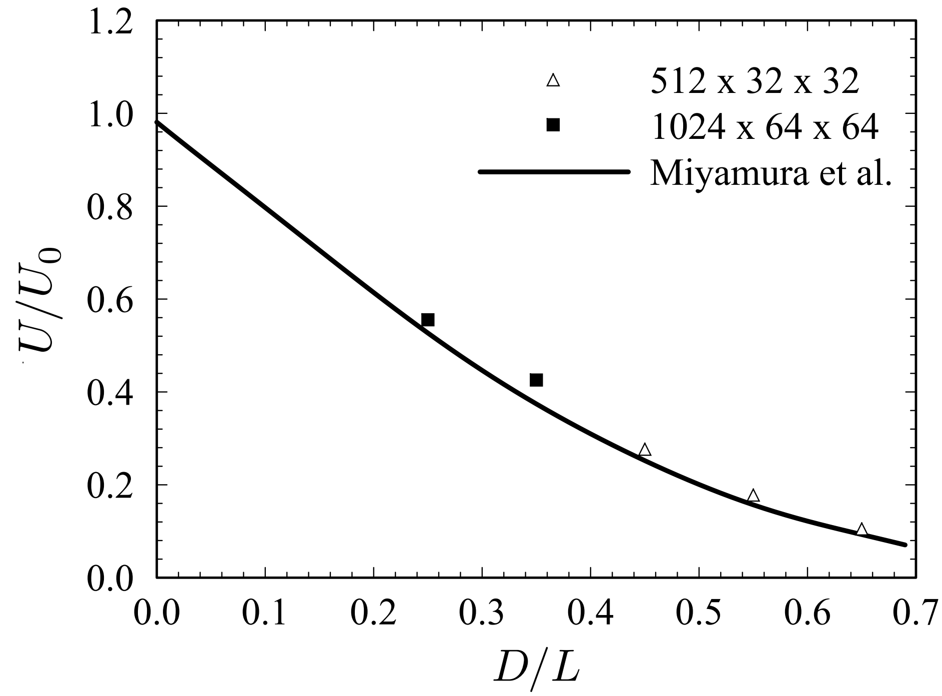

Figure 16: The settling of rigid meshed spheres in a square channel. Figure from MacMeccan et al. (2009).

where M is the mass of the particle, and g_{grav} is the acceleration due to gravity. The results are plotted against D/L, where D is the particle diameter and L is the channel width. The particle is rigid and does not undergo deformation. Two levels of fluid discretization are used, $512 \times 32 \times 32$ and $1024 \times 64 \times 64$, and the size of the sphere is adjusted to achieve the appropriate D/L. The FE mesh size falls within $1.5 < l_{FEA} < 2.2$. Good agreement is seen for all D/L.

2.7.2 Stresslet for isolated sphere

The next validation determines the dilute-limit stresslet for an isolated rigid sphere. The stresslet is calculated via (6) by summing over all the link-wise boundary forces (33) for external fluid nodes. This value is compared with the analytical prediction for the stresslet, $\mathbf{S} = 20/3\pi\mu a^3\mathbf{E}$. Simulations are performed in wall-bounded shear with a variety of particle meshes for a particle radius of 10 lattice spacings, with the

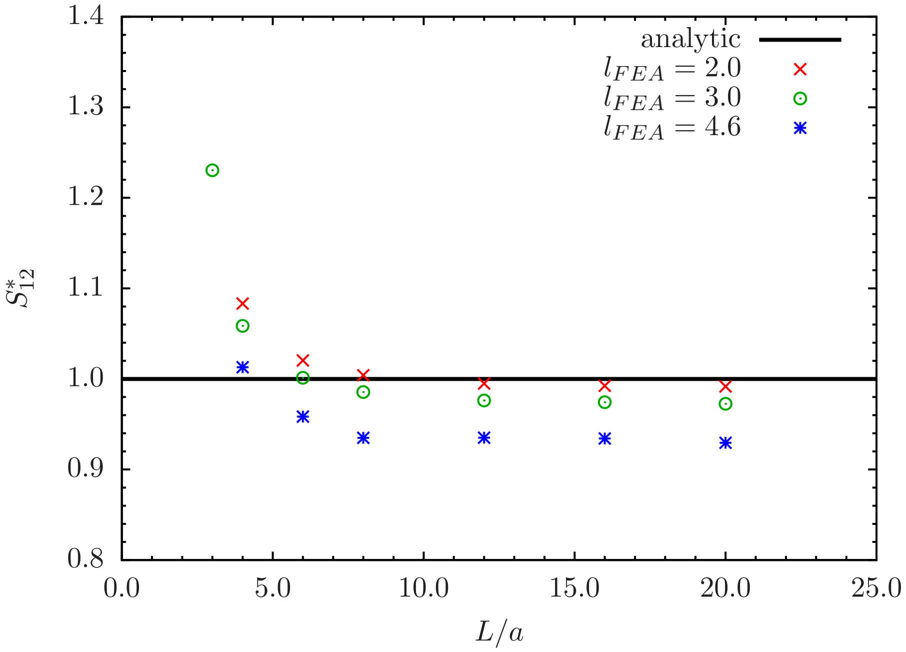

Figure 17: S_{12} component of the stresslet normalized by the dilute-limit isolated sphere value.

results shown in Figure 17. The simulation domain is increased until the the wall-effects are negligible. Coarse meshes (large l_{FEA}) underpredict S_{12}, which is likely caused by the smaller volume occupied by these particles. The radius is calculated by the smallest sphere that can contain all FE nodes, which does not change with discretization levels, but the volume does slightly. Nevertheless, $l_{FEA} = 2.0$ results in errors less than 2%.

2.7.3 Periodic arrays of spheres

For a simple cubic arrangement of spheres, the relative viscosity is known analytically as a function of the volume fraction (Zuzovsky, Adler & Brenner, 1983; Nunan & Keller, 1984). Simulations are performed with 8 rigid spheres of radius 10 in a simple cubic arrangement with the Lees–Edwards boundary condition. Sphere locations are fixed, and the solid and fluid velocities are allowed to relax to a steady value. Results are plotted in Figure 18a along with low ϕ and $\phi \to \phi_m$ asymptotic expansions by

Hofman, Clercx & Schram (2000). The maximum packing volume fraction is $\pi/6$ for a cubic array of spheres. Results include cases with no subgrid modeling and the lubrication model with no contact cutoff, with little difference in the results at $\phi < 0.5$.

The spin viscosity can also be calculated for a cubic array of spheres. As shown in Figure 18b, 8 spheres are initialized with a fixed position and angular velocity. The torque is allowed to relax to a steady value, where the torque on an individual sphere is related to the spin viscosity via

$$\frac{\boldsymbol{T}_V}{r^3} = \mu \eta_r \boldsymbol{\Omega}, \tag{56}$$

where $\boldsymbol{T}_V$ is the torque per unit volume, r is distance between particles, η_r is the spin viscosity, and $\boldsymbol{\Omega}$ is the fixed angular velocity. Asymptotic expansions of the spin viscosity are from Hofman, Clercx & Schram (1999). As in the shear viscosity case, little difference is seen between the no subgrid and lubrication model results at $\phi < 0.5$. In both Figures 18(a and b), FE mesh discretization is $l_{FEA} = 2.0$.

2.7.4 Transient behavior of spherical membrane

The transient inflation of a spherical capsule subjected to internal pressure tests the FE model and fluid–solid coupling for accuracy. In this test, the sphere is subject to a step-wise increase in internal pressure, which is generated by increasing the LB density for interior fluid nodes according to the LB equation of state, $P_f = \rho c_s^2$. The simulations are performed in a triply-periodic domain of size $100 \times 100 \times 100$ LB nodes, and the sphere has an initial radius of 10 LB nodes.The results are shown in Figure 19. The steady-state deformation is given analytically by Young & Budynas (2002) as

$$\Delta a = \frac{P_f a^2 (1 - \nu_p)}{2 E_y t_m}. \tag{57}$$

After the step increase in internal pressure, the sphere undergoes an oscillation that is damped by the presence of the LB fluid, with a period of oscillation given by (Buxton,

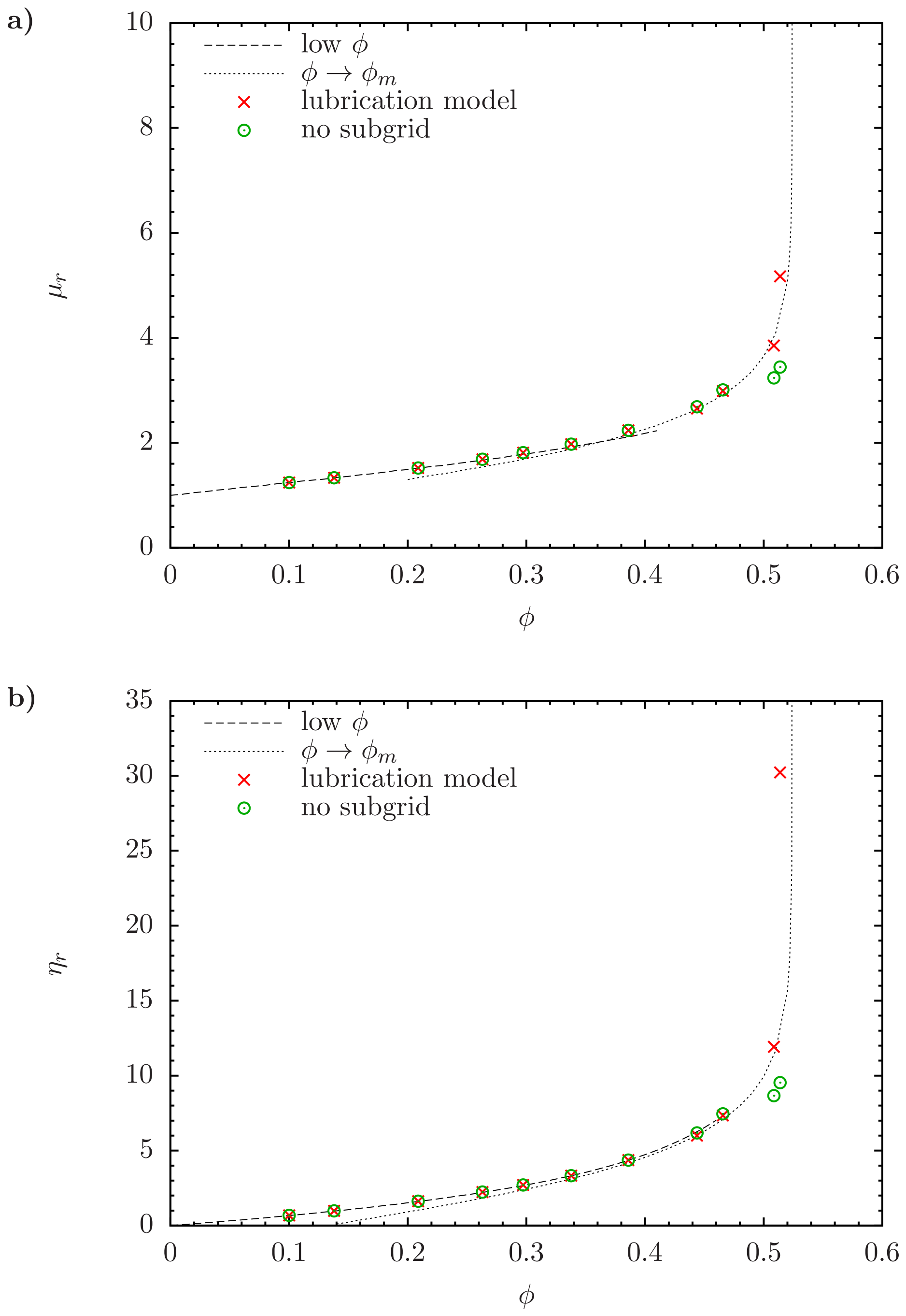

Figure 18: Simulation results showing the (a) relative suspension viscosity and (b) spin viscosity for a cubic array of rigid spherical particles.

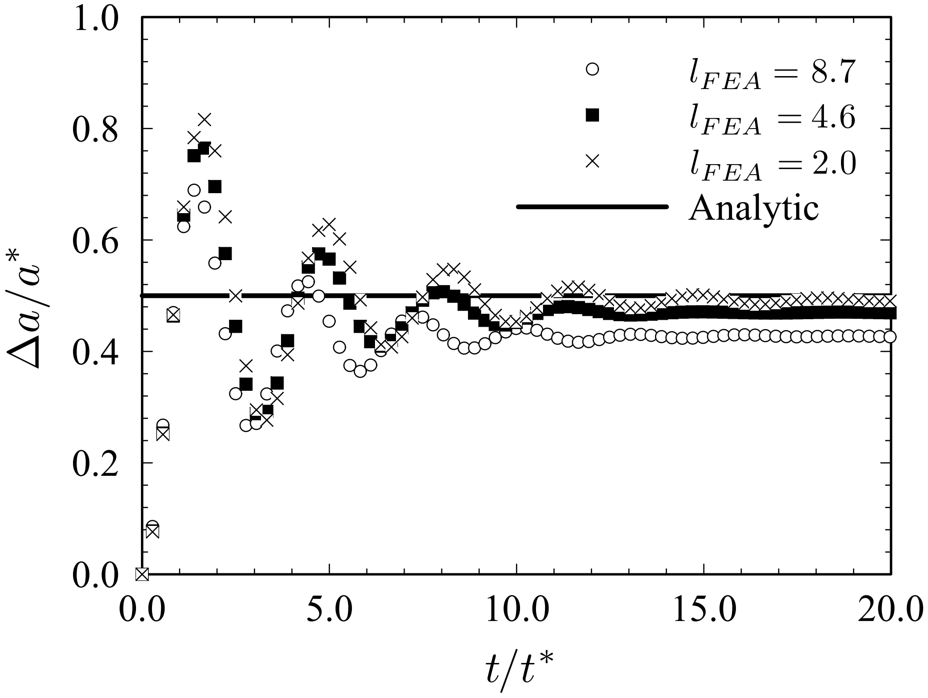

Figure 19: Transient response of spherical capsules inflated to pressure P_f using the LB method. Figure from MacMeccan et al. (2009).

Verberg, Jasnow & Balazs, 2005)

$$\frac{T}{t^*} = \pi\sqrt{2(1-\nu_p)}, \tag{58}$$

where the nondimensional time scale is given as $t^* = a\sqrt{\rho_s/E_y t_m}$. The radius is scaled by $a^* = Pa^2(1-\nu_p)$. As the FE discretization of the sphere increases (l_{FEA} decreases), the simulation results agree well with the analytical steady-state deformation. The period as measured from the graph is ~ 3.25, which compares well with the prediction of 3.3 from (58).

2.7.5 Lubrication

To show a comparison between the LB method with no subgrid modeling, the method of MacMeccan et al. (2009), and the newly proposed lubrication correction, simulations are performed for a variety of particle–particle and particle–wall interactions with the results shown in Figures 20(a,b) and Figures 21(a,b). Simulations in these figures are run using a particle with $l_{FEA} = 2.0$, $a = 10$, Re $= 0.06$ for the largest gap spacing, and no contact modeling or cutoff gap. Particles are given an initial velocity, and their locations are fixed as the fluid is allowed to relax to a steady solution. These simulations represent a best-case scenario for the lubrication model. In dense suspensions, stability must be maintained by introducing a cutoff parameter that necessarily causes deviation from the strictly hydrodynamic case. Chapter 5 will discuss the impact of lubrication modeling on dense suspension rheology.

For Figure 20a, two particles are approaching along their centers with constant velocity, and the resultant repulsive force is plotted. The error bars represent one standard deviation over 12 simulations, where the first particle's location and orientation are random, and the second particle has a random orientation and fixed spacing (ε) from the first particle. Analytical results for the lubrication theory of Cox (1974) and the matched near- and far-field results of Jeffrey & Onishi (1984) are shown. Gaps corresponding to no subgrid modeling ($\varepsilon/a > 0.1$) show almost zero scatter in the results, and closely follow the analytical results of Jeffrey & Onishi (1984). At smaller gaps, the case without subgrid modeling is incapable of recovering the singular behavior and shows large errors below one lattice spacing. The previous model of MacMeccan et al. (2009) correctly reproduces singular behavior; however, the effect is much too weak, likely caused by the incorrect approach velocity. Additionally, the smoothing around the cutoff results in especially poor performance at gaps just under one lattice spacing (see $\varepsilon/a = 0.05$). Multiple simulations were not run for the MacMeccan and no subgrid cases, so error bars are not present. The model in (40) follows the analytical results closely, and the uncertainty introduced through particle and link meshes is seen in the deviation of lubrication forces at smaller gaps. The new model break down at gaps approaching 0.1 lattice units ($\varepsilon/a = 0.01$) and beings to underpredict the lubrication forces.

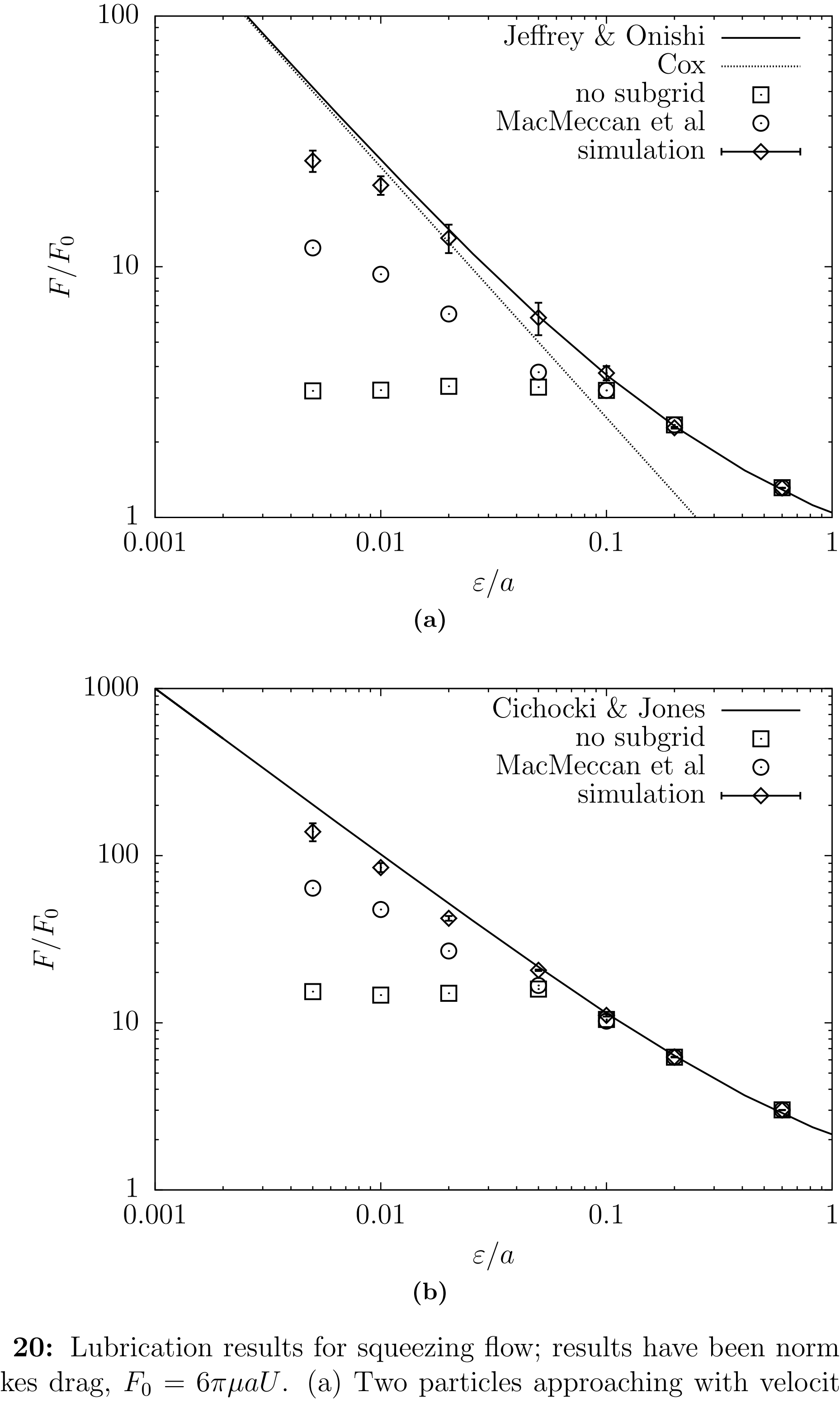

Figure 20: Lubrication results for squeezing flow; results have been normalized by the Stokes drag, $F_0 = 6\pi\mu aU$. (a) Two particles approaching with velocity U. (b) Single particle approaching wall in normal direction with velocity U.

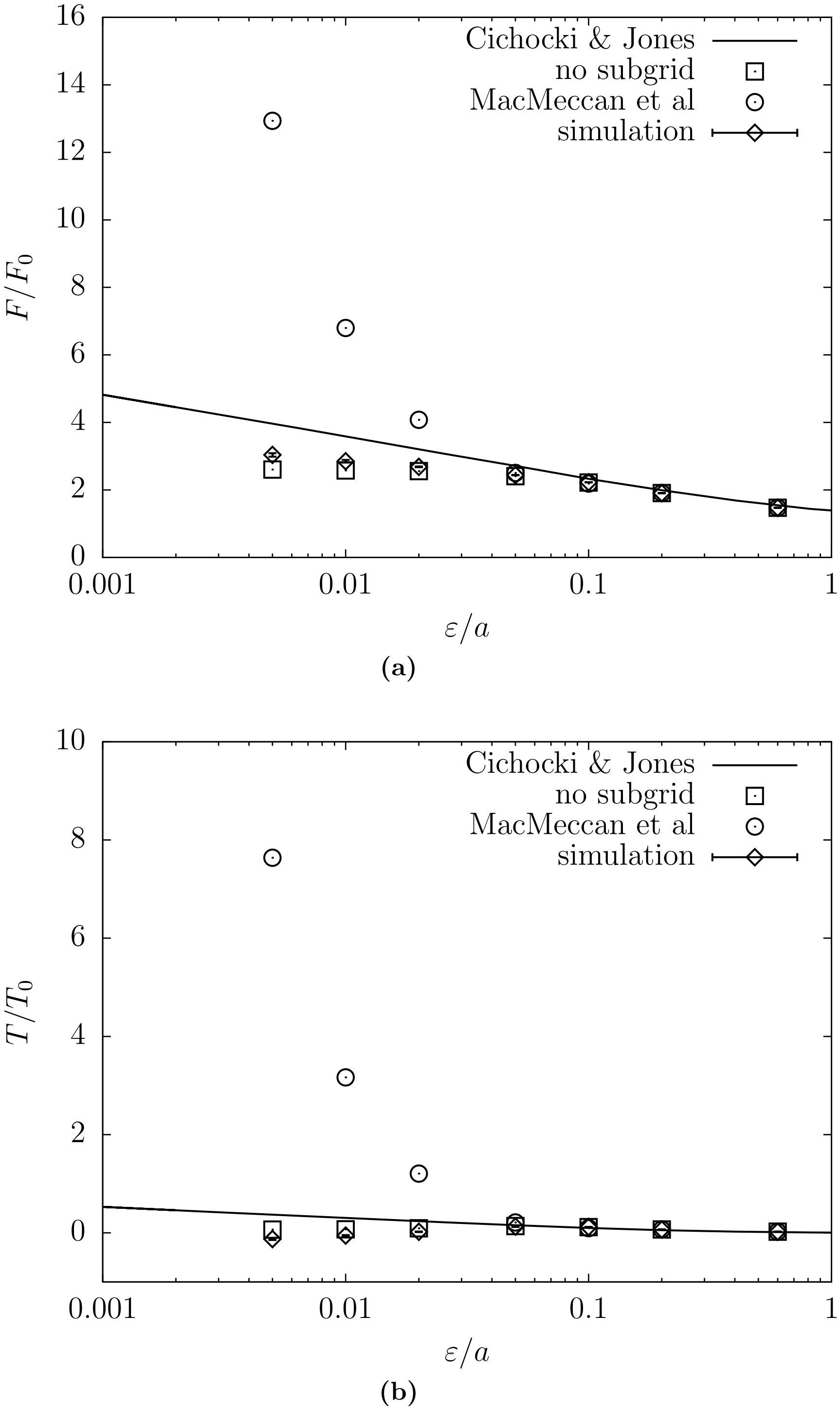

Figure 21: Lubrication results for a single particle sliding parallel to a fixed wall showing (a) force on the particle normalized by $F_0 = 6\pi\mu aU$ and (b) torque on particle normalized by $T_0 = 8\pi\mu a^2U$.

Figure 20b corresponds to the case of a sphere approaching a wall from the direction normal to the wall. Again, the error bars represent one standard deviation over runs in which the particle's orientation and position parallel to the wall are random. The analytical results are taken from the multireflection-based method of Cichocki & Jones (1998). Again similar trends are seen, with the new lubrication model outperforming previous results; however, the new model slightly underpredicts the analytical results at small gaps, which may be a result of the much larger magnitudes seen in sphere-wall interactions.

Next, we consider the case of a sphere sliding near a wall, where the sphere is moved tangentially to a wall with a fixed velocity and is not allowed to rotate. The corresponding force in the direction of motion and torque are plotted in Figures 21(a and b). In these plots, the overestimation of the shear component of lubrication in MacMeccan et al. (2009) is clearly seen, which shows much stronger singular nature than the $O(\ln 1/\epsilon)$ predicted analytically. The newly proposed model attempts to neglect shear components of lubrication; consequently, the results tend to follow the no subgrid modeling cases. Slight deviation from the no subgrid case is seen because $\boldsymbol{n}_{avg}$ may have a small component parallel to the wall for surfaces in near contact. Furthermore, $\boldsymbol{n}_{avg}$ is no longer colinear with the particle's center, thus creating the slight decrease in torque for the simulation data in Figure 21b.

Other important parameters that affect lubrication include the level of FE mesh discretization, l_{FEA}, and particle size, a. At the small gaps seen during near contact, the effect of surface roughness will undoubtedly be large and will serve as a limiting factor, in addition to the particle size, to the gaps that can be resolved with this method. In Figure 22a, the particle–particle results in Figure 20a are repeated for several values of l_{FEA} with $a = 10$, and in Figure 22b, the effect of altering the particle radius while fixing $l_{FEA} = 2.0$ is shown. Data without error bars are subject to uncertainty as discussed previously. Again, the plots in Figure 22 are without contact modeling ($g_c = 0$). In general, the finer meshed particles resolve the lubrication hydrodynamics to smaller gaps, as expected. For the most coarsely meshed particle, $l_{FEA} = 4.0$, large errors occur at gaps near the LB grid spacing. Reasonably accurate results are seen for $\varepsilon/a > 0.02$ for $l_{FEA} \leq 2.0$. Altering the particle radius has as similar effect on lubrication resolution, with the larger radii predictably yielding better results. Also, the ability of the LB method to resolve far-field hydrodynamics with very poorly meshed ($l_{FEA} = 4.0$) or very small ($a = 5.0$) particles is shown.

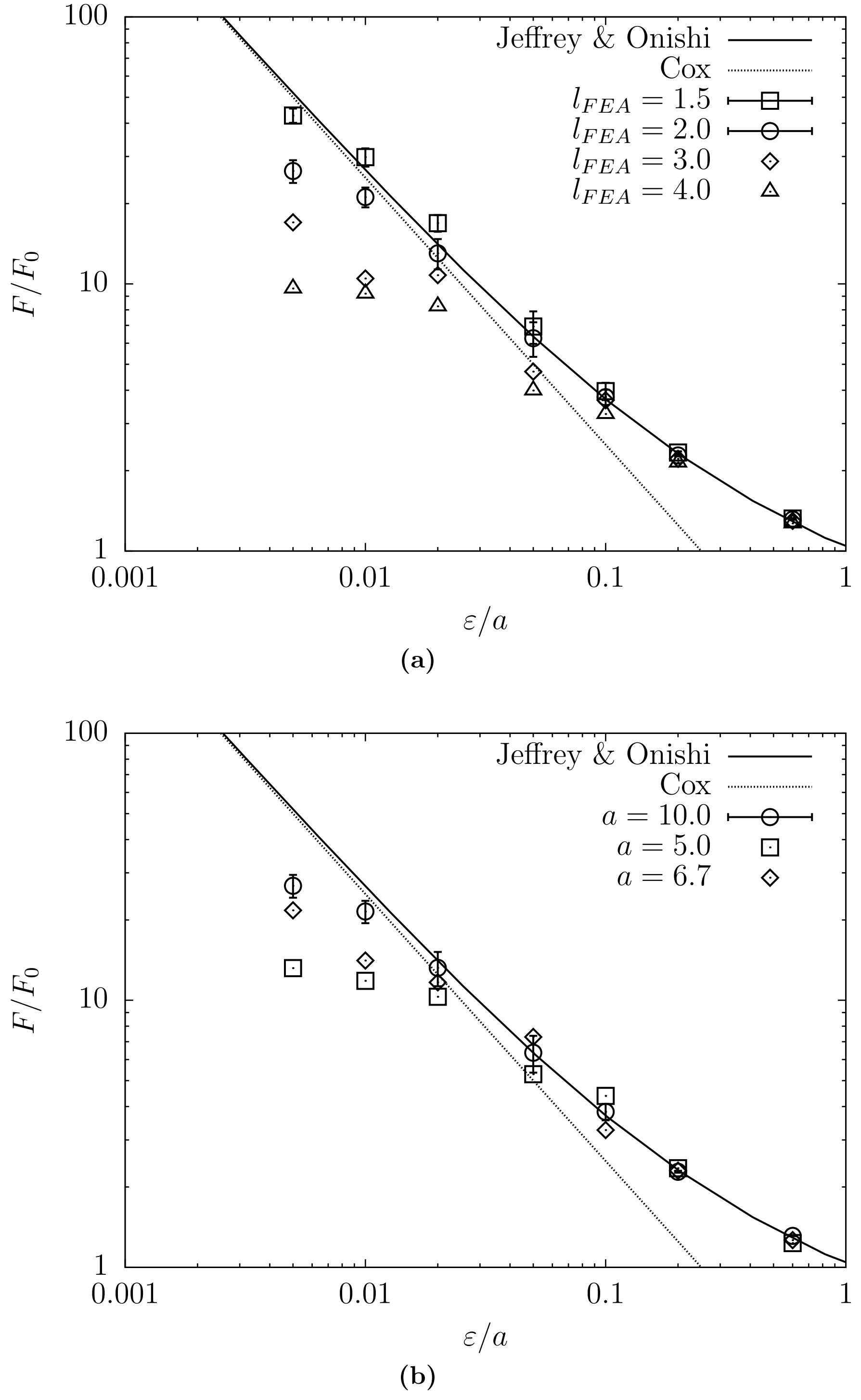

Figure 22: Lubrication results for two particles approaching with velocity U; (a) l_{FEA} is varied and $a = 10$; (b) a is varied and $l_{FEA} = 2.0$.

CHAPTER III

PARALLEL IMPLEMENTATION AND SCALING

3.1 Motivation and domain decomposition

Accurately describing the rheology of capsule suspensions requires approximating the ensemble average in the particle stress equation (5), i.e., a sufficiently large number of particles must be sampled for a sufficiently large amount of time. Although simulations of the size necessary to obtain reasonable statistics can be performed on a single workstation computer, these simulations can take several weeks to perform. Furthermore, accurate reconstruction of rheology requires a parametric sweep of the parameters of interest. As a result, relying on a serial method that can only be run on single computers is not feasible. Accordingly, the method discussed in chapter 2 has been extended to allow simulations on large-scale distributed computational clusters (Clausen et al., 2010).

The parallel implementation uses the message passing interface (MPI), in which messages (data) are explicitly passed between computation nodes. The current MPI implementation discretizes the problem domain into a set of Cartesian subdomains using the standard Cartesian topology functions defined by MPI. Parallel implementation of the fluid phase is fairly straightforward: one set of ghost nodes is created exterior to the domain, and these nodes are repopulated at every time step via `MPI_Sendrecv` function calls in the Cartesian directions. These ghost nodes then propagate the solution into the neighboring domains. Figure 23a depicts a model simulation domain, shown as the central bold square, with a series of LB nodes. A set of fluid nodes is highlighted in red, and communication occurs to the ghost nodes of the domain at right. This scheme is repeated for the remaining Cartesian directions,

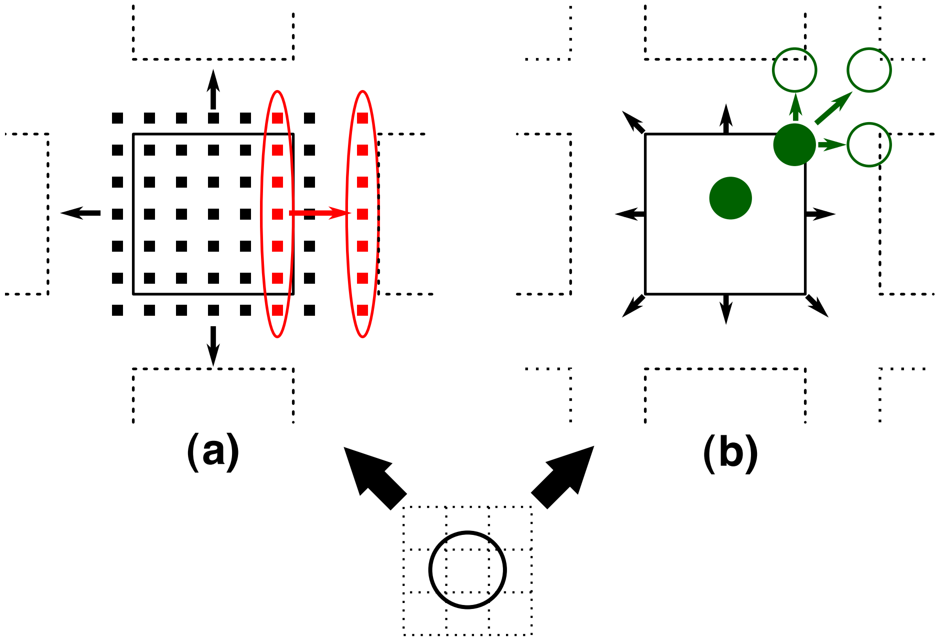

Figure 23: Schematic of MPI communication algorithm showing a simplified 2-dimensional Cartesian topology. Communication is split into two phases: (a) the fluid is communicated in each Cartesian direction by exchanging a set of ghost nodes, and (b) a list of particles near the subdomain border is synchronized with neighboring subdomains via `MPI_Sendrecv` calls, then particles are sent in a point-to-point fashion using nonblocking `MPI_Isend` and `MPI_Irecv`. Figure from Clausen et al. (2010).

for all subdomains. This communication occurs once per time step.

With the solid phase, the particles are tracked as Lagrangian entities that are "handed-off" between subdomain ranks as they travel through the simulation domain, shown in Figure 23b. For a given time step, a list of particles near the subdomain border is created for each subdomain, and this list is synchronized among neighboring ranks by sending it along all possible directions (8 for 2-dimensions and 27 for 3-dimensions) through `MPI_Sendrecv` operations. Next, the particle information necessary to perform the bounce-back coupling is sent in a point-to-point process using nonblocking send and receive operations from the rank where the particle center resides to all ranks the particle is visible within, where visible particle images are shown as outlines in Figure 23b. After the fluid–solid boundary condition is applied, the resultant forces are communicated back to the originating rank and appropriately summed. All dynamics are calculated by the subdomain where the particle's center of mass is located. The particles are stored as a C array of pointers, which are dynamically allocated only if the particle is visible, thus keeping the memory footprint small and scalable. A flow chart showing the order of communication and computation is shown in Figure 24.

3.2 Scaling on the BlueGene/P architecture

The MPI implementation was optimized using the TAU[1] analysis package. Scaling studies were performed on two BlueGene/P (BGP) systems at Argonne National Laboratory: Surveyor, a debugging and porting machine, and Intrepid, the production machine (Clausen et al., 2010). The details of the Intrepid system housed there are as follows[2]:

---

[1] http://www.cs.uoregon.edu/research/tau/home.php

[2] http://www.alcf.anl.gov/resources/index.php

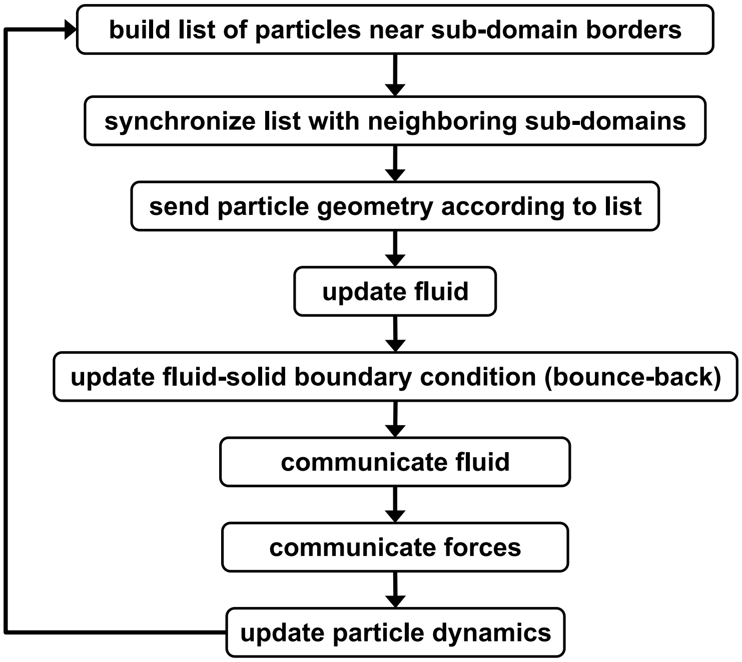

Figure 24: Flowchart for single time step iteration highlighting communication and major computations. Figure from Clausen et al. (2010).

- peak performance of 557 Teraflops with 40,960 compute nodes (40 racks of 1,024 nodes)
- each node contains 4 cores, with each CPU being an IBM PowerPC450 (850 MHz) for a total of 163,840 processor cores (1 Rack = 4,096 cores)
- 2 GB RAM per node (80 TB total)
- 3-dimensional torus point-to-point communication interconnect network with 5.1 GB/s bandwidth (3.5 µs latency)
- collective network with 1.7 GB/s bandwidth per port with 3 ports per node (2.5 µs latency)

When using a BGP system there are several options when submitting large parallel tasks. The first option is *smp* (symmetric multiprocessor) mode, which sends a single message passing interface (MPI) rank to each node, which leaves three of four cores unused in the absence of multi-threading. This configuration is helpful when a large memory footprint is required for each MPI task. The second option is *dual* using two cores on each node, and the third option is *vn* (virtual node) using all four cores of each node. Simulation results presented make use of both *smp* and *vn* modes for benchmark comparisons; however, all scaling results within a figure are run with the same mode. Due to the torus network for point-to-point communication, realistic benchmarks must be performed on a minimum of 512 nodes (1/2 rack) of BGP.

3.2.1 MPI communication overhead

Many of the MPI communication deficiencies associated with the simulation of $O(10,000)$ deformable particles are not obvious for simulations on 128–512 cores on smaller Intel-based resources. Any collective, i.e., not point-to-point, MPI operations become prohibitive when scaling beyond $O(1,000)$ cores.

Using TAU, the MPI communication overhead was determined for single- and multiphase simulations in a 512^3 cubical domain undergoing wall-bounded shear. The multiphase simulation included 13,824 deformable particles. The most demanding MPI functions for these simulations are summarized in Tables 1 and 2 including the number of calls, simulation time, and percentage of total simulation time. The use of TAU streamlined the optimization process by allowing detailed instrumentation without requiring laborious hand-coded timing routines; however, the values from TAU are estimates to the performance and may differ somewhat when a more optimized version is compiled without TAU instrumentation.

In Table 1, it is clear that the `MPI_Sendrecv` function is the most time-consuming communication routine and accounts for 2.4% and 10.1% of the total simulation time for single- and multiphase simulations, respectively. The percentage of time spent communicating increases when going from single- to multiphase simulations

Table 1: MPI function communication summary for 512^3 cubical single-phase simulation. Simulation was performed on 4,096 cores *vn* mode for 100 LB time steps. Total runtime was 158.9 seconds. Number of calls and time are the average per MPI process, with the standard deviation given by σ. Data are from Clausen et al. (2010).

MPI Routine	**Calls**	**Time (s)**	**σ (s)**	**% Total Time**
MPI_Cart_coords	601	0.004	0.000	0.003
MPI_Cart_rank	600	0.004	0.000	0.003
MPI_Sendrecv	600	3.867	1.314	2.434
MPI_Reduce	4	0.329	0.006	0.207
MPI_Barrier	1	0.720	0.072	0.453
MPI_Cart_create	1	0.320	0.083	0.201
MPI_Init	1	0.178	0.000	0.112
Totals:		5.42 sec		3.41%

from 3.4% to 15.6%. This increase is related to the increase in data communicated because of the inclusion of deformable particles. Furthermore, the addition of unequal numbers of particles to each subdomain causes load-balancing and synchronization problems, which increases the time spent in the blocking `MPI_Sendrecv` operation. Evidence of node balancing issues can be seen via the standard deviation, σ, for the MPI function calls in multiphase simulations. More specifically, in Table 2 we see that $\sigma = 15.1$ seconds for the `MPI_Sendrecv`, 9.28 seconds for `MPI_Recv`, and 5.18 seconds for `MPI_Waitall` for a simulation with a total core computing time of 496.9 seconds. These three operations are blocking in nature, i.e., all computational nodes must wait for the slowest node to finish, which creates the large deviation in times. One possible idea for decreasing the communication overhead would be dividing the particles evenly between all ranks, which would improve load-balancing; however, communication overhead would increase slightly since the particles would need to be communicated to the rank where the particle's center resides.

Table 2: MPI function communication summary for 512^3 cubical simulation with 13,824 deformable spheres. Simulation was performed on 4,096 cores *vn* mode for 100 LB time steps. Total runtime was 496.9 seconds. Number of calls and time are the average per MPI process, with the standard deviation given by σ. Data are from Clausen et al. (2010).

MPI Routine	**Calls**	**Time (s)**	σ **(s)**	**% Total Time**
MPI_Cart_coords	100001	0.569	0.014	0.115
MPI_Cart_rank	100001	0.552	0.014	0.111
MPI_Isend	15750	0.124	0.035	0.025
MPI_Sendrecv	11000	50.38	15.11	10.14
MPI_Irecv	9000	0.052	0.008	0.010
MPI_Recv	6793	21.65	9.279	4.357
MPI_Waitall	300	2.756	5.182	0.555
MPI_Send	43	0.030	0.022	0.006
MPI_Barrier	2	0.472	0.150	0.095
MPI_Cart_create	1	0.632	0.366	0.127
MPI_Init	1	0.187	0.000	0.037
Totals:		77.4 sec		15.6%

3.2.2 Memory scaling

Simulating a massive number of deformable particles requires a relatively large memory footprint; however, most Intel based HPC resources have sufficient memory headroom, typically in the range of 1–8 GB per core. The BGP architecture poses more stringent requirements since the resource used in this study has only 2 GB of memory per node equaling only 512 MB per core. The amount of memory required for single- and multiphase simulations is determined using TAU. Figure 25 shows the total memory usage simulations with a fixed subdomain size of 32^3 and the relative requirements of fluid and particles. The simulation on 512 cores with subdomains of 32^3 uses a total of 54.78 GB, and the fluid and solid phases use 22.51 GB and 32.27 GB, respectively. The better than ideal memory usage for 216 cores is caused by rounding to the nearest integer for the number of particles, which results in a slightly lower volume fraction. Memory requirements per node for subdomain sizes

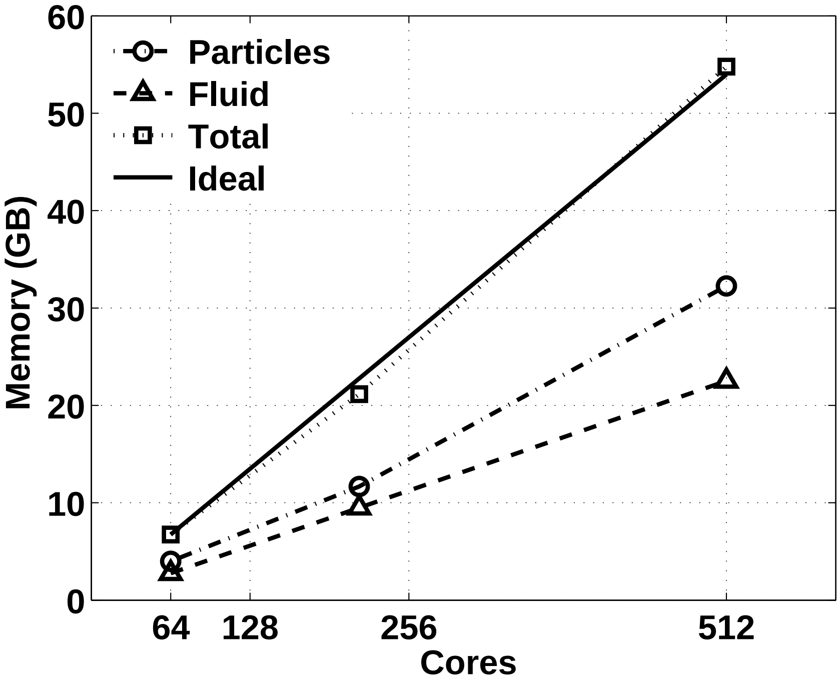

Figure 25: Memory usage vs. number of cores for a fixed sub-domain size of 32×32×32. Ideal corresponds to the total (fluid plus solid) memory footprint. Figure from (Clausen et al., 2010).

32^3 are modest, around 100 MB; however, the memory requirements place an upper limit on subdomain sizes. For example, a simulation of 64^3 requires ∼800 MB, which exceeds the available 512 MB of memory. Memory benchmarks are not attempted on the larger simulations; however, the largest weak-scaling multiphase simulation with 32,768 subdomains of 32^3 each does not have issues with memory headroom, which supports the near-linear scaling of the memory required.

3.2.3 Computational scaling

As mentioned previously, benchmark simulations on BGP systems can only be performed when the number of nodes used is ≥ 512 (1/2 rack) because of the 3-dimensional torus interconnect; however, 512 nodes equates to 2048 cores when simulations are run in *vn* mode. Scaling results are broadly split into two groups: strong and weak scaling. Strong scaling involves keeping the overall domain size constant while progressively dividing the domain into smaller subdivisions, each of which are computed on a separate processor core. Weak scaling involves keeping the subdomain size constant, and increasing the overall simulation size as the number of processor cores increases. The performance metrics used in this section to describe strong scaling results are *speedup*, *efficiency*, and the number of LB time steps obtained in a physical second of time, where $\mathcal{T}=$ LB time steps/second. The term *speedup* is defined as

$$\text{Speedup} = \frac{\text{Time to Solution for 512 nodes}}{\text{Time to Solution for } N \text{ nodes}}, \tag{59}$$

and *efficiency* is defined as

$$\text{Efficiency} = \frac{512}{N} \times \text{Speedup} \times 100\%. \tag{60}$$

Weak scaling is typically quantified by the overall runtime, which should ideally remain unchanged as the number of processor cores increases.

An initial study using a $1,024^3$ cube in wall bounded shear demonstrates the single-phase strong scaling of the LB code. Simulations are run for 1,000 time steps on 1 to 16 racks (4,096 to 65,536 cores) with mode *vn*. Figure 26(a) shows the results with a 74% single-phase efficiency when scaling from 1 rack to 16 racks. As a comparison, Vahala, Keating, Soe, Yepez, Vahala et al. (2008) reports nearly linear strong scaling when increasing the number of processors from 1,024 to 8,192 cores with a $1,024^3$ domain on a similar BG system for a magnetohydrodynamic LB formulation, whereas Figure 26(a) shows 87% efficiency for 32,768 cores. These simulations highlight the known ability of the LB method to scale efficiently on distributed memory computers. The amount of physical or wall time to compute a LB time step varies from 0.612 seconds to 0.026 seconds when the number of racks is increased from 2 to 16. This implies that a simulation of 500,000 time steps can be obtained in less than four hours in the absence of file input and output (I/O).

For the multiphase simulations, strong scaling results are given in Figure 26(b). The simulations are run on Intrepid with a 512^3 fluid domain at 40% volume fraction, which corresponds to 13,824 deformable spherical particles. The strong scaling simulations are run with mode *smp* (one core per node) to maximize available memory per node, which allows larger subdomain sizes and a larger range of scaling results. As a result, the number of cores per rack is different from the single-phase results presented in Figure 26(a). Simulations range from 1/2 rack (512 nodes) to 8 racks (8,192 nodes). Efficiency results hover around 50% for simulations less than 4 racks, then decrease to 31% for the last point. A load-balance issue between computational nodes is the believed culprit for this decrease in performance. As mentioned previously, the domain is discretized into Cartesian subdomains, and all particle dynamics are handled by the subdomain in which the particle resides. At large subdomain sizes, the relative number of particles varies by only a few percent between ranks. For example, the 1/2 rack case in Figure 26(b) corresponds to a subdomain size of 64^3, with approximately 27 particles per subdomain. A difference of a single particle present in two different ranks represents a load difference of approximately 3%. Conversely, at 8 racks, the subdomain size shown in Figure 26(b) is $32 \times 32 \times 16$ with approximately 2 particles per subdomain. A difference of a single particle now accounts for huge swings in computational load.

The load-balancing issue is particularly evident on the *BG/P* architecture since the slower per-processor speed requires smaller subdomains to achieve acceptable wall times. As a result, computations with subdomain sizes below 32^3 are not recommended until the particle dynamics can be further split among processors and the load balance issue resolved. For simulations performed on 8 racks, the ratio of physical time in seconds to LB time steps is approximately unity. This implies that a simulation of 500,000 LB time steps can be obtained in 5.5 days. As shown, the scaling of the single phase simulations is much more efficient than the multiphase

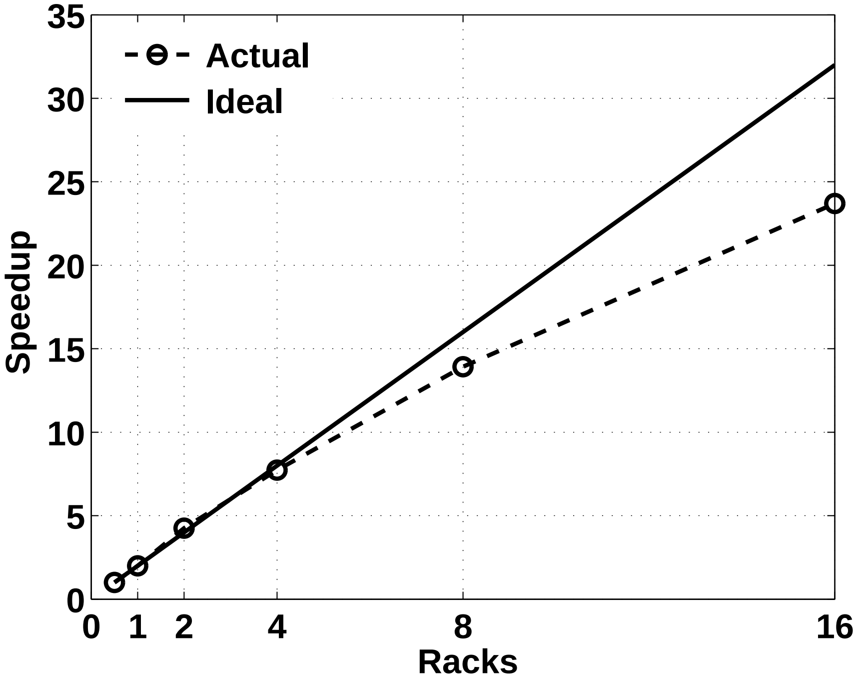

(a) Strong scaling (16 racks = 65,536 cores).

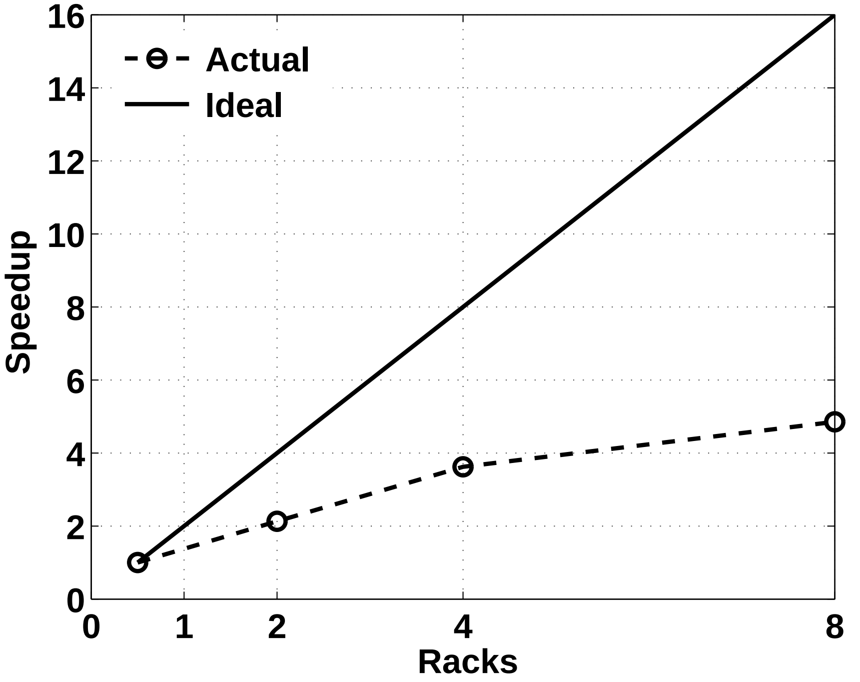

(b) Strong scaling (8 racks = 8,192 cores).

Figure 26: Strong scaling results for simulations performed on BGP. Results shown the (a) single-phase scaling for a 1024^3 domain in wall-bounded shear; mode is *vn*, and the (b) multiphase results for a 512^3 domain in wall-bounded shear; mode is *smp*. Figures from Clausen et al. (2010).

Table 3: Weak scaling results for single phase simulations. Simulations were computed in *vn* mode for 1,000 LB time steps, $\mathcal{T}$= LB time steps/second. Simulations were performed with a fixed subdomain size of 32×32×32. LB site updates per second (SU/s) are also given. Data are from Clausen et al. (2010).

Cores	Total Time (s)	LB Domain	$\mathcal{T}$	SU/s
4096	50.53	512×512×512	19.79	2.656×10^{9}
8192	51.27	1024×512×512	19.51	5.237×10^{9}
16384	45.25	1024×1024×512	22.10	1.186×10^{10}
32768	47.05	1024×1024×1024	21.25	2.282×10^{10}

simulation in similar sized fluid domains.

The weak-scaling results for the single-phase simulations are shown in Table 3. The normalized time step parameter $\mathcal{T}$ is fairly constant for all the simulation performed. Constant $\mathcal{T}$ represents ideal weak scaling, which implies no time penalty for increasing the overall simulation domain size as long as the per-processor load is the same. The weak-scaling results for multiphase simulations are shown in Figure 27 and are performed with a subdomain size of 32^3, with a maximum domain size of $1,024^3$ and $110,592$ particles. All simulations are run with mode *vn*. Although the method does not show ideal scaling, it does scale in a weak linear manner, and simulations with $O(100,000)$ particles are feasible. The nonideal weak scaling may be attributable to load-balancing issues as in the strong scaling case. Although the subdomain sizes are fixed, more subdomains lead to larger statistical variation in the number of particles in each domain, thus causing a decrease in performance. Also, any remaining portion of serial code start to become insignificant at simulations of this size. Unfortunately, extensive exploration of these results would require much more time and instrumentation. Simulations of the size required for this thesis are considerably smaller than these scaling runs.

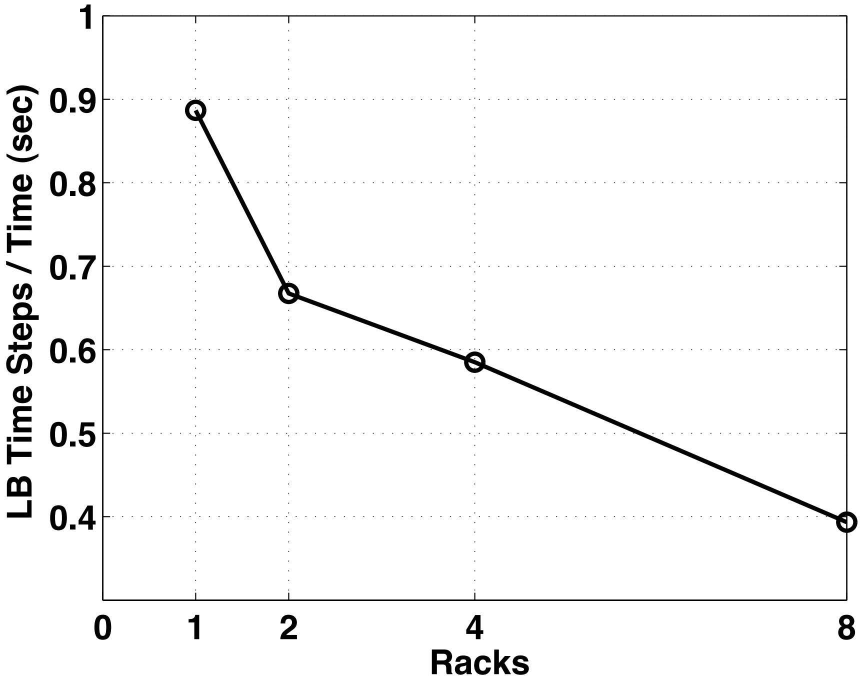

Figure 27: Weak scaling for multiphase simulations. LB time steps normalized by time to solution (s) for multi-phase wall bounded shear using *vn* mode. Figure from Clausen et al. (2010).

3.3 Discussion

The somewhat nontraditional combination of slow processor speed with fast network interconnect on the BGP architecture causes problems not seen on other clusters. First, the low memory headroom requires careful bookkeeping to ensure a linear growth in memory requirements during weak scaling. Second, the slow processor speed requires much smaller subdivisions than competing architectures, such as Intel-based clusters. For single-phase results, this perceived weakness is offset by the fast interconnect speed; however, the per-particle parallelism for the multiphase flow creates load-balancing issues. Compounding the issue, on BGP the computational time is dominated by the solid and boundary condition calculations. For comparison, with commodity Intel clusters using Core 2 processors, the computational time is roughly split evenly between fluid and solid (including boundary condition) calculations. One possible explanation is that the limited memory bus on the Core 2 architecture may become saturated with the memory-bandwidth intensive LB method, a result supported by the lack of scaling across 8 cores on a dual quad-core node. The particle update code is much less memory-bandwidth intensive, thus inflating the relative time spent computing fluid versus solid. The poor solid performance also hints at a section of the particle update code that remains serial. Whereas a single quad-core Intel workstation is able to simulate hundreds of particles at one LB time step per second, the BGP is only able to simulate tens of particles at same update frequency. To achieve adequate simulation speed, small subdomains are needed on the BGP, and the assumption of a roughly homogeneous distribution of particles begins to break down creating the aforementioned load-balancing problems.

Currently, this method is optimized for a rectangular Cartesian grid, thus a load-balancing issue will occur when simulating arbitrary geometries. For the case of tube flow, this loss in efficiency if fairly minor because the vessel still comprises the majority of the simulation volume. For more complicated geometries such as bifurcations, degradation in performance is expected. A scheme that attempts to balance the vessel volume between cores is desirable for these complex geometries.

Nevertheless, this adaptation of the LB/FE method is suitable for parallel computation on distributed-memory clusters. This method demonstrated an ability to scale on as many as 32,768 cores of the BGP system at ANL. Weak scaling results were adequate to perform simulations in excess of 100,000 particles; however, load balancing issues resulted in poor results for subdomain sizes below $32 \times 32 \times 32$, which constrains the maximum simulation lengths possible. Also, the performance of the disk I/O remains an open question that must be investigated further before undertaking these large-scale simulations. Future effort will also focus on ways to further subdivide the solid computational time in order to address this node balancing issue. As it stands, simulations of the size necessary for the data in this thesis are on the order of ∼64 cores, which is significantly less demanding than the scaling results reported in this chapter. A typical suspension simulation has been condensed from a several weeks into one to two days. Also, since the code is able to run on large computational clusters, many simulations can be run concurrently, which is important for the parametric sweep shown in Chapter 5. Resources available from TeraGrid include access to Steele, a 902 node 8-core Intel Xeon, and QueenBee, a 668 node 8-core Intel Xeon machine.

CHAPTER IV

DILUTE LIMIT EFFECTS

4.1 Capsule dynamics and rheology

The dynamics of deformable capsules, vesicles, and soft particles have been of continued interest to the scientific community. When immersed in flow, these particles exhibit much more complex dynamic behavior than rigid particles. In suspensions, these complex dynamics affect the rheology of the bulk flow, creating non-Newtonian flow characteristics, even in the dilute and semidilute regimes. Recent interest in biological flows, in which the particles are highly deformable, has spurred the increased study of capsules. For example, one of the most intensely studied deformable particles is the red blood cell because it is the major constituent of blood.

Before performing a detailed study of many-capsule suspensions, it is important to quantify the dilute-limit impact of deformation on the rheology, as detailed in Clausen & Aidun (2010). Specifically, the single-particle microstructure must be related to changes in the overall suspension rheology. When suspended in shear flow, initially spherical capsules deform into ellipsoidal shapes with a preferential orientation aligned with the extensional flow quadrant. The orientation remains steady, and the capsule's membrane "tank-treads" around the fixed ellipsoidal shape. For an isolated spherical capsule, the single-particle microstructure is quantified through two parameters: the Taylor deformation index and the orientation of the ellipsoid with the flow (x) direction. In contrast to earlier numerical work (for example Ramanujan & Pozrikidis, 1998; Eggleton & Popel, 1998), the complete normal stresses are resolved including the particle pressure.

4.2 Analytical recovery of particle pressure

Before discussing the numerical results, some analytical progress can be made for the case of an isolated capsule in shear by extending the results of Roscoe (1967) to include the isotropic particle pressure (Clausen & Aidun, 2010). The pressure disturbance terms are readily available in Jeffery's (1922) solution for a rigid ellipsoidal suspended in shear; however, these terms were neglected in the analysis by Roscoe (1967). Such neglect of the particle pressure can also be seen in studies for the rheology of slender bodies (Hinch & Leal, 1972, 1973). Note that the solution of Roscoe (1967), which was used by Keller & Skalak (1982) to study the transition from tank-treading to tumbling for nonspherical capsules, does not represent a closed-form solution for capsule dynamics, in contrast to the near-spherical perturbation studies (Barthès-Biesel, 1980; Misbah, 2006; Vlahovska & Gracia, 2007). It requires describing the particle microstructure *a priori*.

It is convenient to define some mapping between the notation used in Jeffery (1922) and this thesis and to define some important parameters. First, the constants defined by Jeffery (1922) in his equations (25) and (26) are expressed in this paper as

$$A_{ij} = \frac{8}{a^3} \begin{pmatrix} A & H & G' \\ H' & B & F \\ G & F' & C \end{pmatrix}, \tag{61}$$

which is similar to the notation found in Roscoe (1967). The undisturbed flow is assumed to be linear and is expressed as

$$v_i = E_{ij} r_j - \Omega_{ij} r_j, \tag{62}$$

where E_{ij} is the rate of strain tensor, Ω_{ij} is the vorticity tensor, and r_j is a position vector. The coefficients in A_{ij} are defined according to integrals which are dependent on the ellipsoidal geometry and the undisturbed flow. The principal axes of the ellipsoid are defined as $a\alpha_1 > a\alpha_2 > a\alpha_3$, in which the volume of the ellipsoid is equivalent to a sphere of radius a, and $\alpha_1\alpha_2\alpha_3 = 1$.

Thus,

$$A_{11} = \frac{4}{3}\frac{2g_1''E_{11}' - g_2''E_{22}' - g_3''E_{33}'}{g_2''g_3'' + g_3''g_1'' + g_1''g_2''}, \tag{63}$$

in which A_{22} and A_{33} can be obtained through cyclic permutations of the indices. Primed tensors, e.g. E_{ij}', refer to tensors in the coordinate system aligned with the ellipsoid's major axes. The integral g_1'' is defined according to

$$g_1'' = \int_0^\infty \frac{\lambda\, d\lambda}{(\alpha_2^2+\lambda)(\alpha_3^2+\lambda)\Delta'}, \tag{64}$$

where $\Delta' = \left[(\alpha_1^2+\lambda)(\alpha_2^2+\lambda)(\alpha_3^2+\lambda)\right]^{1/2}$. Integrals g_2'' and g_3'' can be obtained by permutation of indices in (64). Likewise, integrals g_1, g_2, and g_3 are defined of the type

$$g_1 = \int_0^\infty \frac{d\lambda}{(\alpha_1^2+\lambda)\Delta'}. \tag{65}$$

Jeffery's solution for surface forces on the surface of an ellipsoid, which is valid in any coordinate system, is given as

$$T_i = -\left(p_o + \frac{1}{2}\mu\sum_{\alpha=1}^{3} g_\alpha A_{\alpha\alpha}\right) n_i + \mu A_{ij} n_j, \tag{66}$$

where p_o is the far-field pressure, and the term involving $\sum g_\alpha A_{\alpha\alpha}$ is typically neglected as an isotropic contribution of no importance. Also note that A_{ij} is indeed traceless, which is verifiable using (63). By substituting (66) into the definition of the particle stresslet (6) and applying divergence theorems, the particle stress in the aligned coordinate system can be described as

$$\Sigma_{ij}'^{(p)} = \int_V \left\{-\Pi_p\delta_{ij} + \mu A_{ij}\right\} dV - 2\mu\bar{E}_{ij}'^{(p)}, \tag{67}$$

where $\bar{E}_{ij}'^{(p)}$ is the mean strain rate of the particle, and the particle pressure is recovered as

$$\Pi_p \equiv \frac{1}{2}\mu\sum_{\alpha=1}^{3} g_\alpha A_{\alpha\alpha}. \tag{68}$$

The mean pressure is dictated by the arbitrary far-field pressure term p_0, which has been dropped from (68). Thus, Π_p represents the difference in pressure between the particle and fluid phases, such that the average pressure in both solid and fluid phases is equivalent when $\Pi_p = 0$.

Up to this point, these results are valid for rigid torque-free ellipsoids suspended in arbitrary linear flow fields. By taking advantage of the linearity of the Stokes flow equation, the velocity disturbance of a tank-treading ellipsoid in a linear field (62) can be equated to that of a rigid ellipsoid in a velocity field in which the far-field disturbance accounts for the tank-treading behavior (Roscoe, 1967). Note that Π_p is sensitive to the particle orientation (θ) due to the dependence of $A_{\alpha\alpha}$ on the ellipsoid-aligned strain-rate tensor. Thus, the particle pressure can be determined using (68) with one caveat: the application of Jeffery's solution requires a linear flow field; therefore, the deformation must be homogeneous, i.e., the velocity everywhere inside the particle is described as

$$v_i^{(p)} = \bar{E}_{ij}^{(p)} r_j - \bar{\Omega}_{ij}^{(p)} r_j, \tag{69}$$

where $\bar{E}_{ij}^{(p)}$ and $\bar{\Omega}_{ij}^{(p)}$ are constant. This assumption violates conservation of local surface area, and material points on the particle's surface travel with varying velocity magnitudes. A closed-form solution for the capsule dynamics is not possible without considering the particle material, which is calculated for simple viscoelastic solids in (Roscoe, 1967).

Some comments on the behavior of the particle pressure: In the limit of a sphere, $g_1 = g_2 = g_3$, and the particle pressure vanishes because $A_{ii} = 0$. For a fixed shape, if the particle aligns with the flow ($\theta = 0$) or shear-gradient ($\theta = \pi/2$), the particle pressure vanishes, and a maximum pressure disturbance occurs at $\theta = \pi/4$.

4.3 Simulation results

Simulations are performed using an isolated spherical capsule suspended in simple shear. The elasticity of the capsule is characterized by the nondimensional capillary number (15). The finite thickness of the membrane does introduce a bending stiffness; however, its effect is minimal. The reduced ratio of bending to elastic modulus, which for an elastic shell element is defined as

$$E_b = \frac{t_m^2}{12a^2(1-\nu_p^2)}, \tag{70}$$

is 1.0×10^{-5} for all simulations. Simulations are performed in the Stokes flow limit, where the particle Reynolds number is small.

The domain is $160 \times 160 \times 160$, the undeformed particle radius is 10 lattice grid spacings, and the top and bottom wall velocities are ± 0.005 lattice grid spacings per time step, which gives $\mathrm{Re}_p = 0.0375$ and $\mathrm{Ma} = 0.009$. Simulation results include two different levels of discretization, one with 620 FE surfaces, and the other with 1222 FE surfaces. These meshes correspond to an average length between FE nodes, l_{FEA}, of 2.0 and 1.5 lattice spacings, respectively. Figure 28 shows the simulation setup for a single particle with $l_{FEA} = 1.5$ and $G = 0.03$.

The microstructure is quantified by the orientation angle of the ellipsoid's major axis, θ, and the Taylor deformation parameter, $D_{xy} = (\alpha_1 - \alpha_3)/(\alpha_1 + \alpha_3)$, where $\alpha_1 a$ is the length of the major axis of the ellipse in the xy plane, and $\alpha_3 a$ is the length of the minor axis in the xy plane. Figure 28 illustrates the relevant quantities used in determining the microstructure. Calculating D_{xy} and θ using a naive algorithm based on the maximum and minimum distance to any FE node results in large errors due to the relative coarseness of the FE mesh; consequently, the microstructural parameters are obtained by finding an ellipsoidal body with an equivalent moment of inertia, as originally proposed by Ramanujan & Pozrikidis (1998). For convenience, the volume integral for calculating the moment of inertia of the FE body can be converted into

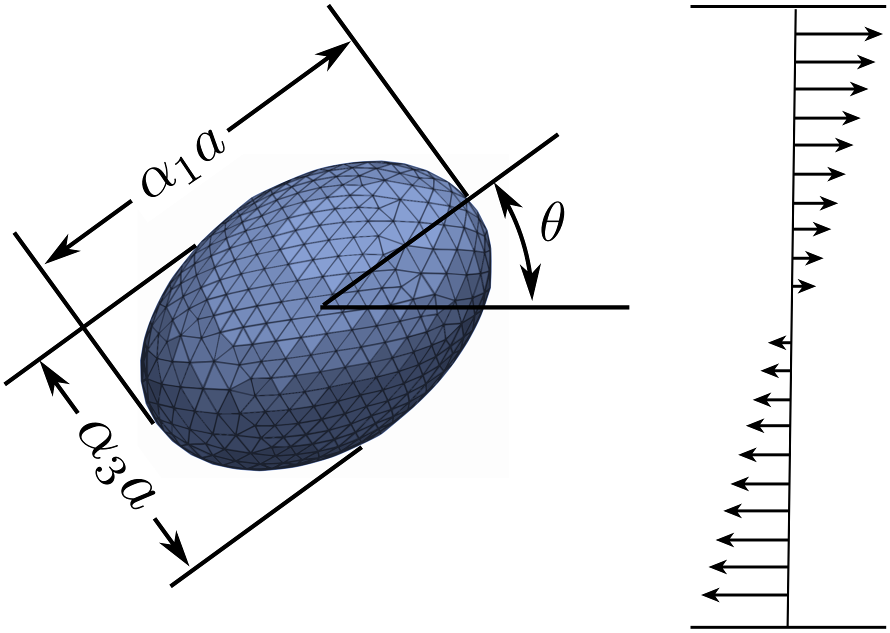

Figure 28: Simulation setup for an isolated capsule in shear. Capsule shown has 1222 elements, corresponding to an averaged element edge length of 1.5 lattice grid spacings.

a surface integral, shown using summation notation as

$$I_{ij}^{inertia} = \int_V r_k r_k \delta_{ij} - r_i r_k \, dV = \frac{1}{5} \int_A r_l r_l r_k n_k \delta_{ij} - r_i r_j r_k n_k \, dA. \tag{71}$$

Note the order of operations reported in Ramanujan & Pozrikidis (1998) is incorrect. The principal axes of of the matrix $I_{ij}^{inertia}$ coincide with the axes of the ellipsoid, which has an analytically known moment of inertia. The eigenvalue problem is solved using LAPACK, a standard math package for scientific programming.

4.3.1 Microstructure results

Figure 29(a) shows the transient behavior of the Taylor deformation parameter, and Figure 29(b) shows the transient behavior of the orientation angle. Several levels of deformation are shown, with both levels of discretization yielding an accurate description, except for the orientation at low Ca_G. At low Ca_G, the particle remains nearly spherical, and oscillations occur in the moment of inertia calculation. This error is significantly reduced by the finer mesh. To calculate converged values, a running average was taken after the initial transient.

Figure 30(a and b) show the converged long-time behavior for D_{xy} and θ, respectively, as a function of Ca_G. At low deformations, the deformation parameter agrees well with the first-order perturbation analysis of Barthès-Biesel (1980), but the second-order perturbation results are not shown for D_{xy} since they have a greater-than-linear growth and have worse agreement than the first-order analysis, which is a known limitation of the analysis. For the orientation angle, the first-order perturbation does not capture a deviation from $\theta = \pi/4$. Second-order results (Barthès-Biesel & Rallison, 1981) do show a progressive alignment of the capsule with the flow direction ($\theta < \pi/4$), although the analytical results underpredict the alignment at relatively modest deformation ($\mathrm{Ca}_G > 0.06$), as seen in Figure 30b. Excellent agreement is seen between the LB/FE hybrid method and the numerical results of Ramanujan & Pozrikidis (1998) at all but the highest Ca_G, which validates using a linear FE membrane. Ramanujan & Pozrikidis (1998) use a nonlinear Neo-Hookean membrane without bending stiffness. Not shown, similar agreement for the Taylor deformation parameter is seen in the numerical results of Eggleton & Popel (1998).

Comparison of the simulation results to the analytical work of vesicles (Seifert, 1999; Misbah, 2006; Vlahovska & Gracia, 2007) in the small-deformation limit is possible; however, D_{xy} is no longer a free parameter. For vesicles, the deformation is quantified by the excess area, which is a fixed quantity owing to the membrane's strict area conservation. This excess area is readily calculated in the LB/FE simulations, and is a steady quantity for a tank-treading capsule. The results for vesicle theory using the microstructure parameters determined by simulation are shown in Figure 30, and good agreement is seen. The inclination angle is a function of the ellipsoidal shape, which is prescribed for the vesicle theory. It is important to stress

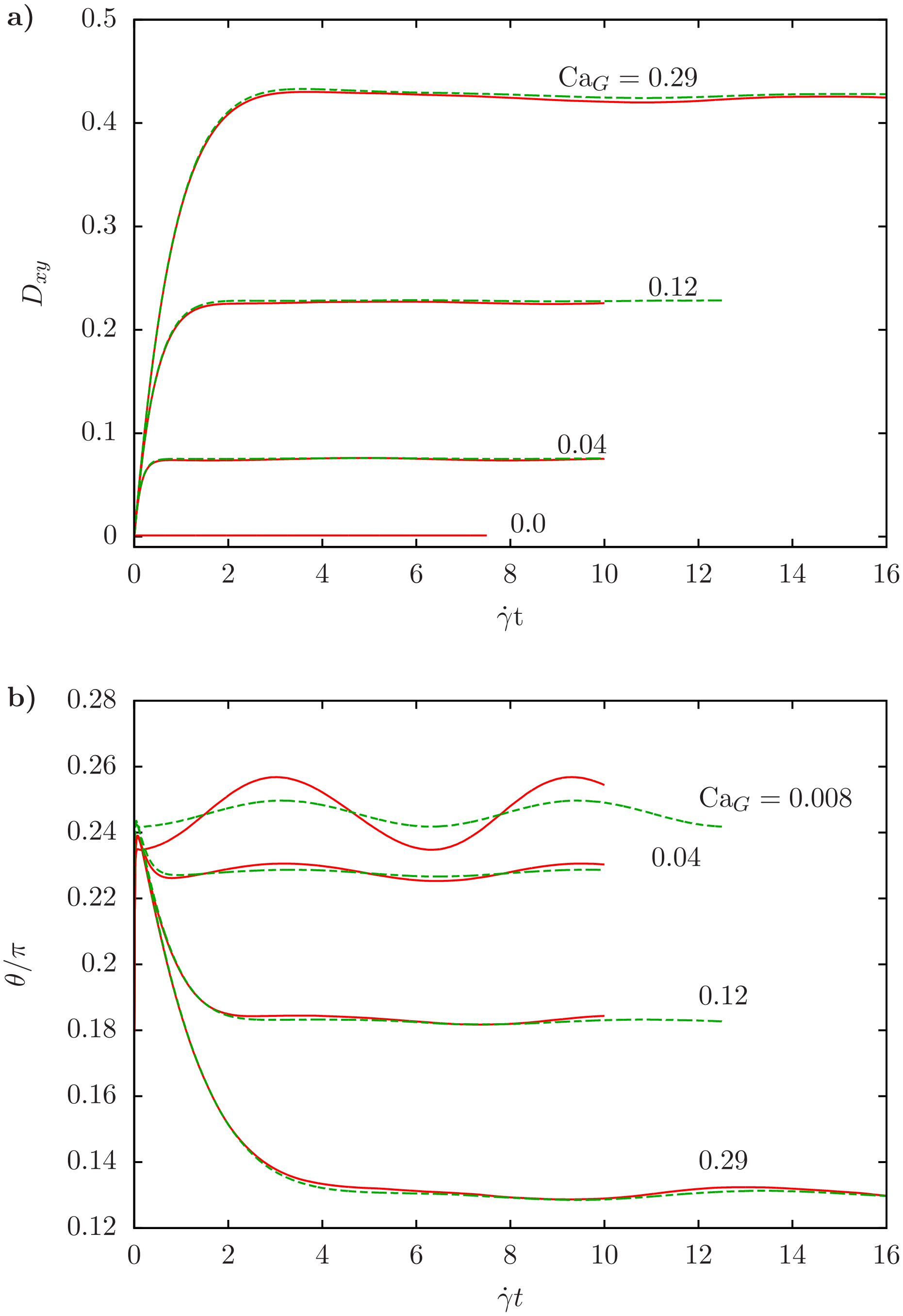

Figure 29: Transient Behavior of the (a) Taylor deformation parameter and (b) orientation angle for an isolated spherical capsule in shear. Solid and dashed lines correspond to $l_{FEA} = 2.0$ and $l_{FEA} = 1.5$, respectively. Figure data from Clausen & Aidun (2010).

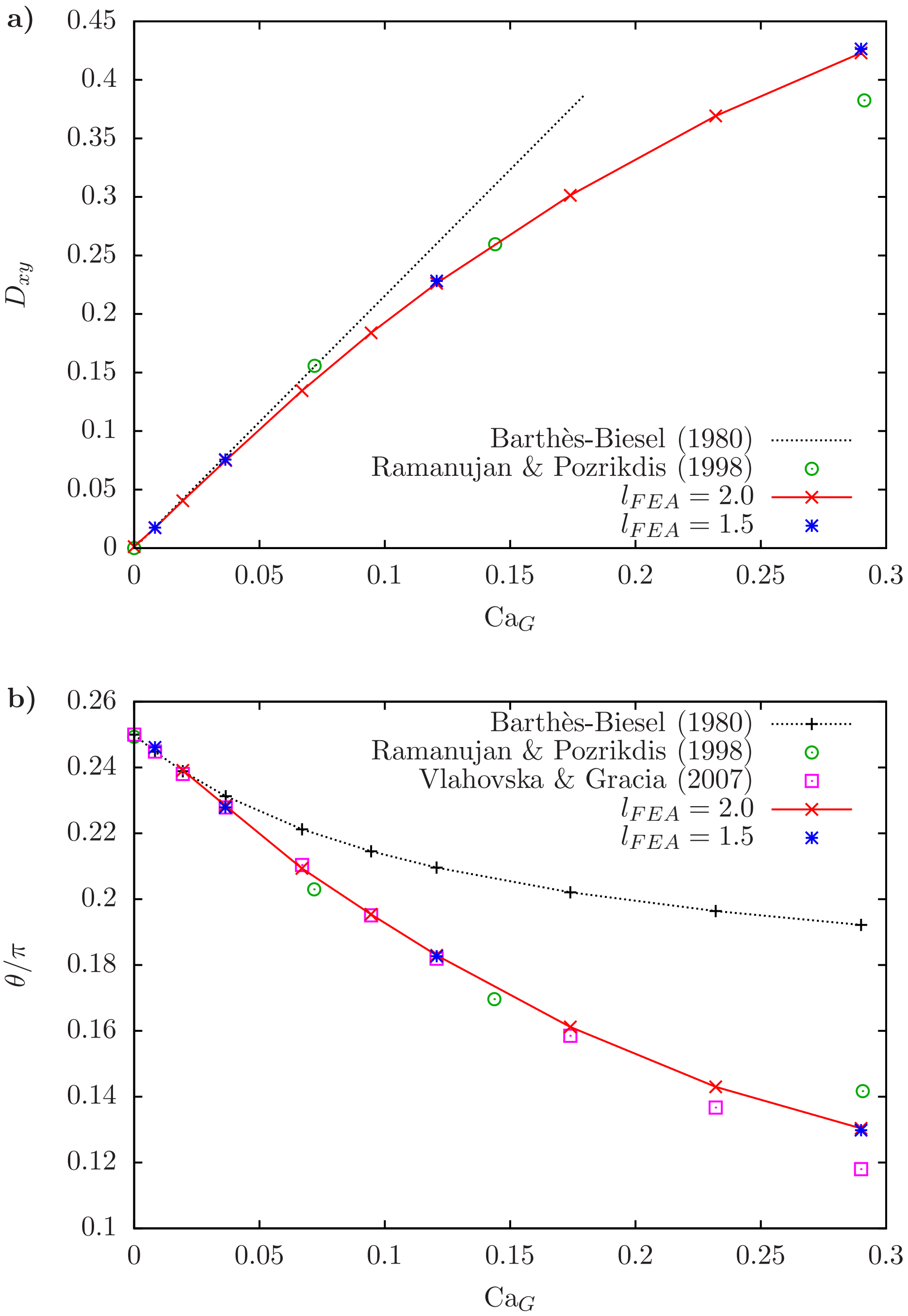

Figure 30: Time-averaged results for the (a) Taylor deformation parameter and (b) orientation angle for an isolated spherical capsule. Figure data from Clausen & Aidun (2010).

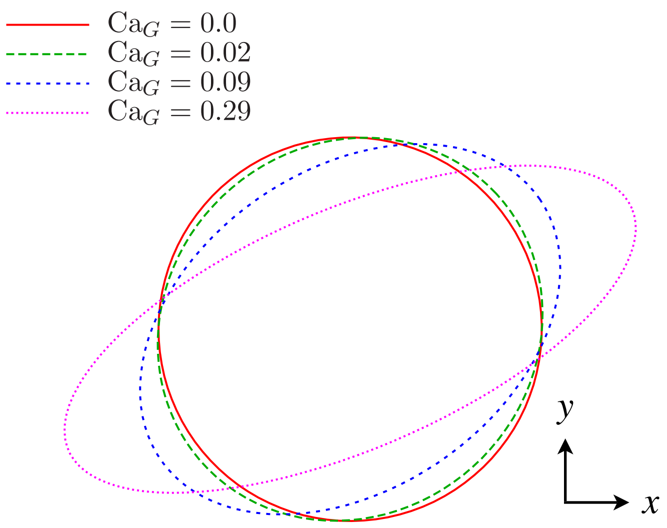

Figure 31: The outline of the particle as a function of of Ca_G. As Ca_G increases, the particle deformation increases, and the particle aligns with the flow (x) direction.

that using vesicle theory does not represent a closed form solution for capsule dynamics because in capsule simulations, the deformation is a dependent variable. However, since matching the vesicle microstructure to a given capsule simulation is possible, a comparison can be made between the LB/FE rheology results and those of vesicle theory (Vlahovska & Gracia, 2007).

Figure 31 shows the particle outline for model ellipses with D_{xy} and θ equivalent to the simulation results. Again, notice the progressive alignment of the capsules with the flow direction (x) as the deformation increases.

4.3.2 Rheology

The effect of the capsule on rheology is ascertained through the calculation of the particle stresslet (6), which includes the isotropic particle pressure term. In all rheology plots, the results have been normalized by $\Sigma_{12}^{(p),s}$, the shear component of the particle stress for an isolated sphere. Normalized results are denoted by starred quantities. Suspensions of deformable capsules are weakly shear thinning, a result which can be seen in Figure 32(a and b) for the transient and time-averaged results, respectively. Linear perturbation results for capsules do not demonstrate shear thinning (Barthès-Biesel, 1980). Analysis of vesicles does demonstrate shear thinning behavior (Vlahovska & Gracia, 2007), and for low deformation ($\mathrm{Ca}_G < 0.06$), the vesicle theory agrees well with numerical results; however, it greatly overpredicts shear thinning at higher deformations.

Likewise, the theory of Roscoe (1967), shown in Figure 32(b), in which the simulation microstructure results are used to prescribe the particle's shape and orientation, overpredicts the shear thinning behavior, or stated another way, energy dissipation is underpredicted. This underprediction is a direct result of the assumption of homogeneous deformation tensor inside the particle. For a capsule undergoing the same average rate of strain as a homogeneously deforming solid particle (69), the capsule introduces a local disturbance to the rate of strain, $\hat{\mathbf{E}}^{(p)}$, such that $\mathbf{E}^{(p)} = \bar{\mathbf{E}}^{(p)} + \hat{\mathbf{E}}^{(p)}$, where $\hat{\mathbf{E}}^{(p)}$ has a zero average over the entire particle and thus no effect on the mean rate of strain. Considering that the mean dissipation internal to the capsule, Φ, can be represented as

$$\Phi = \int_V 2\mu \mathbf{E}^{(p)} : \mathbf{E}^{(p)} dV, \tag{72}$$

it is easy to see that the case of homogeneous deformation, i.e., $\hat{\mathbf{E}}^{(p)} \equiv 0$, represents a minimum in energy dissipation.

Figures 33(a and b) show the transient behavior of the first and second normal stress differences. For the highly deformable case, the particle contribution to the first normal stress difference is on the same order as the shear stress contribution for an isolated sphere. The transient behavior of the normal stress differences, including the initial overshoot of the second normal stress difference, compare well with transient results from Ramanujan & Pozrikidis (1998). Small oscillations are evident in the second normal stress difference due to its small magnitude. The transient particle pressure is shown in Figure 34 and is negative for all values of Ca_G. As with the

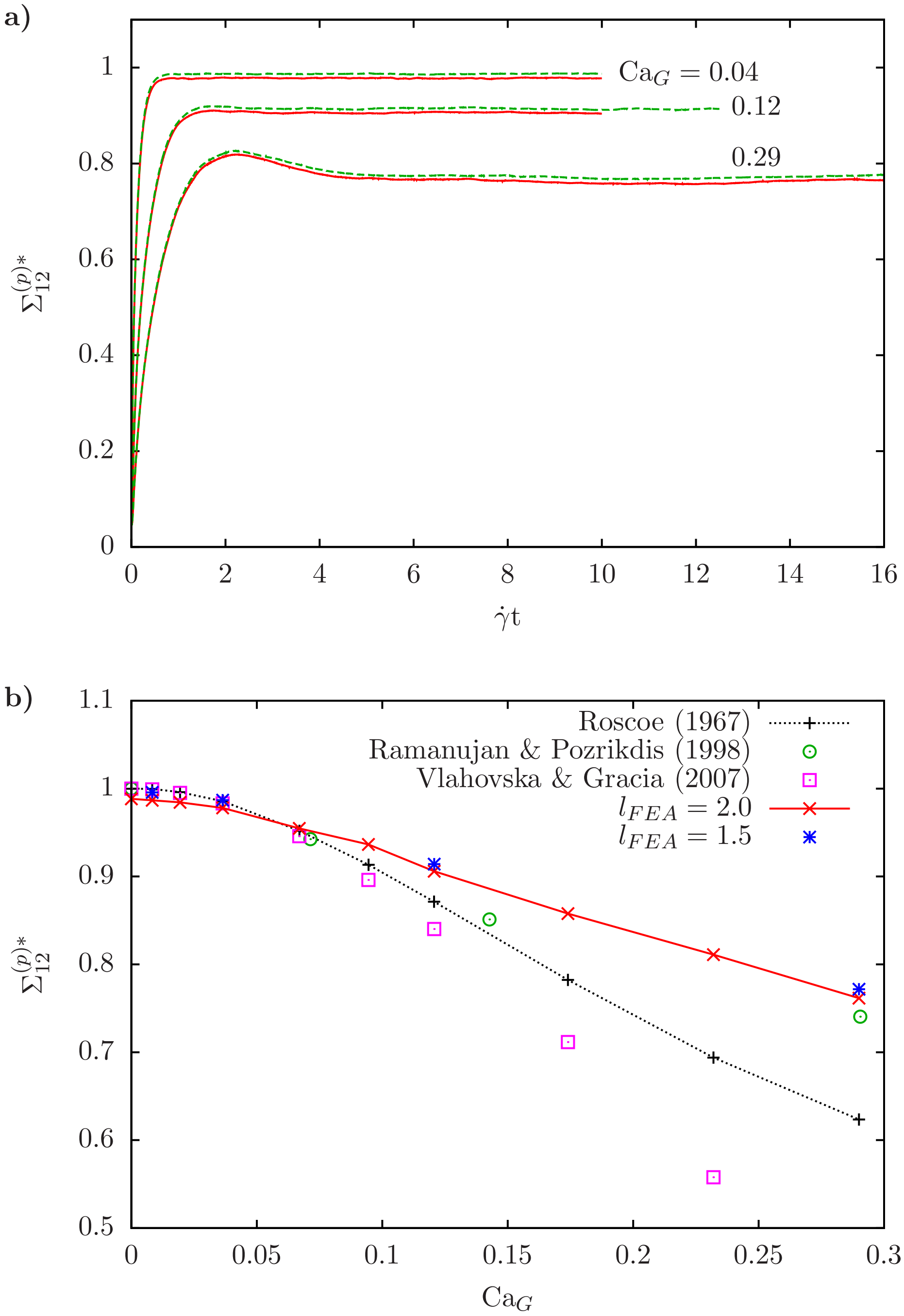

Figure 32: The shear component of the particle stress for an isolated capsule in shear; (a) the transient results, where solid and dashed lines correspond to $l_{FEA} = 2.0$ and $l_{FEA} = 1.5$, respectively; (b) the time-averaged behavior. Figure data from Clausen & Aidun (2010).

microstructure, rheological parameters are generally insensitive to the resolution of the finite element mesh. We do note a slight underprediction of $\Sigma_{12}^{(p)*}$ for the coarse particle that may be caused by the slightly lower volume enclosed by the coarse mesh.

The long-time average values for the typical rheological values of N_1^* and N_2^*, as well as Π_p, are shown in a Figure 35(a–c). Also shown are the numerical results of Ramanujan & Pozrikidis (1998), vesicle theory (Vlahovska & Gracia, 2007), and the viscoelastic solid theory of (Roscoe, 1967), which is extended to resolve Π_p^*. The simulation results agree well with the numerical work of Ramanujan & Pozrikidis (1998), although no particle pressure results are available with other numerical results. Vesicle theory remains accurate for N_1^* up to surprisingly large Ca_G considering the poor prediction of viscosity; however, results for N_2^* are much poorer. The theory of Roscoe (1967) systematically overpredicts N_1^* while underpredicting N_2^*. These errors are a consequence of underpredicting the dissipation internal to the particle. The components of the particle stress, $\boldsymbol{\Sigma}^{(p)}$, in the aligned (primed) coordinates are related to the nonaligned coordinates by

$$\left.\begin{aligned} \Sigma_{11}^{(p)} &= \Sigma_{11}^{'(p)} \cos^2\theta + \Sigma_{22}^{'(p)} \sin^2\theta - \Sigma_{12}^{'(p)} \sin 2\theta \\ \Sigma_{22}^{(p)} &= \Sigma_{11}^{'(p)} \sin^2\theta + \Sigma_{22}^{'(p)} \cos^2\theta + \Sigma_{12}^{'(p)} \sin 2\theta \\ \Sigma_{33}^{(p)} &= \Sigma_{33}^{'(p)} \end{aligned}\right\} . \tag{73}$$

Thus, the underprediction of $\Sigma_{12}^{'(p)}$ in Roscoe's theory translates into the normal stress errors seen in Figure 35. It is also obvious that the errors cancel in determining the isotopic portion of the stress inside the particle, which explains the excellent agreement in Figure 35(c).

Figure 36 shows the individual normal stress components. Again, the inadequate shear component in Roscoe's results causes errors in the prediction of $\Sigma_{11}^{(p)}$ and $\Sigma_{22}^{(p)}$, while the prediction of $\Sigma_{33}^{(p)}$ remains accurate.

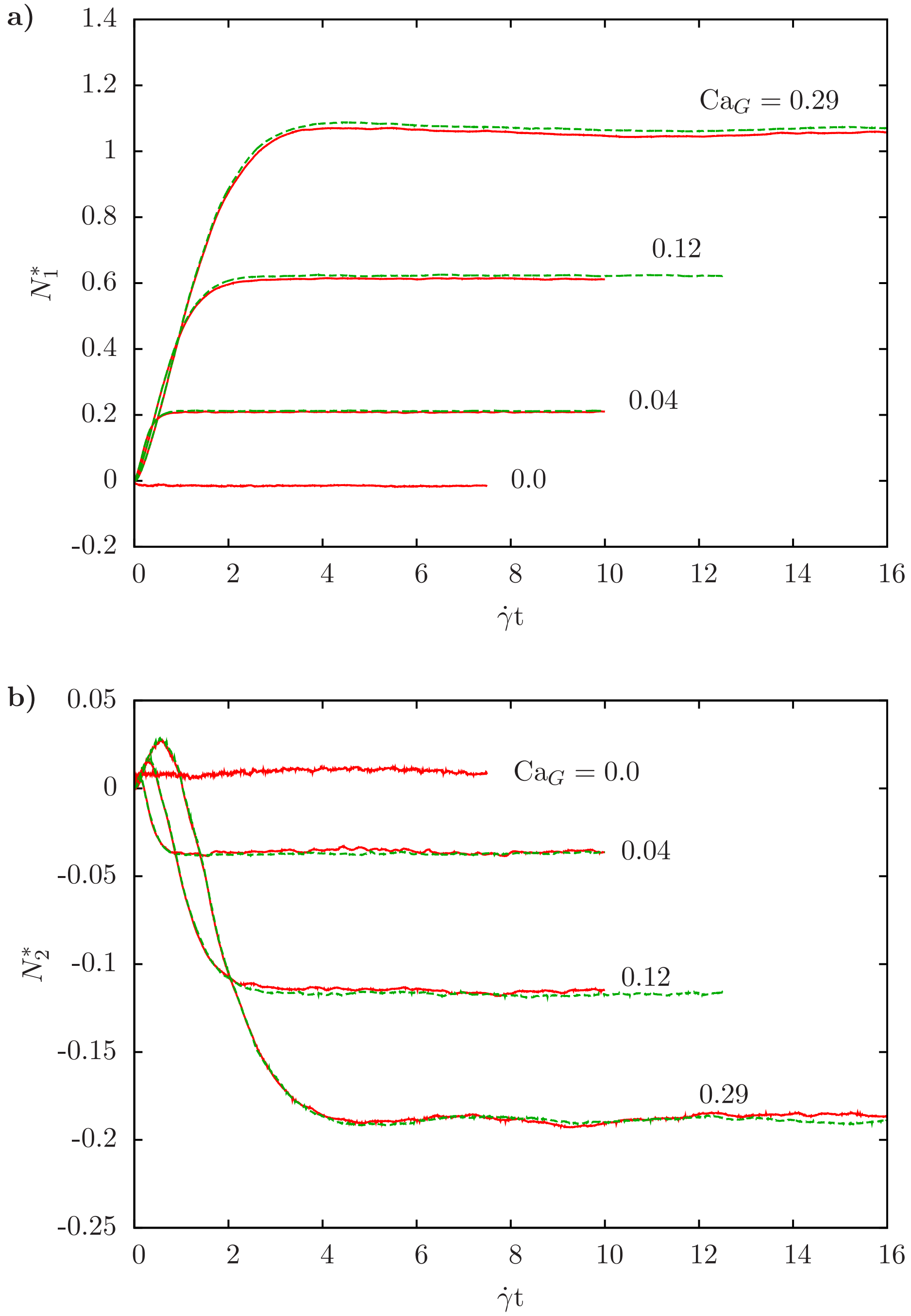

Figure 33: Transient behavior of the (a) first and (b) second normal stress differences for an isolated capsule in shear. Solid and dashed lines correspond to $l_{FEA} = 2.0$ and $l_{FEA} = 1.5$, respectively. Figure data from Clausen & Aidun (2010).

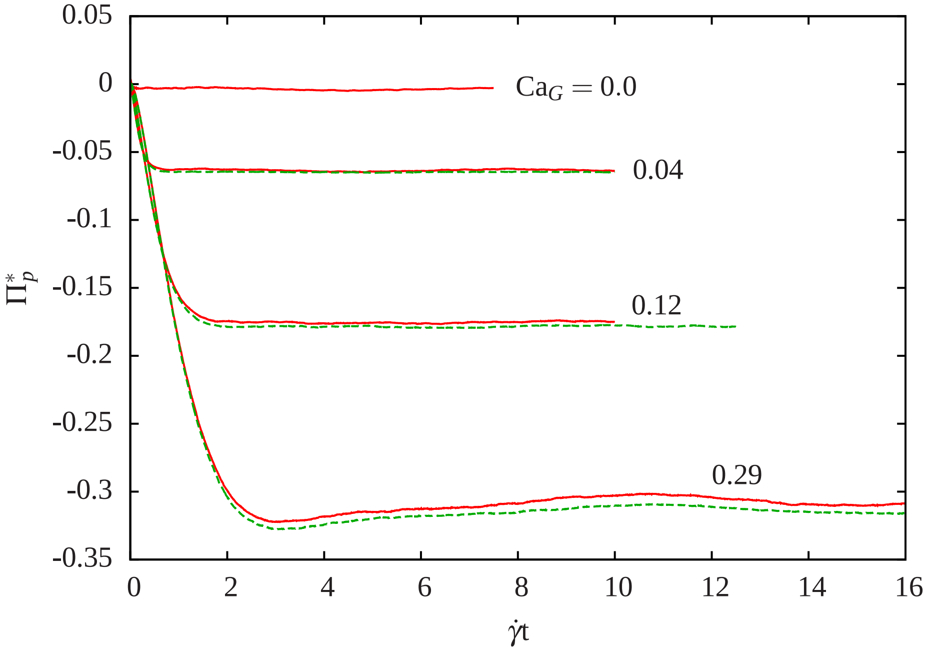

Figure 34: Transient behavior of the particle pressure for an isolated capsule in shear. Solid and dashed lines correspond to $l_{FEA} = 2.0$ and $l_{FEA} = 1.5$, respectively. Figure data from Clausen & Aidun (2010).

4.4 Discussion

The dilute-limit microstructure and its impact on the dilute-limit rheology in capsule suspensions is thoroughly investigated in this chapter, and the results were compared with analytical and numerical results in literature. Some of the existing numerical results use much finer membrane meshes and nonlinear membrane models, yet the LB/FE results achieved excellent agreement at lower deformations ($\mathrm{Ca}_G < 0.3$). These results firmly validate the LB/FE method as capable of obtaining realistic dynamics of capsules in shear undergoing tank-treading behavior.

The dilute-limit rheology of these capsule suspensions is described as a function of the capsule microstructure (D_{xy} and θ). In addition to normal stress differences, the particle pressure is calculated, thus correctly resolving the individual normal stresses in a dilute suspension of capsules. In contrast to spherical particles, capsules create normal stress differences and affect the particle pressure in the dilute limit.

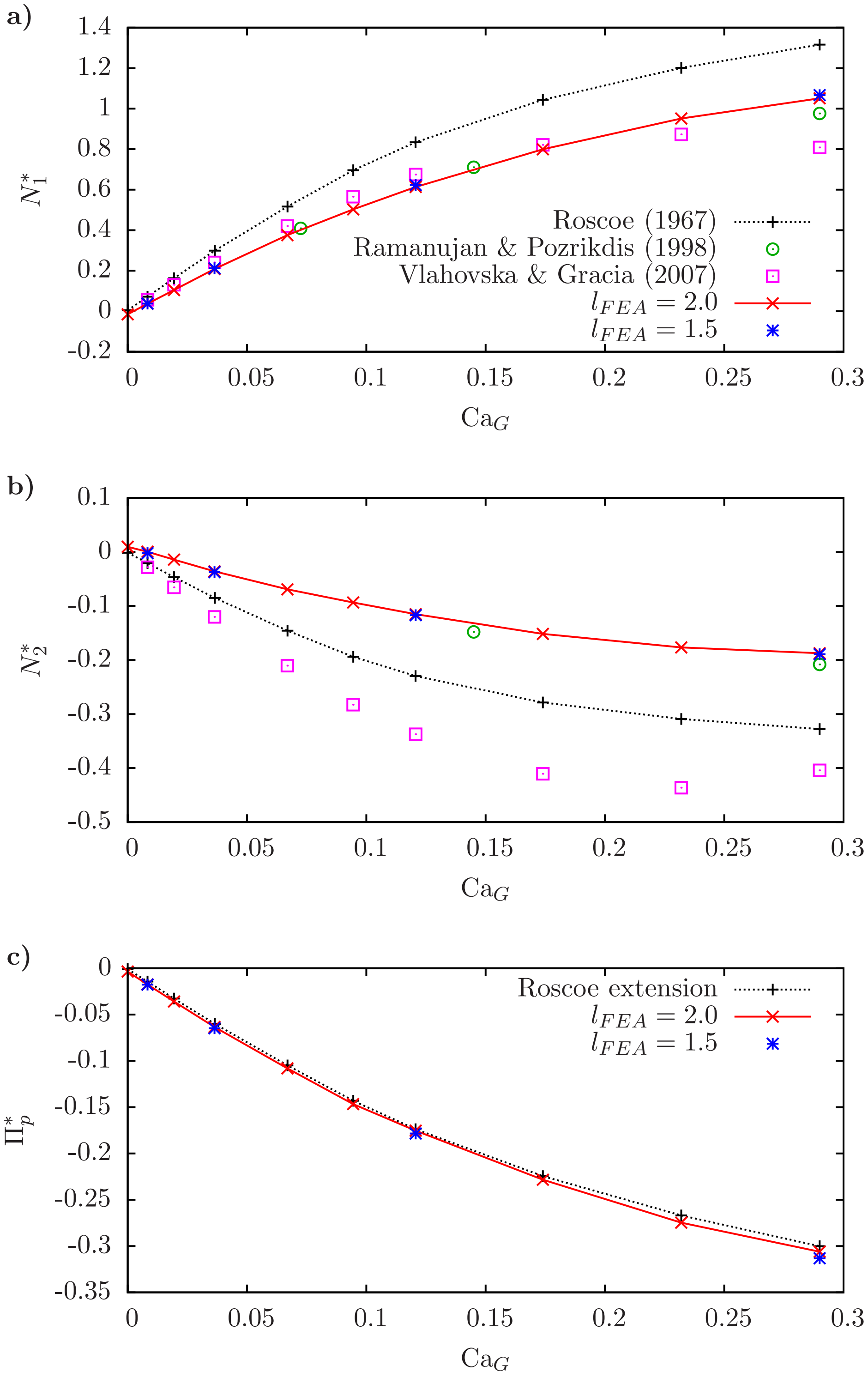

Figure 35: Long-time behavior of the capsule rheology showing (a) N_1^*, (a) N_2^*, and (c) Π_p^*. The legend is the same for (a) and (b). Figure data from Clausen & Aidun (2010).

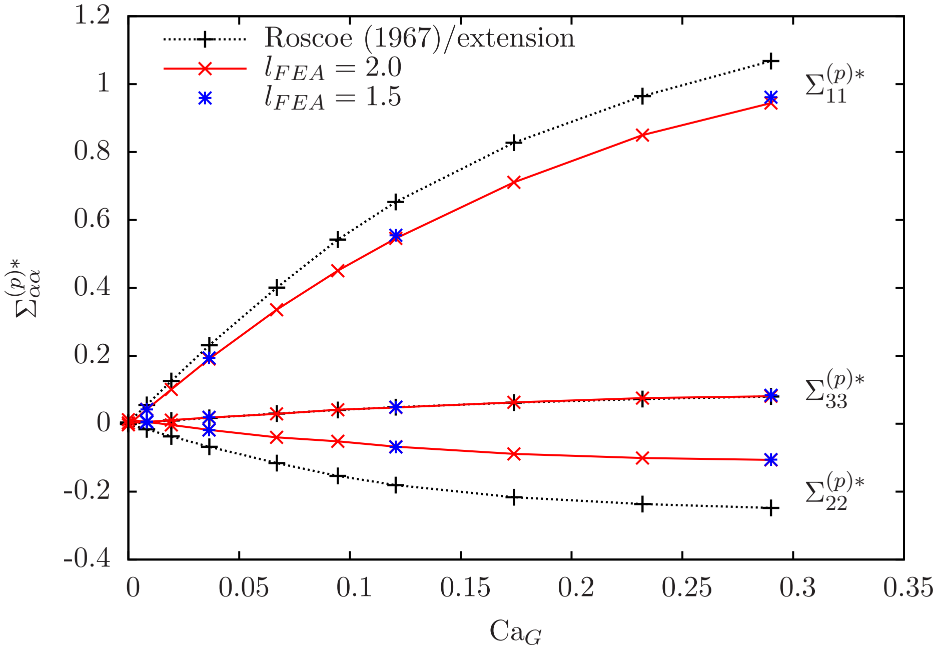

Figure 36: Individual normal stress components for an isolated capsule. Figure data from Clausen & Aidun (2010).

Comparisons of capsule rheology are made with several analytical models, and an extension to the results of Roscoe (1967) allows the prediction of a negative particle pressure. Excellent agreement between the analytical model and the numerical results are seen for the particle pressure term; however, errors in the dissipation internal to the particle caused inaccuracies in the normal stresses in the flow and shear-gradient directions. As discussed in chapter 1, correctly describing the normal stresses in capsule suspensions has a practical significance in understanding particle migration.

CHAPTER V

SUSPENSION RHEOLOGY

5.1 Dense capsule suspensions

The previous chapter characterized the rheology of isolated non-Brownian capsules and found that significant non-Newtonian effects can be generated by the single-body microstructure. The initially spherical capsules deform into ellipsoidal particles with a preferential orientation. Now that the behavior of dilute suspensions is well characterized, this chapter will study the microstructure and rheology of higher concentration suspensions. As discussed in chapter 1, in the dilute-limit, suspensions of rigid noncolloidal spherical particles are Newtonian, i.e., in shear, the only nonzero components to the suspensions stress are the Σ_{12} and Σ_{21} components. These components augment the effective viscosity of the suspension, but do not generate normal stress differences. In dense suspensions, however, anisotropy in the overall particle configuration spurs the generation of a negative first normal stress (Sierou & Brady, 2002). This behavior contrasts with that expected via a dilute-limit analysis of capsule behavior, in which a large positive first normal stress difference is seen. The normal stresses generated from the microstructure of an individual capsule seem to be in competition with the stresses generated from the overall configuration of particles. This chapter will explore these effects and provide insight into dense capsule suspensions.

5.2 Sensitivity to parameters

Before discussing suspension results in detail, it is important to quantify the sensitivity of the simulation results to several parameters that are potential sources of error. Parameters investigated include the number of particles, particle discretization, particle Reynolds number, and contact forces. To a large extent, the appropriate parameters have been described in chapter 2 through smaller model problems, but this section shows their impact on suspension rheology as a whole.

5.2.1 Number of particles and simulation repeatability

The rheology and microstructure measurements are average quantities, and as such, a large enough number of particles is required to achieve converged statistics. In dense suspensions, these parameters can show large fluctuations, and achieving reliable estimates of these quantities requires a significant number of particles simulated for large times (> 30 strain units).

Test simulations are performed in unbounded shear with a moderate level of deformation ($\mathrm{Ca}_G = 0.02$) at 40% volume fraction, although some small variance in volume fraction exists due to the integer nature of the number of particles and the domain size. In all cases, the particle radius is 10 lattice spacings, the discretization is such that $l_{FEA} = 2.0$ and $\mathrm{Re}_p = 0.067$. Simulations are performed at $N = 25$, 50, 97, and 285, with all simulations using the Lees–Edwards boundary condition. Contact parameters are chosen such that $\tilde{A}_c = 1.27$, $\tilde{\sigma}_c = 0.0075$, and $\tilde{g}_c = 0.05$. Contact parameters will be investigated in detail in section 5.2.3. Figure 37 shows a snapshot of a typical capsule simulation with $N = 285$ and $\mathrm{Ca}_G = 0.02$.

Ensemble-averaged quantities are approximated by plotting transient values for the rheology and microstructure that have been averaged over all particles in the domain. Then, after the initial transient (usually ~10 strain units), a time average is calculated from that point onwards. Figures 38(a–c) show the transient behavior of the deformation index, relative viscosity, and first normal stress difference for several N as thin lines. Time-averaged quantities are denoted by heavy lines, with time-averaging starting at $\dot{\gamma}t = 10$. The Taylor deformation parameter and relative

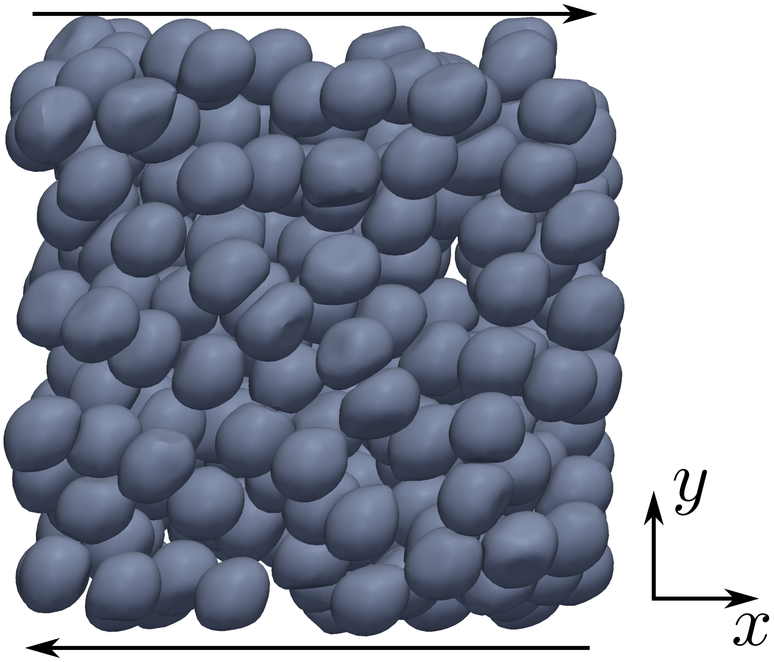

Figure 37: Snapshot of typical simulation of 285 initially spherical capsules with $\mathrm{Ca}_G = 0.02$.

suspension viscosity are generally insensitive to changes in N, although the low particle cases do display larger fluctuations, as seen in the instantaneous values. The first normal stress differences show especially large fluctuations in the instantaneous particle-averaged results, with the $N = 25$ and 50 cases showing poor time-averaged convergence.

The rheological and microstructural parameters show better convergence the longer the time averaging continues, with reasonable convergence seen around 40 strain units, i.e., 30 strain units after the initial transient. The full range of rheological parameters for all N is shown in Table 4, with values containing the time average from 10–40 strain units. For the case of $N = 285$, a simulation of 130 strain units is performed to allow averaging over independent 30 strain unit periods (10–40, 40–70, etc.), and the value ranges found in Table 4 represent the mean and a range of two standard deviations. The expected uncertainty would be much larger for the lower N cases, and a rigorous statistical test determining if N is significant is not possible without

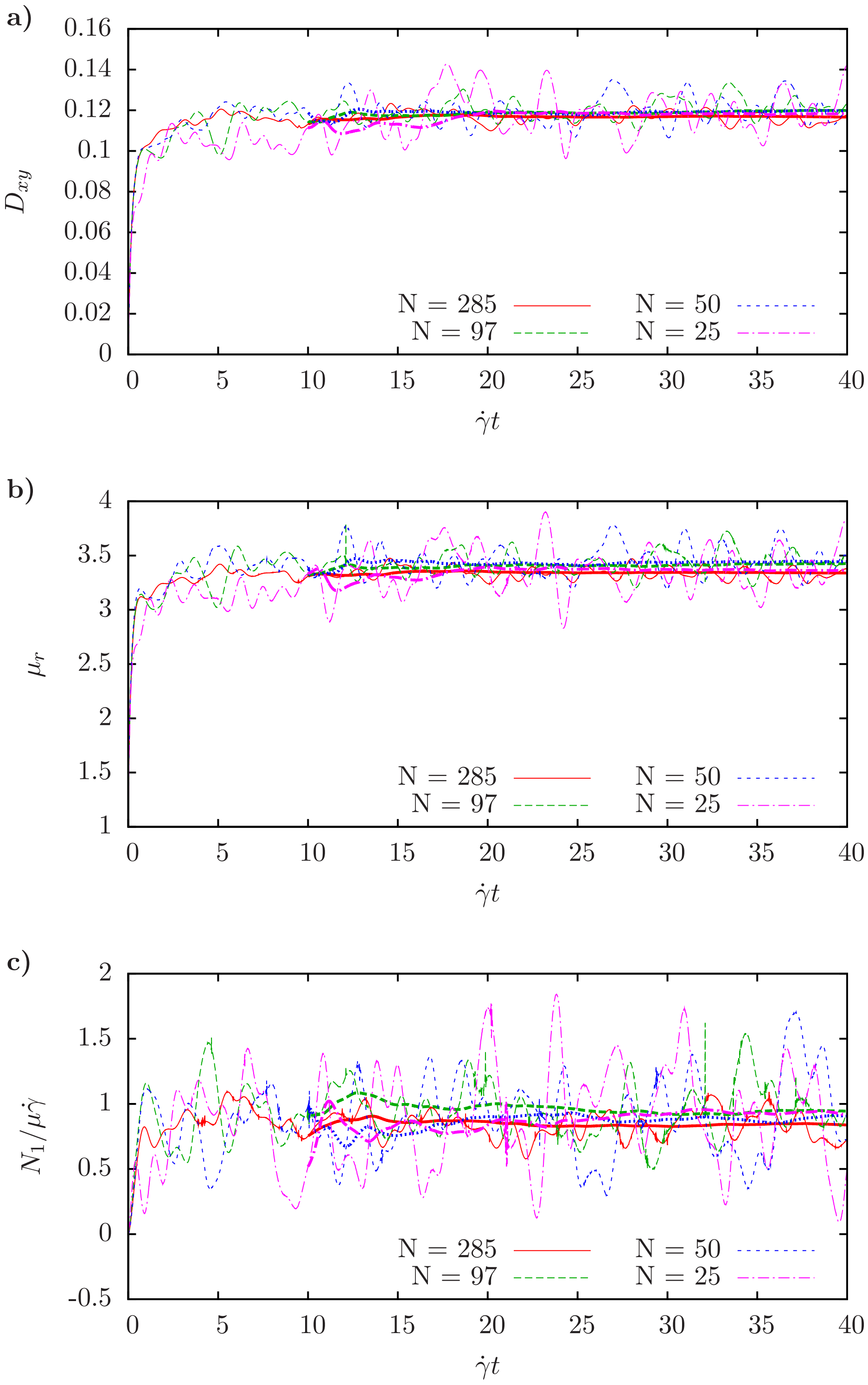

Figure 38: Transient behavior for simulations of a varying number of particles, N. Results show the (a) deformation index, (b) relative suspension viscosity, and (c) first normal stress difference. Thin lines show transient behaviors, while thick lines show time-averaged values starting at $\dot{\gamma} = 10$.

Table 4: Converged microstructure and rheology parameters for $\mathrm{Ca}_G = 0.02$ simulation as a function of the number of particles, N. Range at $N = 285$ represents 2 standard deviations calculated by 4 separate time averages.

N	**25**	**50**	**97**	**285**
Domain	64^3	80^3	100^3	144^3
$\boldsymbol{\phi}$	39.20	40.14	39.87	39.23
$\boldsymbol{D_{xy}}$	0.1186	0.1197	0.1200	0.1173 ± 0.0004
$\boldsymbol{\theta/\pi}$	0.2161	0.2176	0.2165	0.2191 ± 0.0004
$\boldsymbol{\mu_r}$	3.370	3.444	3.426	3.342 ± 0.0032
$\boldsymbol{N_1/\mu\dot{\gamma}}$	0.9157	0.9060	0.9448	0.8322 ± 0.0108
$\boldsymbol{N_2/\mu\dot{\gamma}}$	-0.3505	-0.3413	-0.3949	-0.3771 ± 0.0070
$\boldsymbol{\Pi_p/\mu\dot{\gamma}}$	0.2838	0.2939	0.2795	0.2711 ± 0.0120

long simulations at all N. Nevertheless, the repeatability is excellent at $N = 285$.

The converged microstructure and rheology averages show only minor differences as a function of N, and these differences may be readily attributed to the poor accuracy of the low N simulations. Owing to the smaller fluctuations in averaged quantities and higher accuracy, the parametric study in section 5.3 will use 285 particles for the 40% concentration cases. Details on dense suspension simulations can be found in section 5.3.

5.2.2 Reynolds number and particle discretization

The primary interest of this study is in the limit of low-Reynolds-number (Stokes) flows; however, the LB method properly recovers inertial behavior, thus a small amount of inertia will be present. Furthermore, reducing Re_p requires decreasing the shear rate, which increases the number of time steps necessary to reach a given nondimensional time. Increasing the fluid viscosity is possible, but without higher-order bounce-back schemes (Aidun & Clausen, 2010), this results in increased error in the bounce-back boundary condition (Noble et al., 1995; Ladd & Verberg, 2001; Ding & Aidun, 2003), thus the preferred viscosity is 1/6. To demonstrate the effect of inertia, the 40% volume fraction case with 285 particles from the previous section is simulated at $\mathrm{Re}_p = 0.0067$, 0.067, and 0.67, and the transient and time-averaged behavior of D_{xy}, μ_r, and N_1 is shown in Figures 39(a–c). All simulations use $l_{FEA} = 2.0$ except where noted. The high-Re_p case shows a noticeable drift in the rheology and microstructure results, although the error is relatively small ($\sim$10% for the first normal stress difference) when compared with the baseline ($\mathrm{Re}_p = 0.067$) case. The small-magnitude Re_p simulation exceeds the current computational capabilities; however, the short-time behavior shows excellent agreement with the baseline $\mathrm{Re}_p = 0.067$ case, as seen in the zoomed insets in Figures 39. Furthermore, the error in the high-Re_p case is evident even in the initial transient, suggesting that the Reynolds number effects are negligible at $\mathrm{Re}_p = 0.067$. The difference between the fine discretization ($l_{FEA} = 1.5$) case and the baseline is minimal. Other microstructure and rheology results not shown in Figures 39(a–c) show similar behavior.

The model problems in chapter 2, the dilute limit results in chapter 4, and the simulations shown in Figures 39 show that capsules with a discretization level of $l_{FEA} \leq 2.0$ are sufficient to accurately capture particle dynamics and suspension rheology. Also, these results suggest that $\mathrm{Re}_p = 0.067$ is an appropriate Reynolds number for the accurately capturing the suspension microstructure and rheology in the Stokes-flow limit.

5.2.3 Contact forces

In section 2.3.2, considerable effort is spent assessing the accuracy of the subgrid modeling for lubrication, with accurate results maintained down to 0.1 lattice units ($0.01a$). When dense suspensions are attempted with the proposed lubrication modeling, instabilities in the particle update procedure are seen and manifest as fluctuations in the capsule membrane. These instabilities are hard to predict, and are a byproduct of the singular nature of lubrication hydrodynamics, as well as the discrete and fluctuating nature of the link-based method.

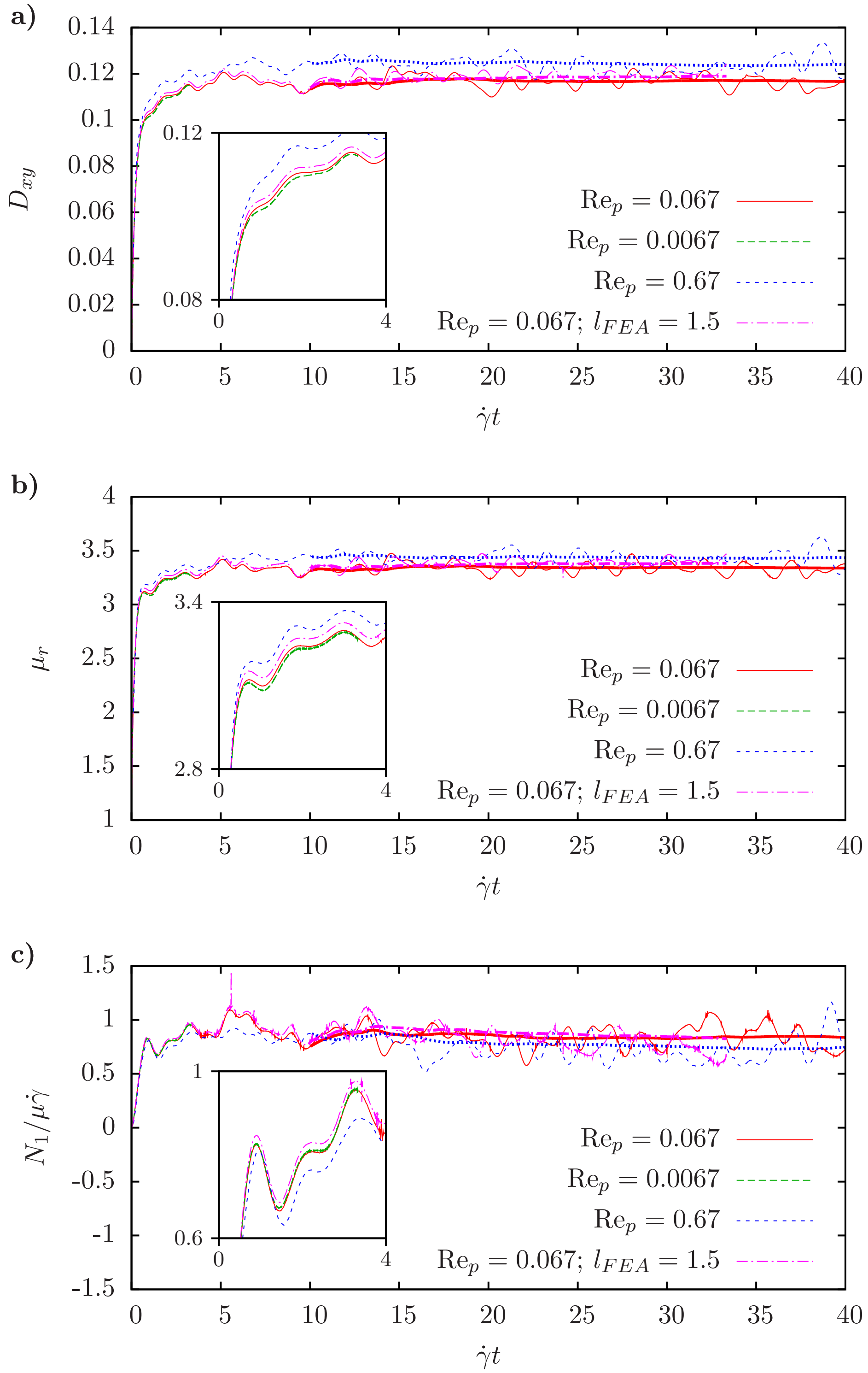

Figure 39: Transient behavior of microstructure and rheology for a suspension of 285 capsules with $\mathrm{Ca}_G = 0.02$ as a function of Re_p. Results show the (a) deformation index, (b) relative suspension viscosity, and (c) first normal stress difference, with short-time transient behavior shown in inset. Thin lines show transient behaviors, while thick lines show time-averaged values starting at $\dot{\gamma} = 10$.

This unstable behavior is not unique to this methodology, even for rigid particle suspensions, thus alternate numerical schemes frequently introduce repulsive forces (Brady & Bossis, 1988; Nguyen & Ladd, 2002; Sierou & Brady, 2002). Several issues serve to worsen the stability for the LB/FE method. Since the number and positions of the links change as the particle traverses the underlying LB grid, large fluctuations in the lubrication force are seen, which is localized to the few links that are present in the gap between the particles. The magnitudes of these fluctuations are quantified in the model problems found in section 2.3.2, and the fluctuations are dependent on link creation and destruction and not necessarily the discrete time step used in integration process. These fluctuations are especially troublesome for capsules, since the large lubrication forces, which are concentrated in just a few links, are no longer averaged into an overall force, as is the case with rigid particles. The large force oscillations can be seen in Figure 40, where red and blue areas denote large magnitude compressive and tensile normal stresses, respectively. To maintain stability, minimal lubrication modeling can be used, and a relatively soft contact force is required.

Transitioning the subgrid modeling scheme to a non-link-based model is critical for making headway towards accurately resolving lubrication hydrodynamics at small gaps. Such as scheme would be based solely on the solid geometry, and thus would not share the discontinuous fluctuation in lubrication force due to creating and destruction of links. Higher-order interpolation functions could be used for the surface elements, which would increase the "smoothness" of the particle surface. Discontinuities in the force would be a function of the integration time step, and not the creation of links, thus higher-order integration schemes may prove helpful.

Nevertheless, some headway can be made with rigid particle suspensions, in which the motion of the particle is governed by the total force on the particle, and inertial damping from the entire particle mass increases the stability. In order to quantify the impact of the contact parameters on suspension rheology, a small study on the

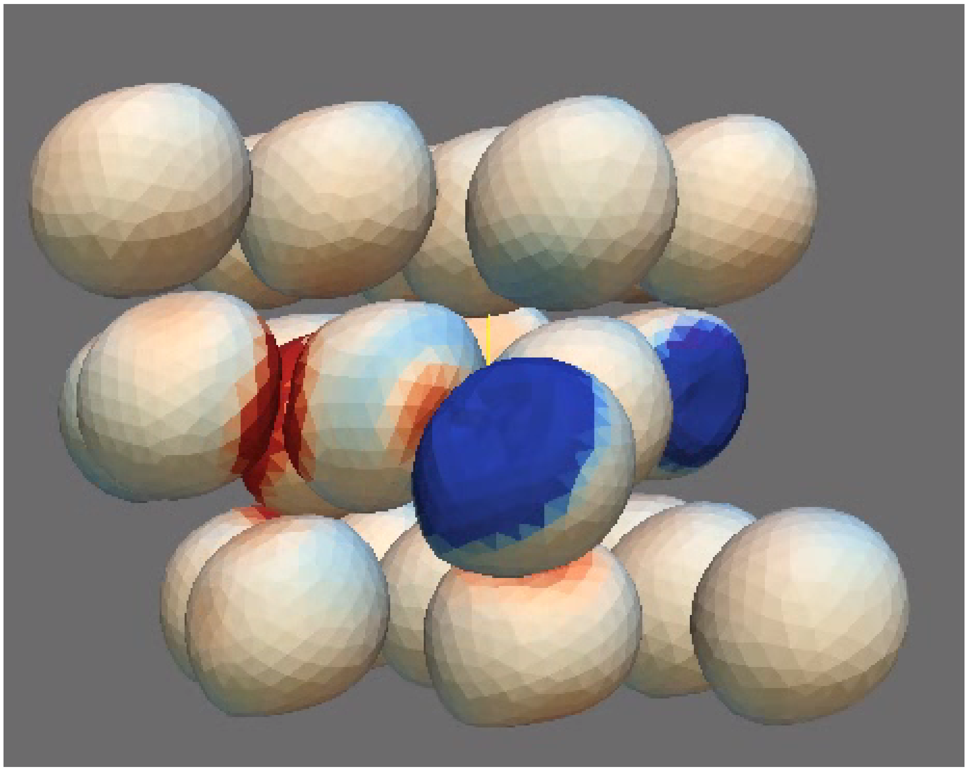

Figure 40: Test simulation of 25 deformable capsules in shear with subgrid modeling enabled. Oscillations in the surface velocity creates large fluctuations in surface forces, which can be seen as large negative (blue) and positive (red) normal stresses. Also note the wrinkling of the FE surface.

Table 5: Parameters used to study effect of subgrid modeling on rheology. Simulations progress from relatively soft contact to stiffer, shorter-ranged contact. Simulation A does not use subgrid lubrication modeling since $g_c = 0.05$ corresponds to half a lattice unit, where hydrodynamics are reasonably recovered. Simulations B–D use the subgrid lubrication model discussed in section 2.3.2.

Sim	$\tilde{A}_c$	$\tilde{\sigma}_c$	$\tilde{g}_c$
A	1.273	0.0075	0.05
B	4.0	0.0054	0.03
C	7.958	0.0041	0.02
D	14.15	0.0035	0.015

effect of the contact and lubrication parameters is made for suspensions of rigid spherical particles, with $l_{FEA} = 2.0$, $\phi = 40\%$, and $\mathrm{Re}_p = 0.067$. Table 5 details the nondimensional contact parameters used for simulation runs A–D, with the contact forces becoming progressively shorter ranged and stiffer. Simulations B–D include the subgrid lubrication model, while simulation A only uses the contact model, which increases the stability of the method. Note that the parameters chosen in Table 5 result in the same nondimensional contact force when the gap is zero.

Rheology results for the various simulations can be found in Figure 41(a–d) with thin lines showing transient, particle-averaged behavior, and heavy lines showing time-averaged results. The transient behavior is not plotted after 35 strain units to highlight time-averaged results. One can see a pronounced decrease in the suspension viscosity, seen in Figure 41(a), which is expected since lubrication forces are dissipative in nature. Such results are also confirmed in alternate numerical methods (Sierou & Brady, 2002), which can resolve much smaller gaps owing to the ideal spherical representation of particles. The viscosity of rigid suspensions will be discussed in section 5.3.1, where a large degree of variation is seen in the experimental results for the shear viscosity at high volume fraction. Normal stresses are much less sensitive to the variations in the interparticle force, as seen in Figures 41(b–d), a results also supported by Stokesian dynamics simulations (Sierou & Brady, 2002). In general,

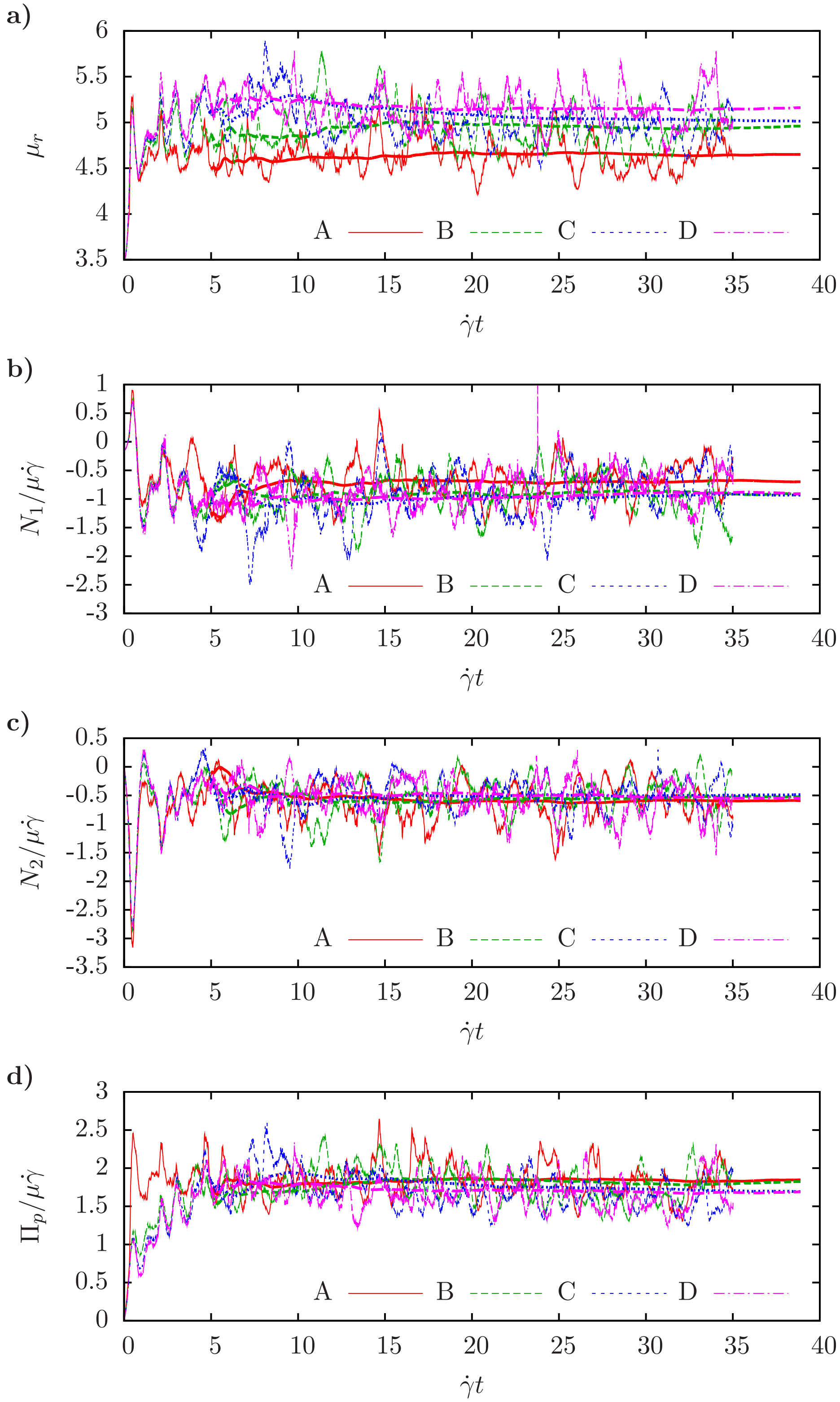

Figure 41: Effect of subgrid modeling for simulations of 285 rigid spheres at 40% volume fraction. Results show the (a) relative viscosity, (b) first normal stress difference, (c) second normal stress difference, and (d) particle pressure. Thin lines show transient behaviors, while thick lines show time-averaged values starting at $\dot{\gamma} = 10$.

Table 6: Simulations that are used in parametric study of capsule rheology.

ϕ	N	**Domain**	**Ca$_G$**
0.1	180	196^3	0.0, 0.02, 0.04
0.2	196	160^3	0.0, 0.005, 0.01, 0.02, 0.03, 0.04
0.3	214	144^3	0.0, 0.02, 0.04
0.4	285	144^3	0.0, 0.002, 0.005, 0.01, 0.02, 0.03, 0.04

rigid particle suspensions show larger transient fluctuations in the rheological results than deformable capsules, such as the Ca$_G$ = 0.02 case shown in Figures 38 and 39. The LB/FE method is currently not an ideal method for the investigation of contact or other interparticle forces on the rheology and microstructure, and thus this thesis does not explore these effects in depth. Deviations in the rheology due to interparticle forces can be significant in experimental results, as will be seen in section 5.3.1.

5.3 Simulation results

A large-scale parametric study of the rheology and microstructure of capsule suspension is performed. Based on the studies in the previous section, the simulations are composed of roughly 200 deformable particles with $l_{FEA} = 2.0$ and $a = 10$ lattice spacings. Simulations are performed in simple shear using the Lees–Edwards boundary condition (LEbc) to eliminate wall effects. Inertial effects are minimal with $\mathrm{Re}_p = 0.067$ and $\mathrm{Ma} < 0.03$ for all simulations. The contact parameters used are $A_c = 4.0$, $\sigma_c = 0.00543$, and $g_c = 0.05$. The study includes several volume fractions and Ca$_G$, as outlined in Table 6.

5.3.1 Comparison to rigid results

Before introducing particle deformation, suspensions of rigid spheres are compared with existing experimental and numerical results. Simulations are performed for the Ca$_G$ = 0.0 cases shown in Table 6, and the results are presented in this section. Viscosity results for suspensions of rigid spherical particles are prevalent in literature, both experimentally and numerically.

As discussed in section 1.2, this thesis is focused on noncolloidal suspensions in which the effects of Brownian motion and inertia are both negligible. This region corresponds to the so-called high-shear viscosity regime, and is ideally treated as Newtonian (Stickel & Powell, 2005). Theoretically, the suspension viscosity is strictly a function of the volume fraction, and many attempts have been made to fit empirical curves to rheological data in this regime. Common fits include the Krieger–Dougherty relation (Krieger & Dougherty, 1959)

$$\mu_r = \left(1 - \frac{\phi}{\phi_m}\right)^{-[\mu]\phi_m}, \tag{74}$$

and the fit of Eilers (1941) (Zarraga et al., 2000)

$$\mu_r = \left(1 + \frac{1.5\phi}{(1 - \phi/\phi_m)}\right)^2, \tag{75}$$

where ϕ_m is the maximum packing fraction, and $[\mu]$ is the intrinsic viscosity. In practice, suspensions are less ideal than these relations suppose, as demonstrated in Figure 42, and ϕ_m and $[\mu]$ are used as a fitting parameters. For example, Papir & Krieger (1970) suggest using $\phi_m = 0.68$ and $[\mu] = 2.67$ in (74) to accurately fit the high-shear viscosity of polystyrene spheres with a = 75–215 nm in benzyl alcohol or metacresol, with both empirical fit and data shown in Figure 42. These viscosities are significantly lower than those reported by Zarraga et al. (2000), who use $\phi_m = 0.58$ in (75) to fit the rheological data from spheres ranging from $43.0 - 73.6$ μm in size. Experimental data and fit from Zarraga et al. (2000) are shown in Figure 42. Additionally, many suspensions are known be shear-thinning at regions well past the transition from the low- to high-shear limits (Zarraga et al., 2000; Stickel & Powell, 2005), an effect which is not captured in the above empirical fits and currently lacks explanation.

These deviations in rheology can be explained by differences in interparticle forces. Mewis et al. (1989) studied the rheology of suspensions with a variety of particle sizes,

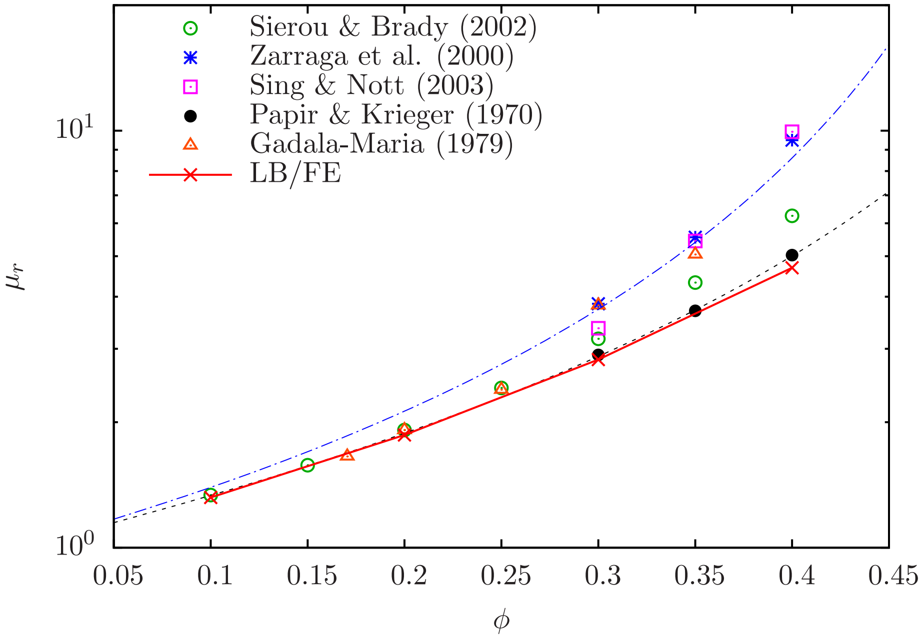

Figure 42: Relative viscosity as a function of the volume fraction for rigid sphere suspensions. Empirical fits include the Krieger–Dougherty relation (- - -) for the data of Papir & Krieger (1970) and the Eilers fit (– · –) for the data of Zarraga et al. (2000).

and found that when sterically stabilized, smaller particles were effectively softer due to the relatively (in terms of the particle radius) larger-ranged interparticle forces. This observation is corroborated by SD simulations, in which larger interparticle forces reduced the suspension viscosity (Sierou & Brady, 2002). The brief study of contact forces in section 5.2.3 also supports this hypothesis. Since lubrication forces are dissipative in nature, the decreased suspension viscosity is a direct result of the larger particle gaps, and thus smaller lubrication forces, that are seen in the presence of larger repulsive interparticle forces.

The relative viscosity calculated from the LB/FE results for rigid suspensions in simple shear is also shown in Figure 42. In addition to the previously mentioned results of Papir & Krieger (1970) and Zarraga et al. (2000), experimental results from Singh & Nott (2003) and Gadala-Maria (1979), and Stokesian dynamics (SD) numerical results from Sierou & Brady (2002) are also shown. Excellent agreement between experimental and numerical results are seen at lower volume fractions, with some divergence seen at higher concentrations. The LB/FE results are among the lowest in viscosity; however, the results are within the range measured experimentally. Good agreement is seen between the results of Papir & Krieger (1970) and the LB/FE simulations. These results share the attribute that the suspensions tested contain the relatively largest interparticle repulsive forces.

Experimentally measuring the normal stresses in suspensions of rigid spherical particles is much more challenging than measuring the viscosity. The presence of normal stresses these suspensions was first observed by Gadala-Maria (1979); however, his results were subject to large errors. More recent results by Zarraga et al. (2000) used a variety of techniques that included using the resuspension data of Acrivos, Mauri & Fan (1993), parallel-plate and cone-and-plate viscometers, and surface profilometry to accurately resolve the separate normal stress components. Zarraga et al. (2000) proposed the following empirical fits to their data:

$$\left.\begin{aligned}\frac{\Sigma_{11}}{\mu_r\mu\dot{\gamma}} &= -2.50\phi^3 e^{2.34\phi}\\ \frac{\Sigma_{22}}{\mu_r\mu\dot{\gamma}} &= -2.17\phi^3 e^{2.34\phi}\\ \frac{\Sigma_{33}}{\mu_r\mu\dot{\gamma}} &= -\phi^3 e^{2.34\phi}\end{aligned}\right\}. \tag{76}$$

Perhaps the most accurate results are those presented by Singh & Nott (2003), in which the normal stress differences were measured using a sinusoidal varying shear rate in a combination of parallel-plate and Couette viscometers. Figures 43(a–c) summarize these experimental findings along with the LB/FE simulation data.

The LB/FE results agree well with the experimental results of Singh & Nott (2003) for N_1 at high volume fraction, as seen in Figure 43(a). At higher concentrations, a qualitative agreement is seen with the empirical fit of Zarraga and the SD results of Sierou & Brady (2001); however, at lower volume fractions, some deviation in the

LB/FE results is seen. In general, the empirical fit of Zarraga underpredicts N_1 relative to other experimental and numerical methods. The deviation between the LB/FE results and the other results at low volume fraction could be the result of numerical errors because the magnitude of N_1 is exceedingly small at these concentrations.

The four methods show much better agreement with respect to N_2, as seen in Figure 43(b), where the LB/FE and SD methods tend to underprect the magnitude. Experimental studies tend to find $N_2 > N_1$, while the numerical results of the LB/FE method and SD put the first and second normal stresses at roughly the same magnitude. The interparticle force has been implicated in this discrepancy (Singh & Nott, 2003), although this theory is inconclusive. Particle pressure results are not available from Singh & Nott (2003); however, decent agreement is seen between the empirical fit, SD simulations, and the LB/FE method, seen in Figure 43(c).

Also shown in Figure 43(c) are the results of Deboeuf et al. (2009), in which the particle pressure was measured by attaching a screened manometer tube to the side of a continuously sheared Couette viscometer. The increase in particle pressure creates an effect analogous to that of an osmotic pressure, i.e., the partial pressure of the fluid phase decreases. Thus, the shearing motion of the suspension creates a drop in the fluid pressure as measured in the manometer. The scatter in results correspond to measurements with various sized particles.

The individual normal stress components are shown in Figure 44. Qualitatively, experimental, Stokesian Dynamics, and LB/FE results show increasingly negative normal stress components, with $\Sigma^p_{11} > \Sigma^p_{22} > \Sigma^p_{33}$; however, quantitative differences exist. The empirical fit of Zarraga et al. (2000) underpredicts the difference between Σ^p_{11} and Σ^p_{22}, with both the LB/FE and SD results (Sierou & Brady, 2002) showing larger differences, as seen in Figure 44. This underprediction in $\Sigma^p_{11} - \Sigma^p_{22}$ was also seen as an underprediction in N_1 in Figure 43(a). While the SD results follow the fit of Zarraga et al. (2000) reasonably well, the LB/FE results diverge at lower volume

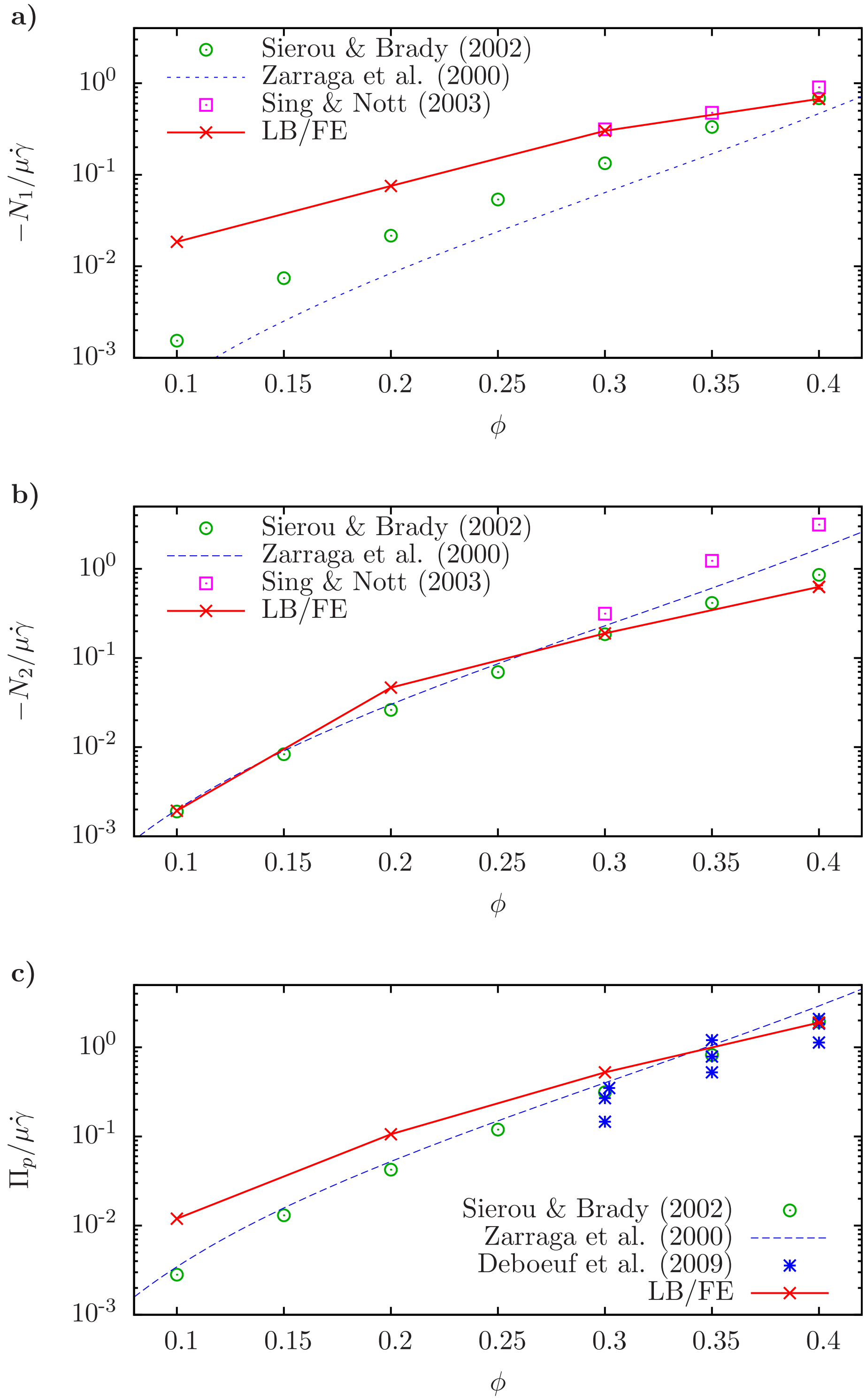

Figure 43: Normal stress results for suspension of rigid spherical particles in unbounded shear as a function of volume fraction. Results show the (a) first normal stress difference, (b) second normal stress difference, and (c) particle pressure.

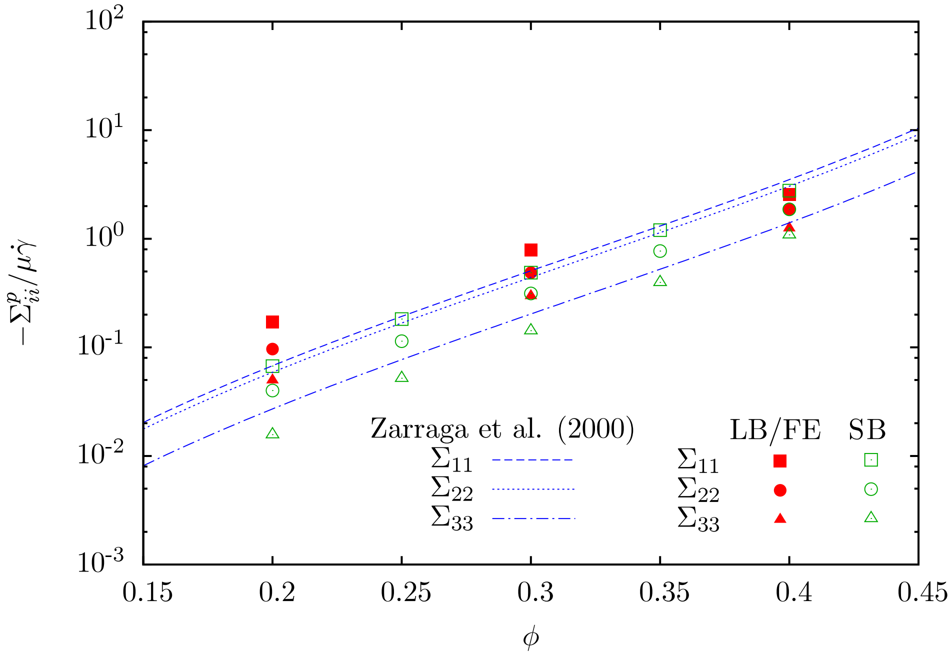

Figure 44: Individual components of the normal stresses as a function of volume fraction. LB/FE results are shown as solid symbols, Sierou & Brady (2002) (SB) results are shown as outlined symbols, and the proposed empirical fits of Zarraga et al. (2000) are shown as dashed lines.

fractions where the magnitude of the normal stresses is quite small.

5.3.2 Capsule rheology

Now that the rheological behavior and accuracy of the LB/FE method has been demonstrated in the rigid limit, a detailed study characterizing the effect of particle deformation is performed. In dense suspensions, the elasticity parameter is more accurately scaled by defining an effective capillary number, shown as

$$\mathrm{Ca}_{G,\mathrm{eff}} = \frac{\mu_r \mu \dot{\gamma}}{G_M}, \tag{77}$$

in which the viscous stresses are scaled by the effective suspension viscosity ($\mu_r\mu$).

Figure 45 shows the shear-thinning behavior of capsule suspensions as the deformation of the solid phase is increased. At high concentrations, the shear-thinning is much more pronounced. For the $\phi = 0.4$ case, the relative viscosity decreases from

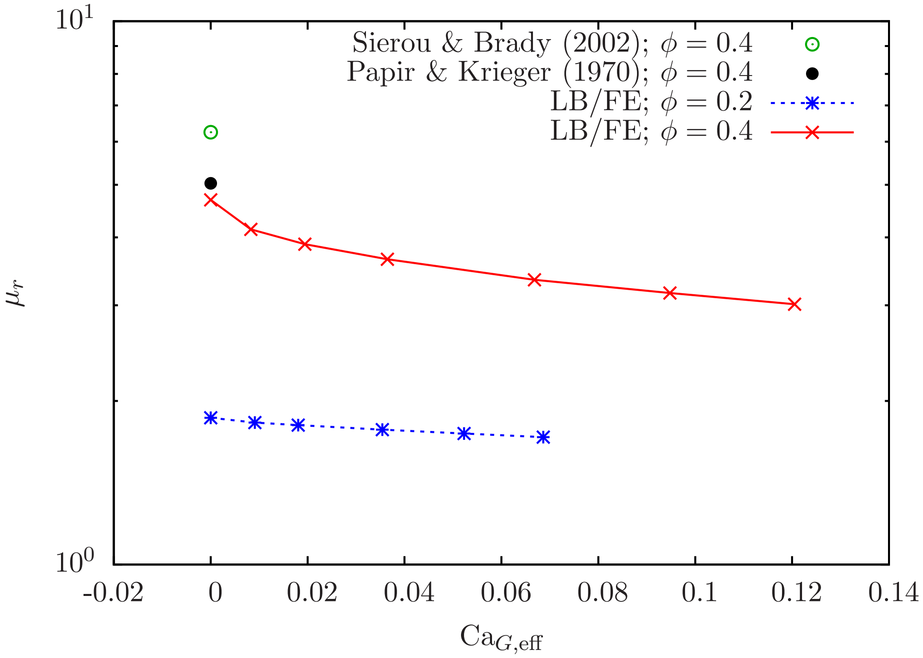

Figure 45: Relative viscosity of capsule suspension as a function of the elasticity parameter $\mathrm{Ca}_{G,\mathrm{eff}}$. Volume fractions of 20% and 40% are shown.

4.7 to 3.0 over the range of $\mathrm{Ca}_{G,\mathrm{eff}}$ simulated. In contrast to the dilute capsule results shown in section 4, the decrease in viscosity is most prominent in the near-rigid limit. This behavior seems to imply that the initial reduction in viscosity is driven by changes in the particle interactions, hence altering the configurational microstructure, and not by the single-body change in particle shape. Suspension microstructure will be examined in more detail in section 5.3.3.

Figures 46(a–c) show the behavior of the normal stresses as deformation is increased. The first normal stress difference, shown in Figure 46(a) undergoes a change in sign, from negative where the anisotropy due to the the particle microstructure is aligned with in the compressional quadrant, to positive where individual capsules have a preferential orientation along the extensional quadrant. At $\phi = 0.2$, similar behavior is seen, but the magnitudes are much smaller. Both 20% and 40% concentrations appear to reach zero N_1 at similar $\mathrm{Ca}_{G,\mathrm{eff}}$; however, it is not know if this trend will continue at other concentrations. The second normal stress difference, shown in

Figure 46(b) is much more inconclusive; N_2 remains negative with a slight decrease in magnitude due to capsule deformation. Perhaps most surprising is the particle pressure, shown in Figure 46(c), which decreases rapidly with the onset of deformation. Some of this decrease is attributable to the negative pressure generated by an isolated capsule (see section 4); however, alterations in interparticle interactions could also play a role.

Other simulation results for deformable particles are confined to droplets in emulsion flow. Loewenberg (1998) simulates up to 12 deformable droplets using a boundary integral formulation. Qualitatively, the droplet dynamics are similar to elastic capsules. The initially spherical droplets deform into ellipsoids and align with the flow direction; a positive N_1 and negative N_2 are generated. Rheological measurements show qualitative differences, however, and in the limit $\mathrm{Ca} \to 0$, the rheology does not converge to those of rigid spheres. The capillary number is defined for droplets as $\mathrm{Ca} \equiv \mu\dot{\gamma}a/\gamma_{it}$, where γ_{it} is the interfacial tension. Instead, Loewenberg (1998) reports zero normal stress differences. As deformation increases, rheology measurements do not appear to converge to a limiting value, but instead diverge, with N_1 rapidly increasing at $\mathrm{Ca} \sim 0.4$. Particle pressure is not reported.

The boundary integral results of Zinchenko & Davis (2002) are in better qualitative agreement with the LB/FE results. In these simulations, up to 200 deformable droplets are simulated in unbounded shear. Again, dynamics are similar, and positive N_1 and negative N_2 rheology is seen. More importantly, rheology measurements appear to be leveling off as deformation increases, in contrast to the divergent behavior of Loewenberg (1998). Simulation results are constrained to $\mathrm{Ca} > 0.05$; therefore, it is difficult to make comparisons to rigid sphere rheology. N_1 is positive for all simulation results, although it appears that a negative value will be obtained prior to $\mathrm{Ca} = 0.0$. Again, particle pressure results are not reported.

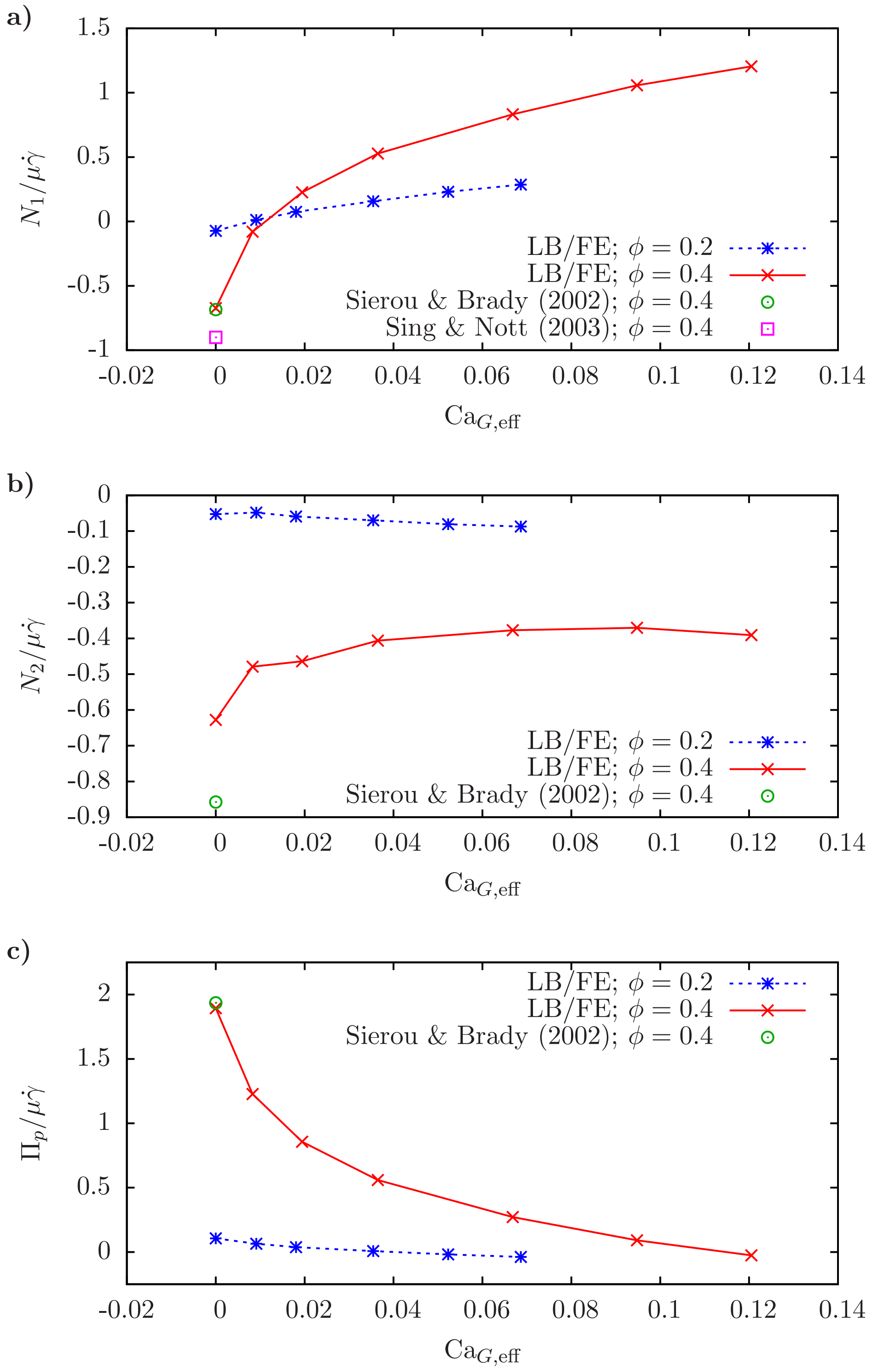

Figure 46: Normal stress quantities of capsule suspensions as a function of the elasticity parameter $\mathrm{Ca}_{G,\mathrm{eff}}$. Volume fractions of 20% and 40% are shown for (a) first normal stress difference, (b) second normal stress difference, and (c) particle pressure.

5.3.3 Capsule microstructure

Quantifying the changes in suspension microstructure is critical to providing physical insight into the observed changes in suspension rheology caused by particle deformation. The dilute-limit microstructure for capsules was extensively probed in section 4, and this section presents average capsule microstructure using the Taylor deformation parameter (D_{xy}) and the capsule orientation (θ), with definitions identical to those in section 4. Additionally, the configurational microstructure, as quantified by the pair-distribution function $g(\boldsymbol{r})$, is discussed.

Figures 47(a and b) show these parameters as a function of the effective capillary number, $\mathrm{Ca}_{G,\mathrm{eff}}$. If we assume that the average capsule deformation is a function of the average shear stress in a suspension, then the microstructure parameters D_{xy} and θ will be only weak functions of the volume fraction. The deformation parameter, shown in Figure 47(a), largely behaves in this manner, especially as $\mathrm{Ca}_G \to 0$; however, the orientation angle, θ, shows a shift towards the extensional axis at higher volume fractions. One possible explanation for this shift could be the asymmetry found in the pair-distribution function at higher concentrations. Figure 48 shows the angular dependence on the pair distribution function as a function of volume fraction. Data are taken from Sierou & Brady (2002), and θ as been made consistent with the definition in this thesis. As the concentration increases, the asymmetry is progressively skewed towards the flow direction in the compressional quadrant ($\pi/2 < \theta < \pi$). As schematically shown in Figure 48, this asymmetry creates a torque that promotes an alignment further from the flow direction.

The pair distribution function is calculated for the LB/FE simulations using a standard binning procedure (Morris & Katyal, 2002), and asymmetry in the pair-distribution function can be visualized by looking at the projection of $g(\boldsymbol{r})$ on the xy (flow and shear-gradient) plane, as seen in Figures 49(a–d) for several different $\mathrm{Ca}_{G,\mathrm{eff}}$. At large $\mathrm{Ca}_{G,\mathrm{eff}}$, the pair distribution function clearly shows the ellipsoidal

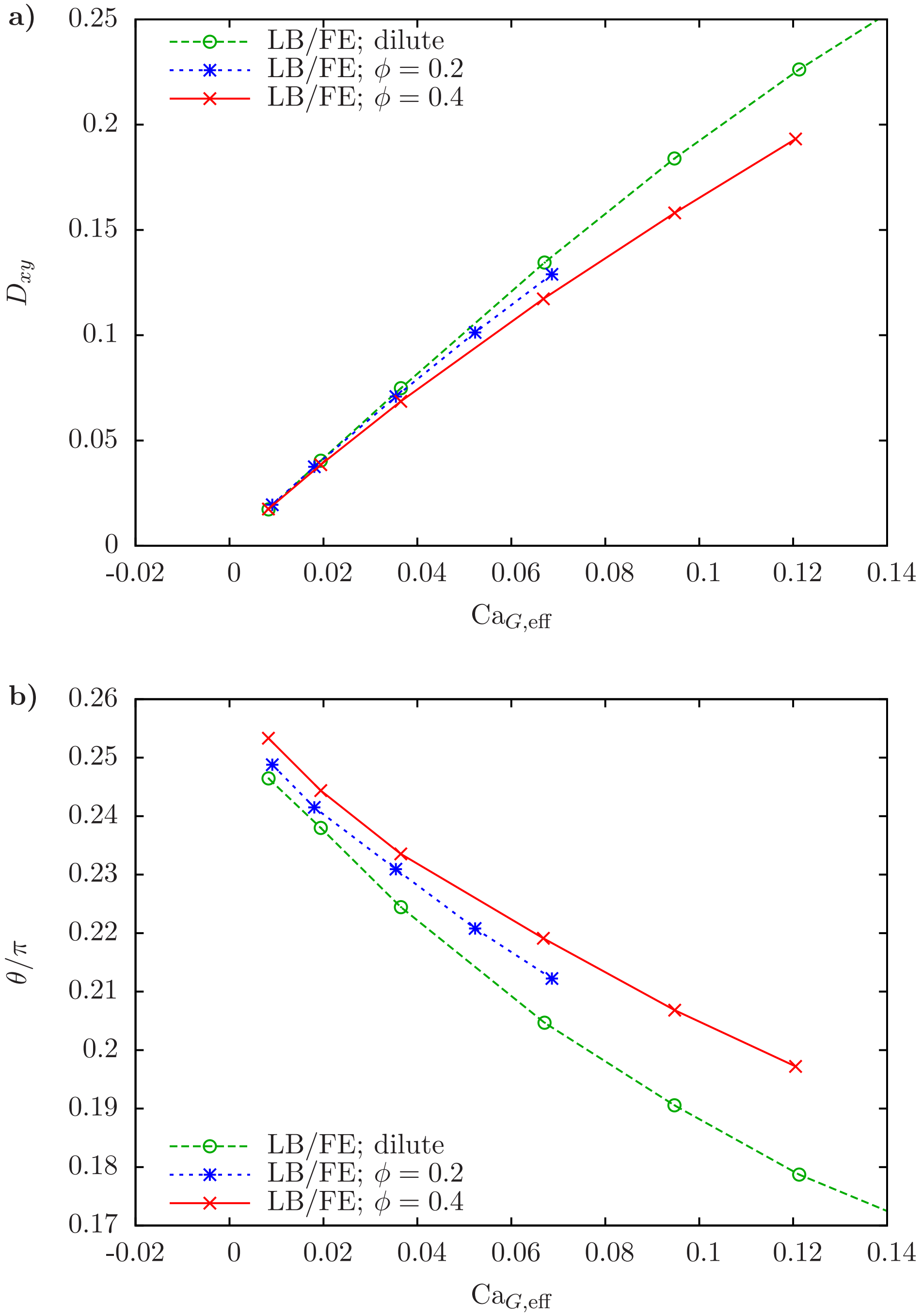

Figure 47: Single-body microstructure in capsule suspensions as a function of Ca_G showing the (a) Taylor deformation parameter and (b) orientation of the capsule with the flow (x) direction

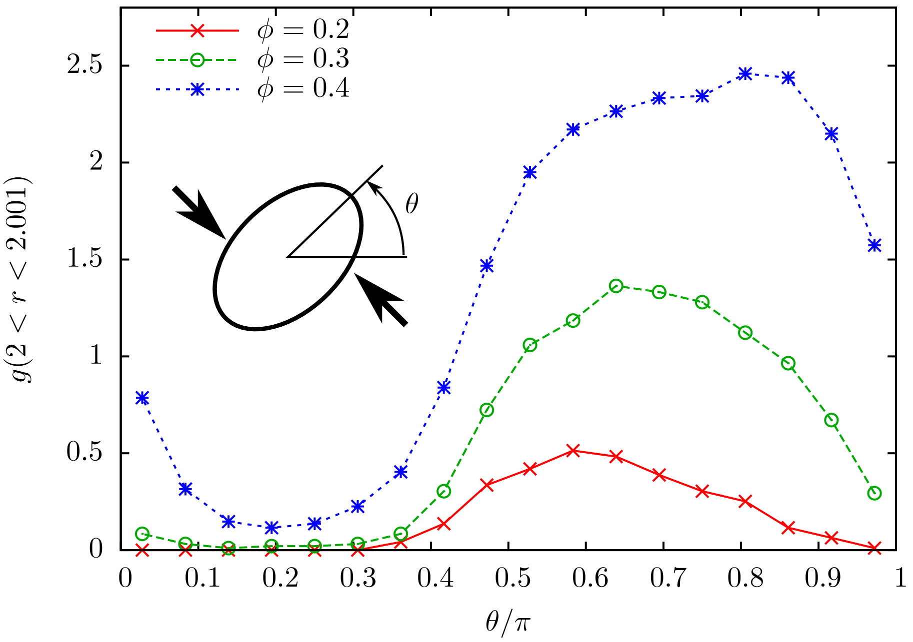

Figure 48: Results from Sierou & Brady (2002) that show a skewing of the angular dependence of the pair distribution function towards the x axis in the compressional quadrant at higher particle concentration. As a result, compressive forces corresponding to the peak in the pair distribution function create a torque on the deforming capsule opposing the dilute tendency of a capsule to orient along the flow direction.

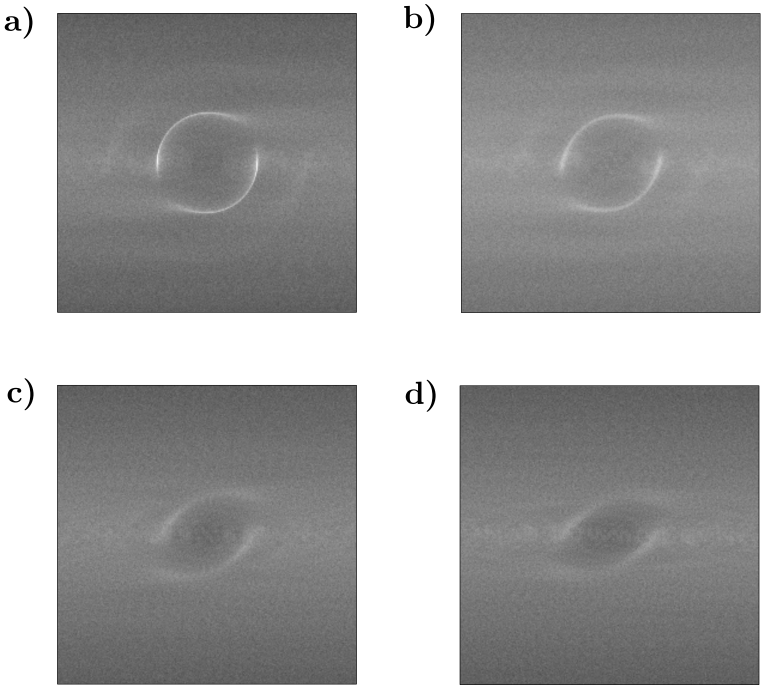

Figure 49: Projection of $g(\boldsymbol{r})$ in the xy plane for (a) $\mathrm{Ca}_{G,\mathrm{eff}} = 0.0$, (b) $\mathrm{Ca}_{G,\mathrm{eff}} = 0.01$, (c) $\mathrm{Ca}_{G,\mathrm{eff}} = 0.07$, and (d) $\mathrm{Ca}_{G,\mathrm{eff}} = 0.12$. All simulations are $\phi = 0.4$

shape of the deformed capsule with a much less defined and softer contact region. The deformation in Figure 49(b) is very minor (see Figure 31 for relative deformation), yet the pair-distribution function shows a noticeable ellipsoidal shape, which highlights the impact of capsule deformation on particle interactions that exceeds the simple change in geometry. Also note the slight appearance of bands aligned with the flow in the rigid and near-rigid cases. Such bands are not reported in Stokesian dynamics simulations at these concentrations; however, order in suspension microstructure has been noted in simulations at higher concentrations (Morris & Katyal, 2002; Sierou & Brady, 2002). Experimentally, order has been seen in electrostatically stabilized suspensions (Chen, Ackerson & Zukoski, 1994) suggesting that the relatively large interparticle force present in the LB/FE simulations may play a role.

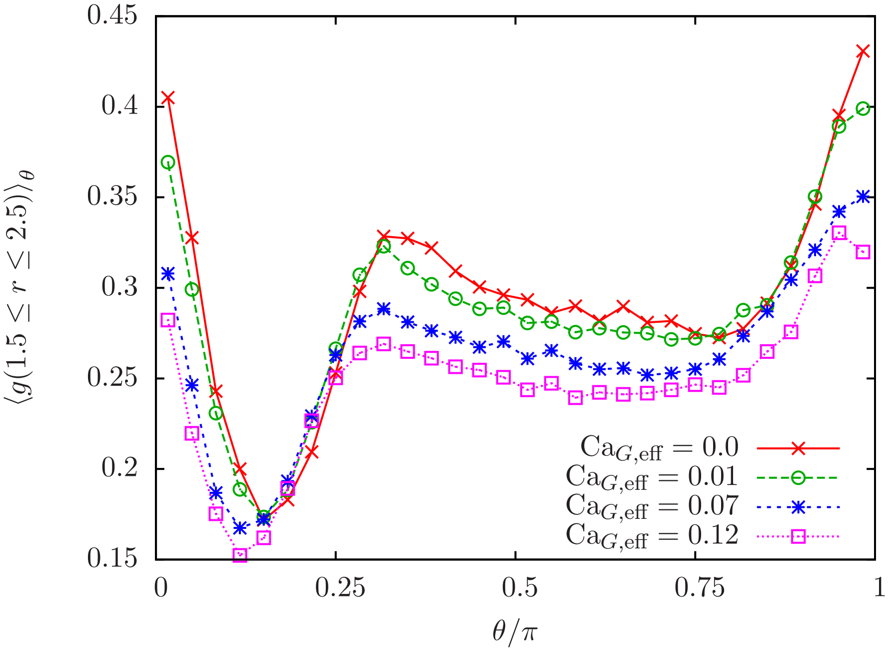

Figure 50: Angular dependence of pair distribution function for various Ca_G at $\phi = 0.4$. Reduced asymmetry reduces the impact of particle configuration on the rheology as deformation increases.

The angular dependence of the pair-distribution function can be plotted for the LB/FE results; however, care must be taken to use a sufficiently sized radial range since the particle border is no longer spherical. Figure 50 shows the angular dependence for several $\mathrm{Ca}_{G,\mathrm{eff}}$, and a decrease in the asymmetry is seen at higher deformations. The deformation serves to reduce the impact of asymmetry in the particle configuration. Thus, the negative first normal stress difference seen in Figure 46a, which is generated via asymmetry in the pair-distribution function, relaxes as even minor levels of deformation are introduced. Stated another way, particle deformation tends to create softer interactions with larger gaps between particles, which reduces the impact of the configurational microstructure on the overall rheology. These effects, combined with the dilute-limit normal stress differences generated by the ellipsoidal shape of the deformed capsule, cause the sign change as the capillary number increases.

5.4 Limitations of modeling

Dilute-limit modeling of capsule dynamics was discussed in detail in chapter 4, and analytical models based on asymptotic expansions in the spherical limit, while qualitatively useful in describing several effects of deformation, are quantitatively inaccurate at anything but minimal deformations. More importantly, even with a completely accurate description of the dilute-limit capsule rheology, a model that neglects the impact of deformation on the particle configuration will have a qualitatively inaccurate description of the suspension rheology. As seen in the previous section, the pair-distribution function changes rapidly at even minimal deformations, and this change manifests itself as a rapid change in the rheology of these suspensions. Thus, modeling of capsule suspensions suffers the same difficulties seen in modeling rigid particle suspensions: detailed statistical knowledge of the particle configuration is required. Deformation complicates the description of the microstructure by causing large changes in the particle configuration.

For example, the predictive model of Pal (2003), shown previously in (19), is based on the dilute-limit and nearly spherical model of Goddard & Miller (1967). This model, as shown in Figure 51, predicts an initially gradual shear-thinning behavior. Although Pal (2003) uses the differential effective medium approach (DEMA), the deformation is essentially a scaling factor to the particle stress due to deformation which is based in the dilute limit. The modeling of Pal (2003) is shown in Figure 51 using the fitting parameters from Papir & Krieger (1970). Again, note the qualitatively incorrect behavior of shear thinning, in which the gradient in the viscosity is at a minimum as $\mathrm{Ca}_{G,\mathrm{eff}} \to 0$ in contrast to the simulation results.

One could adapt the dilute simulation results from section 4 to describe the effect of deformation assuming that changes in rheology exist on a particle-by-particle basis, which neglects the influence of deformation on the particle configuration. This assumption is incorrect, but it highlights the large changes in particle microstructure

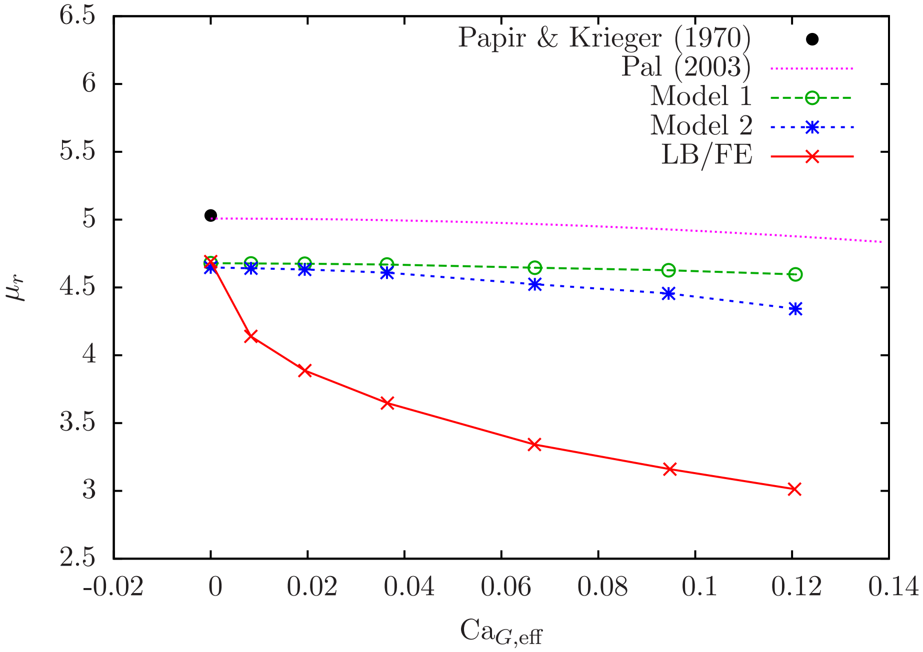

Figure 51: Inaccuracy of rheology models that neglect deformation-induced changes in particle configuration.

caused by particle deformation. Starting with the nondimensional form of Batchelor's equation (5), shown as

$$\langle \mathbf{\Sigma} \rangle = -\langle P_f \rangle \mathbf{I} + 2\mu \langle \mathbf{E} \rangle + \phi \langle \mathbf{S} \rangle , \tag{78}$$

where all quantities are nondimensional, the particle influence to the overall stress can be separated into a component equal to that of a rigid suspension, and a deviation from this value brought caused by particle deformation. If one assumes that the only influence of deformation is single-body, the deviation from rigid results will scale identically to the dilute capsule results in section 4. Consequently, the overall suspension stress can be written as

$$\langle \mathbf{\Sigma} \rangle \approx -\langle P_f \rangle \mathbf{I} + 2\mu \langle \mathbf{E} \rangle + \phi \left(\langle \mathbf{S}_r \rangle + \mathbf{S}_{dc} - \mathbf{S}_{dr} \right) , \tag{79}$$

where the subscripts dc and dr refer to dilute-capsule and dilute-rigid stresslets, respectively. $\langle \mathbf{S}_r \rangle$ is known from the concentrated rigid particle simulations, $\mathbf{S}_{dc}$ is known from the capsule simulations given in section 4, and $\mathbf{S}_{dr} = 5/2$. This model, referred to as Model 1 in Figure 51, drastically underpredicts the deformation-induced shear-thinning behavior seen in the LB/FE simulations. Although not shown, predictions in normal stress differences are equally poor.

A more simplistic model is to simply scale the particle stress according to $\mathbf{S}_{dc}/\mathbf{S}_{dr}$, i.e.,

$$\langle \mathbf{\Sigma} \rangle \approx -\langle P_f \rangle \mathbf{I} + 2\mu \langle \mathbf{E} \rangle + \phi \left(\langle \mathbf{S}_r \rangle \frac{\mathbf{S}_{dc}}{\mathbf{S}_{dr}} \right), \tag{80}$$

where this model is referred to as Model 2 in Figure 51. Again, qualitatively incorrect behavior is observed, although this model is more comparable to that of Pal (2003). Furthermore, this model is incapable of recovering any alterations to the normal stresses, since $\mathbf{S}_r$ is zero for any normal components. Any rheological modeling of deformation in dense suspensions must account for the rheological changes caused by changes to both the single-body and configurational microstructure.

5.5 Individual normal stress components and implications for particle migration

According to the suspension-balance model (Nott & Brady, 1994), particle migration is driven by gradients in the normal stresses. At an equilibrium concentration, the particle-phase momentum must satisfy

$$\nabla \cdot \mathbf{\Sigma}^p = 0, \tag{81}$$

as discussed in section 1.3 (see also Nott & Brady, 1994; Morris & Boulay, 1999). In rigid suspensions, the normal stresses are a function of the volume fraction and show a linear dependence on the shear stress. In capsule suspensions, normal stresses are also functions of particle deformation, itself a function of the shear rate, which adds a complex interplay between these parameters. Figures 52(a and b) show the individual components of a deformable capsule suspension at 20% and 40% volume fractions, respectively. In general, deformation introduces a shift towards tensile (positive) normal stresses, with the shift more pronounced at higher concentrations.

In particular, the flow-direction stress, Σ_{11}^{p} shows a large change, proceeding from a large compressive stress at $\mathrm{Ca}_{G,\mathrm{eff}} = 0.0$ to a large tensile stress as $\mathrm{Ca}_{G,\mathrm{eff}}$ increases. This trend directly relates to the tensile stresses found in the solid phase as the initially spherical capsules deform into ellipsoids that align in the flow direction. Less pronounced shifts are seen in the shear-gradient and vorticity directions. The Σ_{22}^{p} results in Figure 52a disagree with the general trend towards tensile normal stresses, and instead demonstrates a small tensile shift, followed by a leveling off and perhaps more compressive stresses. One potential explanation is the competition between configurational and single-body microstructure. For example, in the near-rigid limit, changes to the configuration would dominate; consequently, Σ_{22}^{p} follows the general trend of decreasing compressive stresses. At more moderate deformation, the single-body effects are more prominent demonstrating a trend towards more compressive Σ_{22}^{p}, as shown in Figure 36. Figure 52c shows the Σ_{22}^{p} component of the normal stresses as a function of volume fraction, with various Ca_G denoted by various curves.

Predicting the equilibrium concentration, even considering an accurate description of $\boldsymbol{\Sigma}^{p} = \boldsymbol{\Sigma}^{p*}(\phi, \mathrm{Ca}_G)\mu\dot{\gamma}$, is a highly coupled problem. For illustrative purposes, consider the case of a suspension in pressure-driven channel flow, as shown in Figure 53. At equilibrium, the particle y momentum balance must satisfy $\Sigma_{22}^{p} = C$, where C is an arbitrary constant. In contrast to a simple Newtonian fluid, the local viscosity is a strong function of ϕ; therefore, the local shear rate is coupled to ϕ. The same is true of the capillary number, which is dependent on the local shear and viscosity. For rigid particles, $\mathrm{Ca}_G = 0.0$ everywhere, thus the equilibrium concentration can be calculated by following the $\mathrm{Ca}_G = 0.0$ curve in Figure 52c until the proper Σ_{22}^{p*} is obtained.

For example, consider two regions in the pressure-driven flow, marked region 1 and 2 in Figure 53, in which the shear rate of region 2 is twice the shear rate in region 1. The dimensional Σ_{22}^{p} is constant between regions when the dimensionless normal

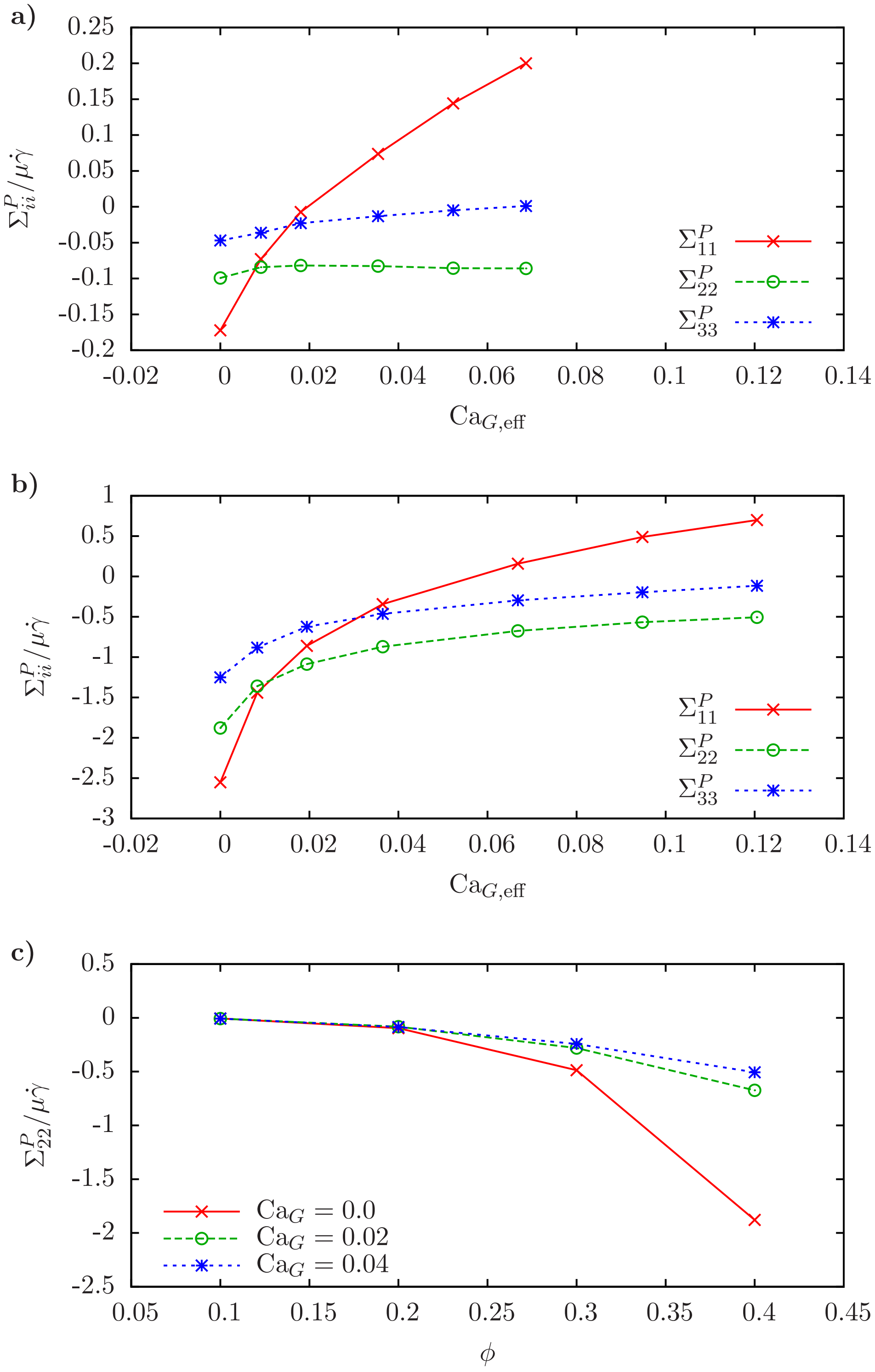

Figure 52: Behavior of individual normal-stress components for a suspension of deformable capsules at (a) 20% and (b) 40% volume fractions; (c) the relationship between volume fraction and Σ^p_{22} at several capillary numbers.

stress of region 2 is half that of region 1. Assuming $\phi = 0.4$ in region 1, constant Σ^p_{22} is maintained when $\phi \approx 0.33$ in region 2, as estimated from Figure 52c. When deformation is introduced, increasing the shear rate also increases deformation, thus, $\Sigma^p_{22}/\mu\dot{\gamma}$ is read from adjacent curves at larger capillary numbers, all of which represent a more rapid decrease in normal stress than maintaining rigid behavior. Thus, a smaller deviation in volume fraction is necessary to create the matching conditions in Σ^p_{22}, i.e., particle deformation reduces normal-stress driven migration. It is worth mentioning that modeling concentration distributions using the suspension balance model breaks down in regions of no shear, such as the centerline in pressure-driven channel flow (Nott & Brady, 1994). In this case $\dot{\gamma} \to 0$, which requires $\Sigma^p_{22} \to \infty$. Current models use a nonlocal formulation in a finite volume based on the typical particle length scale that avoids this behavior (Nott & Brady, 1994; Morris & Boulay, 1999).

Although the equilibrium balance in (81) is valid for suspensions of rigid spheres, macroscopic modeling of deformable capsule suspensions requires consideration of lift forces generated on deformed capsules, which have been attributed to both nonlinear shear-gradient effects in pressure-driven flow and to wall–capsule interactions (Coupier, Kaoui, Podgorski & Misbah, 2008). As a driving factor for creating concentration gradients, normal stresses decrease in importance as deformation increases; however, deformation-induced lift forces may create enhanced migration due to wall effects and nonlinear shear gradients. These topics need more investigation.

5.6 Particle diffusion

Several simulations have been performed for sufficient strains to obtain a preliminary investigation of particle self-diffusion. Particle diffusion is driven by the fluctuating nature of the particle interactions, which cause the particle trajectories to stochastically evolve. Particle self-diffusion, like any diffusive process, can be calculated by

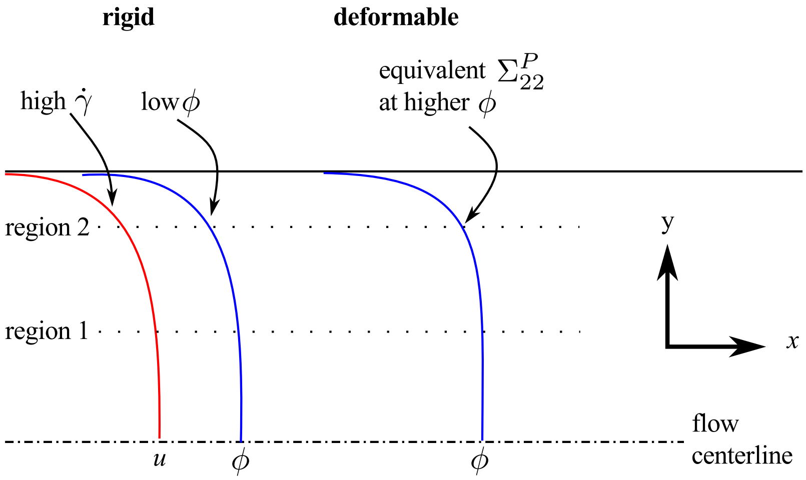

Figure 53: Schematic illustrating the effect of deformation on equilibrium particle concentrations in Poiseuille flow.

measuring the mean-squared displacements of the particle locations (Marchioro & Acrivos, 2001; Sierou & Brady, 2004), shown as

$$\langle \Delta y \Delta y \rangle \sim 2D_{yy}t, \tag{82}$$

where Δy is the y displacement and D_{yy} is the diffusion constant. A similar relationship holds for the z direction; however, the x direction diffusion must account for the affine displacements caused by the overall particle flow (Foss & Brady, 1999; Sierou & Brady, 2004). Diffusivities are nondimensionalized by $1/\dot{\gamma}a^2$. The diffusion constant exhibits both a short-time behavior that scales as t^2 (ballistic behavior), and a long-time diffusive behavior that scales as t, as shown in (82). Previous studies into the self-diffusivity of rigid spherical suspensions have shown that a large number of particles are required in order to achieve a reliable and convergent statistic for the diffusion tensor. The simulations in this thesis, with 285 particles, are on the lower end of the required number of particles, thus any results for $\mathbf{D}$ will be subject to high levels of uncertainty. Nevertheless, several qualitative observations can be made about the magnitude of the diffusion coefficient as particle deformation is increased.

The LB/FE method, when coupled with the LEbc, is subject to drifts in the mean particle velocity. A suspension using the LEbc has no source of momentum damping, thus any errors in force conservation persist indefinitely. The LB method itself is known to be subject to fluctuations in particle force at small time scales (Chun & Ladd, 2007; Wu & Aidun, 2009), and these fluctuations are largely caused by the discrete nature inherent in to the link-based LB method. For another source of fluctuation in the y-momentum, consider a particle straddling the LEbc that is under the influence of the volume controller as described in section 2. Since the lattice symmetry is disturbed, the number of links on either side of the LEbc is no longer in a one-to-one correspondence, thus a net drift in the particle location could be introduced. These drifts can be accounted for by defining the variance in particle displacements such that

$$\langle \Delta y \Delta y \rangle = \left\langle [y(t) - y(0)]^2 \right\rangle - \langle y(t) - y(0) \rangle^2 . \tag{83}$$

Figures 54(a and b) show the behavior of the y and z mean-squared displacements. Notice the short-time behavior that scales as t^2 and the long-time diffusive behavior that scales as t. Calculating the slope in the long-time regime yields the diffusion coefficient from (82), and the results have been tabulated in Table 7. For comparison, Sierou & Brady (2004) obtain diffusion coefficients of $D_{yy} = 0.0620 \pm 0.0060$ and $D_{zz} = 0.0290 \pm 0.0030$ for 40% volume fraction rigid spheres. More accurate results from the LB/FE method will require more particles and ensemble averaging of many particle configurations. For all simulations, deformation caused a decrease in particle diffusivity, and $D_{yy} \leq D_{zz}$. Measurements of particle self-diffusivity are difficult to perform experimentally; however, researchers have reported some success (Eckstein, Bailey & Shapiro, 2006; Leighton & Acrivos, 1987; Breedveld, van den Ende, Bosscher, Jongschaap & Mellema, 2001a; Breedveld et al., 2001b, 2002). Large variations in the reported diffusivity exist in literature making quantitative comparisons difficult. Much of the deviation in experimental results has been attributed to the short times

Table 7: Diffusion coefficients for simulations of 285 capsules at 40% volume fraction.

$\mathbf{Ca}_{\boldsymbol{G},\mathrm{eff}}$	$\boldsymbol{D_{yy}}$	$\boldsymbol{D_{zz}}$
0.0	0.046	0.035
0.01	0.038	0.024
0.07	0.018	0.015
0.12	0.014	0.014

(less than 10 strain units) measured (Sierou & Brady, 2004). This time, as seen in Figures 54(a and b), is still within the transition region before true diffusive behavior has been established.

There exists a subtle connection between self-diffusion and particle migration. In the initial formulation of the suspension balance model, Nott & Brady (1994) introduced the concept of a suspension "temperature", $T \sim \langle \boldsymbol{u}' \cdot \boldsymbol{u}' \rangle$, where $\boldsymbol{u}'$ is the fluctuational velocity associated with the interparticle interactions. This temperature is then used in a modeling equation for the particle pressure. The suspension temperature is directly related to the diffusion coefficient via the velocity autocorrelation function (Nott & Brady, 1994)

$$D \equiv \int_0^\infty \langle \boldsymbol{u}'(0) \cdot \boldsymbol{u}'(t) \rangle \, dt \sim aT^{1/2}. \tag{84}$$

In the diffusive-flux model (Phillips et al., 1992), in which particle migration is attributed to gradients in the diffusion, the authors argue that the underlying mechanism driving migration is the relative imbalance of particle interactions on either side of the particle, which would be seen in situations where the diffusion changes on the particle length scale (Leighton & Acrivos, 1987).

The results reported here echo these arguments. The diffusion tensor shows a systematic decrease as particle deformation in introduced; consequently, a reduction in compressive particle normal stresses are seen as deformation is introduced. Also, just as the isotropic formulation of suspension temperature is shown to be inadequate and an anisotropic description of the normal stresses is required (Morris & Boulay,

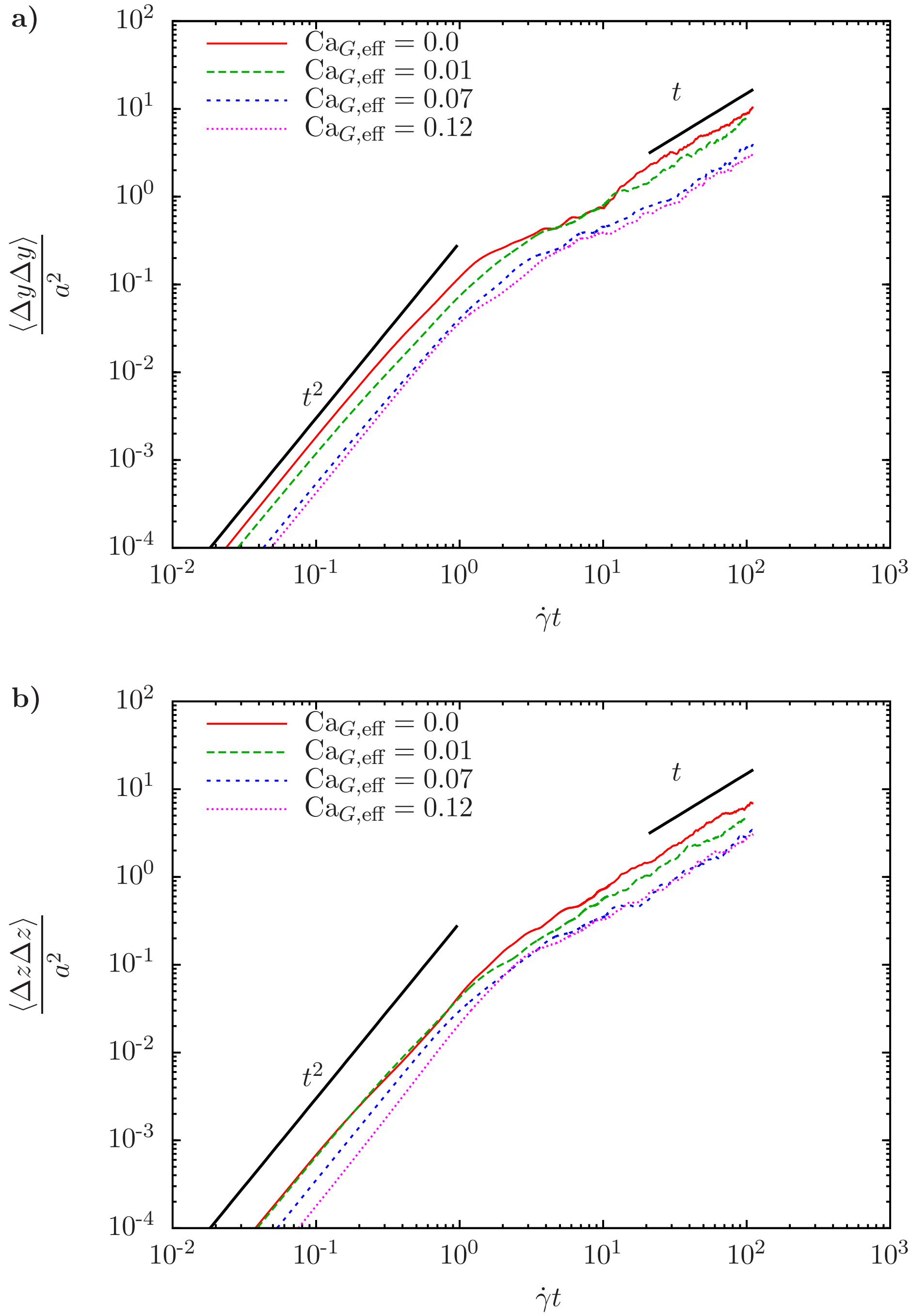

Figure 54: Mean-squared displacements of the particle position as a function of time for the (a) shear-gradient direction (y) and the (b) vorticity direction (z). At long time scales particles show linear growth of displacement variance in contrast to the short time quadratic growth.

1999), the diffusion tensor is also anisotropic. The relative magnitudes of Σ_{22}^{p} and D_{yy} are greater than Σ_{33}^{p} and D_{zz}, respectively.

CHAPTER VI

CONCLUSIONS AND FUTURE WORK

Particle suspensions are ubiquitous in many industrial and biological processes, and understanding the physical mechanisms which govern these flows is important for many commercial, industrial, and health businesses. A subset of suspensions exist in which deformation of the solid phase creates changes in the suspension rheology. Two areas of particular interest include those of papermaking, in which deformation of wood fibers creates changes in the rheology of paper slurries, and those of blood flow, in which deformation of red blood cells causes non-Newtonian changes in the rheology of flowing blood.

In order to study suspensions of deformable particles, a robust hybrid computational method is created that combines a lattice-Boltzmann (LB) fluid solver with a finite element (FE) solver for the dynamics of the suspended phase. This method was originally developed using a LB fluid code created within the research group with the help of former colleague Robert MacMeccan, and is capable of simulating hundreds of deformable particles on shared-memory computers. This method is validated with a number of model problems as described in chapter 2, MacMeccan (2007), and MacMeccan et al. (2009). Capabilities for distributed-memory computations have been added using the Message Passing Interface (MPI) constructs, and scalability is demonstrated on world-class computational clusters including the BlueGene/P installation at Argonne National Labs (Clausen et al., 2010).

Code structure relies on modular data structures and routines, thus allowing for future modifications on a unified code base that will be used by other researchers. For example, fluid and solid solvers communicate through boundary condition and geometry objects, thus a change in the solid model only requires a researcher to accurately update the state variables of the geometry object. Application of the boundary conditions remains standard. Current efforts by other members of the group using the unified code base include implementing the entropic LB method for high-Reynolds-number flows (Vahala, Keating, Soe, Yepez, Vahala & Ziegeler, 2009), alternative fluid–solid boundary conditions such as the external boundary force (Wu & Aidun, 2009, 2010), support for large FE objects such as porous media, and nonlinear models of red blood cell membrane mechanics (Dao, Li & Suresh, 2006). These additions will greatly increase the range of problems that this method is capable of simulating. Other areas of future work include improving the scaling, as the results in chapter 3 do not represent optimal scaling, and improving the data input/output procedures on a large numbers of processors.

A detailed investigation is performed to describe the rheology and microstructure of suspensions in both the dilute-limit case, and for densely concentrated suspensions. For the dilute case, significant results exist for the dynamics of fluid-filled capsules, and these results are used as a baseline for the LB/FE simulation. Analytical methods typically rely on asymptotic expansions in the limit of small deformation, and high deformation numerical models using Neo-Hookean membrane models are also included. Rheology measurements did exist; however, an accurate description of the dilute-limit rheology was incomplete because proper consideration of the isotropic contribution, i.e., the particle pressure, was not made. As deformation increases, a positive first normal stress difference, a negative second normal stress difference, and a negative (tensile) particle pressure are recovered in the dilute limit. The strong positive first normal stress is a direct result of the tensile forces present inside the capsule as it orients in the flow direction. In an effort to analytically model these effects, an extension of the results of Roscoe (1967) for an ellipsoidal body tank-treading in shear flow is made. This extension uses the previously neglected terms from Jeffery's (1922) solution to properly recover all normal stress components. It is worth noting that dilute slender-body rheological theory does not account for the particle pressure term that is a function of the particle's orientation (see for example Hinch & Leal, 1972). Deviations in the average orientation from $\theta = 0$ will generate changes in particle pressure for rigid, orientable objects.

For a dense suspension, a parameter sweep is conducted of the volume fraction and deformation. All capsules are taken to be fluid filled with the same fluid internal and external to the capsules. For dense rigid suspensions, the LB/FE method yields results that agree well with existing numerical and experimental results. Accurate resolution of the particle pressure requires several modifications to the LB/FE method to account for Galilean errors and the pseudo-compressible nature of the LB method. One caveat to the LB/FE method, however, is the relatively large interparticle repulsive force necessary due to the FE mesh link-based subgrid modeling. This force alters the suspension viscosity most dramatically, as large dissipative lubrication forces associated with small gaps are suppressed. Nevertheless, the LB/FE results fall within the large deviations in results seen experimentally. The role of interparticle forces remains an open area of investigation.

Deformation of the suspended phase induces rapid changes in the suspension rheology. Suspensions show a shear-thinning behavior, an effect also seen in biological flows of deformable red blood cells and in emulsions of deformable droplets. The shear-thinning behavior is also seen at the dilute limit; however, the dilute and dense behaviors are qualitatively different. Dilute shear thinning is driven by changes in the single-body microstructure, i.e., shape changes to the capsule, and shows a gradual onset. Conversely, shear thinning in dense suspensions shows a rapid onset at even mild deformations. Changes in rheology due to deformation cannot be explained by single-particle effects and must include changes to interparticle interactions. In a sense, at small deformations the elasticity of the particles augment the interparticle force creating softer interactions. A rapid sign change in the first normal stress difference is seen as the deformation increased. Although the same qualitative behavior is seen in the dilute limit, the rapidity of the increase cannot be explained looking at single-body changes in microstructure. Changes to the second normal stress are somewhat inconclusive, but the particle pressure shows a decrease as particle deformation increased.

Both the single-body and configurational microstructure are examined for these suspensions. The single-body microstructure, as quantified by the Taylor deformation parameter and orientation angle, is a weak function of the volume concentration. Since the single-body microstructure exhibits such a weak dependence on the volume fraction, qualitative changes in rheological behavior between dilute and rigid cases cannot be explained entirely through analysis of the single-body microstructure; therefore the pair-distribution function is used to study changes in configurational microstructure. Qualitatively, projections of the pair-distribution function show the "softening" of particle interactions and a notable asymmetry at very small deformations. In the rigid case, this asymmetry is the cause of normal stress differences. Rapid changes in particle configuration are also generated by deformation, which implies a significant rheological change driven by deformation-induced configuration changes. Quantitatively, using the pair-distribution for deformable capsule suspensions becomes difficult owing to the nonspherical and changing particle border. In contrast to rigid suspensions, where changes in the pair-distribution function are evaluated at small radii ($2 < r < 2.001$), large radial ranges must be considered in the deformable case. Deformation appears to reduce asymmetry, and in general reduces the increased likelihood of finding nearest and next-nearest neighbors. In the pair distribution function, the net effect is a homogenization of the configurational probability.

A qualitative investigation into the effects of deformation on particle migration is made. For deformable particles, changes in shear, deformation, and volume concentration are all strongly coupled. Thus, investigations into migration require traversing the parameter space spanned by ϕ, Ca_G, and $\dot{\gamma}$. Deformation decreases the magnitude of the shear-gradient and vorticity normal stresses, which serves to counterbalance the increase caused by higher shear. Consequently, deformation serves to suppress normal-stress-driven particle migration. Verifying this effect will require large-scale simulations in more realistic flow conditions. Furthermore, wall effects and deformation-induced lift forces could obscure normal-stress-driven migration, and one must account for these effects. Future development of constitutive models would be useful for macroscopic modeling of deformable particle suspensions.

The influence of deformation on particle self-diffusion is evaluated for the shear-gradient and vorticity directions at 40% concentration. This investigation is preliminary, and larger simulations are required to achieve accurate and quantitative results; however, some observations can be made. In general, deformation suppresses self-diffusion of the particle phase; consequently, the fluctuating velocity of the particles is less as deformation increased. The reduced fluctuation of the particles corresponds to a reduction of compressive forces in the particle phase, i.e., the suspension temperature is reduced with the addition of deformation. The relative magnitude of the shear-gradient and vorticity components of the diffusion tensor agree with the relative magnitude of the normal forces; higher diffusivities correspond with higher compressive stresses.

This thesis represents a fundamental study into the rheology of initially spherical, fluid-filled, deformable capsules in shear flow. Spherical capsules represent one of the simplest deformable particles, yet many questions remain. Some of these questions have been examined for isolated capsules but remain unknown in dense suspensions: What are the effects of nonlinear membrane models that may include significant amounts of bending stiffness? What are the effects of nonspherical equilibrium particle shapes, including the biconcave shape of the red blood cell or slender body effects of paper fibers? What are the effects of varying the internal fluid viscosity? This study is constrained to studying suspensions in linear shear. What are the effects of different flow fields, particularly extensional flow? Supercomputing speeds and computational methodologies have advanced enough that meaningful simulations can be performed on suspensions with a complex particle shapes and material properties. The flexible, parallel, and extensible FE/LB method developed in this thesis should be a useful tool for answering these questions.

REFERENCES

Aarts PA, Van Den Broek SA, Prins GW, Kuiken GD, Sixma JJ, Heethaar RM. 1988. Blood platelets are concentrated near the wall and red blood cells, in the center in flowing blood. *Arterioscler., Thromb., Vasc. Biol.* 8:819

Acrivos A, Mauri R, Fan X. 1993. Shear-induced resuspension in a Couette device. *Int. J. Multiphas. Flow* 19:797–802

Aidun CK, Clausen JR. 2010. The lattice-Boltzmann method for complex flows. *Annu. Rev. Fluid Mech.* 42:439–72

Aidun CK, Lu Y. 1995. Lattice Boltzmann simulation of solid particles suspended in fluid. *J. Stat. Phys.* 81:49–61

Aidun CK, Lu Y, Ding EJ. 1998. Direct analysis of particulate suspensions with inertia using the discrete Boltzmann equation. *J. Fluid Mech.* 373:287–311

Bagchi P. 2007. Mesoscale simulation of blood flow in small vessels. *Biophys. J.* 92:1858–77

Barthès-Biesel D. 1980. Motion of a spherical microcapsule freely suspended in a linear shear flow. *J. Fluid Mech.* 100:831–53

Barthès-Biesel D, Diaz A, Dhenin E. 2002. Effect of constitutive laws for two-dimensional membranes on flow-induced capsule deformation. *J. Fluid Mech.* 460:211–22

Barthès-Biesel D, Rallison J. 1981. The time-dependent deformation of a capsule freely suspended in a linear shear flow. *J. Fluid Mech.* 113:251–67

Batchelor GK. 1970. The stress system in a suspension of force-free particles. *J. Fluid Mech.* 41:545–70

Batchelor GK, Green JT. 1972a. The determination of the bulk stress in a suspension of spherical particles to order c^2. *J. Fluid Mech.* 56:401–27

Batchelor GK, Green JT. 1972b. The hydrodynamic interaction of two small freely-moving spheres in a linear flow field. *J. Fluid Mech.* 56:375–400

Bathe K. 1996. *Finite Element Procedures.* Englewood Cliffs, N.J. : Prentice Hall

Beaucourt J, Rioual F, Séon T, Biben T, Misbah C. 2004. Steady to unsteady dynamics of a vesicle in a flow. *Phys. Rev. E* 69:011906

Biben T, Misbah C. 2003. Tumbling of vesicles under shear flow within an advected-field approach. *Phys. Rev. E* 67:031908

Bouzidi M, Firdaouss M, Lallemand P. 2001. Momentum transfer of a Boltzmann-lattice fluid with boundaries. *Phys. Fluids* 13:3452

Brady JF, Bossis G. 1988. Stokesian Dynamics. *Annu. Rev. Fluid Mech.* 20:111–57

Brady JF, Morris JF. 1997. Microstructure of strongly sheared suspensions and its impact on rheology and diffusion. *J. Fluid Mech.* 348:103–39

Breedveld V, van den Ende D, Bosscher M, Jongschaap R, Mellema J. 2001a. Measuring shear-induced self-diffusion in a counterrotating geometry. *Phys. Rev. E* 63:21403

Breedveld V, van den Ende D, Bosscher M, Jongschaap R, Mellema J. 2002. Measurement of the full shear-induced self-diffusion tensor of noncolloidal suspensions. *J. Chem. Phys.* 116:10529–10535

Breedveld V, van den Ende D, Jongschaap R, Mellema J. 2001b. Shear-induced diffusion and rheology of noncolloidal suspensions: Time scales and particle displacements. *J. Chem. Phys.* 114:5923

Breyiannis G, Pozrikidis C. 2000. Simple shear flow of suspensions of elastic capsules. *Theor. Comput. Fluid Dyn.* 13:327–347

Buxton G, Verberg R, Jasnow D, Balazs A. 2005. Newtonian fluid meets an elastic solid: Coupling lattice Boltzmann and lattice-spring models. *Phys. Rev. E* 71:56707

Caiazzo A, Junk M. 2008. Boundary forces in lattice Boltzmann: Analysis of momentum exchange algorithm. *Comput. Math. Appl.* 55:1415–23

Chen H, Chen S, Matthaeus WH. 1992. Recovery of the Navier-Stokes equations using a lattice-gas Boltzmann method. *Phys. Rev. A* 45:R5339–R5342

Chen H, Kandasamy S, Orszag SA, Shock R, Succi S, Yakhot V. 2003. Extended Boltzmann kinetic equation for turbulent flows. *Science* 301:633–6

Chen LB, Ackerson BJ, Zukoski CF. 1994. Rheological consequences of microstructural transitions in colloidal crystals. *J. Rheol.* 38:193–216

Chen S, Doolen GD. 1998. Lattice Boltzmann method for fluid flows. *Annu. Rev. Fluid Mech.* 30:329–64

Chun B, Ladd AJC. 2007. Interpolated boundary condition for lattice Boltzmann simulations of flows in narrow gaps. *Phys. Rev. E* 75:66705

Cichocki B, Jones R. 1998. Image representation of a spherical particle near a hard wall. *Physica. A* 258:273–302

Clausen JR, Aidun CK. 2009. Galilean invariance in the lattice-Boltzmann method and its effect on the calculation of rheological properties in suspensions. *Int. J. Multiphas. Flow* 35:307–11

Clausen JR, Aidun CK. 2010. Capsule dynamics and rheology in shear flow: Particle pressure and normal stress. *submitted to Phys. Fluids*

Clausen JR, Reasor DA, Aidun CK. 2010. Parallel performance of a lattice-Boltzmann/finite element cellular blood flow solver on the IBM Blue Gene/P architecture. *Comput. Phys. Commun.* 181:1013–20

Cornubert R, d'Humières D, Levermore. 1991. A Knudsen layer theory for lattice gases. *Physica D.* 47:241–259

Coupier G, Kaoui B, Podgorski T, Misbah C. 2008. Noninertial lateral migration of vesicles in bounded Poiseuille flow. *Phys. Fluids* 20:111702

Cox RG. 1969. The deformation of a drop in a general time-dependent fluid flow. *J. Fluid Mech.* 37:601–23

Cox RG. 1974. The motion of suspended particles almost in contact. *Int. J. Multiphas. Flow* 1:343–71

Danker G, Misbah C. 2007. Rheology of a dilute suspension of vesicles. *Phys. Rev. Lett.* 98:088104

Dao M, Li J, Suresh S. 2006. Molecularly based analysis of deformation of spectrin network and human erythrocyte. *Mater. Sci. Eng. C* 26:1232–44

de Haas KH, Blom C, van den Ende D, Duits MHG, Mellema J. 1997. Deformation of giant lipid bilayer vesicles in shear flow. *Phys. Rev. E* 56:7132–7

Deboeuf A, Gauthier G, Martin J, Yurkovetsky Y, Morris JF. 2009. Particle pressure in a sheared suspension: A bridge from osmosis to granular dilatancy. *Phys. Rev. Lett.* 102:108301

d'Humières D, Ginzburg I, Krafczyk M, Lallemand P, Luo LS. 2002. Multiple-relaxation-time lattice Boltzmann models in three dimensions. *Phil. Trans. R. Soc. Lond. A* 360:437–51

Ding EJ, Aidun CK. 2003. Extension of the lattice-Boltzmann method for direct simulation of suspended particles near contact. *J. Stat. Phys.* 112:685–708

Doddi SK, Bagchi P. 2009. Three-dimensional computational modeling of multiple deformable cells flowing in microvessels. *Phys. Rev. E* 79:46318

Drew DA, Lahey RT. 1993. Analytical modelling of multiphase flow. In *Particulate two-phase flows*, ed. MC Roco. Oxford: Butterworth-Heinemann

Dupin MM, Halliday I, Care CM, Alboul L, Munn LL. 2007. Modeling the flow of dense suspensions of deformable particles in three dimensions. *Phys. Rev. E* 75:66707

Dupin MM, Halliday I, Care CM, Munn LL. 2008. Lattice Boltzmann modelling of blood cell dynamics. *Int. J. Comp. Fluid D.* 22:481–492

Eckstein EC, Bailey DG, Shapiro AH. 2006. Self-diffusion of particles in shear flow of a suspension. *J. Fluid Mech.* 79:191–208

Eggleton CD, Popel AS. 1998. Large deformation of red blood cell ghosts in a simple shear flow. *Phys. Fluids* 10:1834–1845

Eilers H. 1941. Die viskosität von emulsionen hochviskoser stoffe als funktion der konzentration. *Colloid Polym. Sci.* 97:313–21

Einstein A. 1906. Zur theorie der brownschen bewegung. *Ann. Phys.(Leipzig)* 19:371–381

Einstein A. 1911. Berichtigung zu meiner arbeit: Eine neue bestimmung der moleküldimensionen. *Ann. Phys. (Leipzig)* 34:591–592

Ethier C. 2002. Computational Modeling of mass transfer and links to atherosclerosis. *Ann. Biomed. Eng.* 30:461–71

Feng ZG, Michaelides EE. 2004. The immersed boundary-lattice Boltzmann method for solving fluid–particles interaction problems. *J. Comput. Phys.* 195:602–28

Foss DR, Brady JF. 1999. Self-diffusion in sheared suspensions by dynamic simulation. *J. Fluid Mech.* 401:243–74

Foss DR, Brady JF. 2000. Structure, diffusion and rheology of Brownian suspensions by Stokesian Dynamics simulation. *J. Fluid Mech.* 407:167–200

Freund JB. 2007. Leukocyte margination in a model microvessel. *Phys. Fluids* 19:023301

Frisch U, d'Humières D, Hasslacher B, Lallemand P, Pomeau Y, Rivet JP. 1987. Lattice gas hydrodynamics in two and three dimensions. *Complex Syst.* 1:649–707

Gadala-Maria F. 1979. *The rheology of concentrated suspensions.* Ph.D. thesis, PhD thesis, Standford University

Ginzbourg I, Adler P. 1994. Boundary flow condition analysis for the 3-dimensional lattice Boltzmann model. *J. Phys. II* 4:191–214

Goddard J, Miller C. 1967. Nonlinear effects in the rheology of dilute suspensions. *J. Fluid Mech.* 28:657–673

Higuera FJ, Jimenez J. 1989. Boltzmann approach to lattice gas simulations. *Europhys. Lett.* 9:663–68

Hinch EJ, Leal LG. 1972. The effect of Brownian motion on the rheological properties of a suspension of non-spherical particles. *J. Fluid Mech.* 52:683–712

Hinch EJ, Leal LG. 1973. Time-dependent shear flows of a suspension of particles with weak Brownian rotations. *J. Fluid Mech.* 57:753–67

Hoffman RL. 1972. Discontinuous and dilatant viscosity behavior in concentrated suspensions. I. Observation of a flow instability. *J. Rheol.* 16:155–73

Hofman JMA, Clercx HJH, Schram PPJM. 1999. Hydrodynamic interactions in colloidal crystals - (II). Application to dense cubic and tetragonal arrays. *Physica A* 268:353–390

Hofman JMA, Clercx HJH, Schram PPJM. 2000. Effective viscosity of dense colloidal crystals. *Phys. Rev. E* 62:8212–33

Jeffery GB. 1922. The motion of ellipsoidal particles immersed in a viscous fluid. *Proc. R. Soc. Lond. A* 102:161–79

Jeffrey D, Onishi Y. 1984. Calculation of the resistance and mobility functions for two unequal rigid spheres in low-reynolds-number flow. *J. Fluid Mech.* 139:261–290

Jeffrey DJ, Morris JF, Brady JF. 1993. The pressure moments for two rigid spheres in low-Reynolds-number flow. *Phys. Fluids A* 5:2317–25

Junk M, Klar A, Luo LS. 2005. Asymptotic analysis of the lattice Boltzmann equation. *J. Comput. Phys.* 210:676–704

Junk M, Yang Z. 2005. One-point boundary condition for the lattice Boltzmann method. *Phys. Rev. E* 72:66701

Junk M, Yong W. 2003. Rigorous Navier–Stokes limit of the lattice Boltzmann equation. *Asymptotic Anal.* 35:165–85

Kantsler V, Steinberg V. 2005. Orientation and dynamics of a vesicle in tank-treading motion in shear flow. *Phys. Rev. Lett.* 95:258101

Kantsler V, Steinberg V. 2006. Transition to tumbling and two regimes of tumbling motion of a vesicle in shear flow. *Phys. Rev. Lett.* 96:036001

Karniadakis G, Beskok A. 2005. *Microflows and Nanoflows: Fundamentals and Simulation.* New York: Springer

Keating B, Vahala G, Yepez J, Soe M, Vahala L. 2007. Entropic lattice Boltzmann representations required to recover Navier–Stokes flows. *Phys. Rev. E* 75:036712

Keller SR, Skalak R. 1982. Motion of a tank-treading ellipsoidal particle in a shear flow. *J. Fluid Mech.* 120:27–47

Kessler S, Finken R, Seifert U. 2008. Swinging and tumbling of elastic capsules in shear flow. *J. Fluid Mech.* 605:207–26

Kim S, Karilla S. 1991. *Microhydrodynamics: Principles and Selected Applications.* Boston: Butterworth-Heinemann

Kim SH, Pitsch H, Boyd ID. 2008. Accuracy of higher-order lattice Boltzmann methods for microscale flows with finite Knudsen numbers. *J. Comput. Phys.* 227:8655–71

Konstantopoulos K, Kukreti S, McIntire LV. 1998. Biomechanics of cell interactions in shear fields. *Adv. Drug Deliver. Rev.* 33:141–64

Krieger IM, Dougherty TJ. 1959. A mechanism for non-Newtonian flow in suspensions of rigid spheres. *J. Rheol.* 3:137–52

Kulkarni PM, Morris JF. 2008. Suspension properties at finite Reynolds number from simulated shear flow. *Phys. Fluids* 20:040602

Ladd AJC. 1994a. Numerical simulations of particulate suspensions via a discretized Boltzmann equation. Part 1. Theoretical foundation. *J. Fluid Mech.* 271:285–309

Ladd AJC. 1994b. Numerical simulations of particulate suspensions via a discretized Boltzmann equation. Part 2. Numerical results. *J. Fluid Mech.* 271:311–39

Ladd AJC, Verberg R. 2001. Lattice-Boltzmann simulations of particle-fluid suspensions. *J. Stat. Phys.* 104:1191–251

Lallemand P, Luo LS. 2003. Lattice Boltzmann method for moving boundaries. *J. Comput. Phys.* 184:406–21

Lees AW, Edwards SF. 1972. The computer study of transport processes under extreme conditions. *J. Phys. C* 5:1921–8

Leighton D, Acrivos A. 1986. Viscous resuspension. *Chem. Eng. Sci.* 41:1377–84

Leighton DT, Acrivos A. 1987. The shear-induced migration of particles in concentrated suspensions. *J. Fluid Mech.* 181:415–39

Lishchuk SV, Halliday I, Care CM. 2006. Shear viscosity of bulk suspensions at low Reynolds number with the three-dimensional lattice Boltzmann method. *Phys. Rev. E* 74:017701

Lloyd-Jones D, Adams R, Carnethon M, De Simone G, Ferguson T, et al. 2009. Heart Disease and Stroke Statistics–2009 Update. A Report From the American Heart Association Statistics Committee and Stroke Statistics Subcommittee. *Circulation* 119:e21

Loewenberg M. 1998. Numerical simulation of concentrated emulsion flows. *J. Fluid Eng. T. ASME* 120:824–32

Loewenberg M, Hinch E. 1996. Numerical simulation of a concentrated emulsion in shear flow. *J. Fluid Mech.* 321:395–419

MacMeccan R. 2007. *Mechanistic Effects of Erythrocytes on Platelet Deposition in Coronary Thrombosis*. Ph.D. thesis, Georgia Institute of Technology

MacMeccan RM, Clausen JR, Neitzel GP, Aidun CK. 2009. Simulating deformable particle suspensions using a coupled lattice-Boltzmann and finite-element method. *J. Fluid Mech.* 618:13–39

Mader M, Vitkova V, Abkarian M, Viallat A, Podgorski T. 2006. Dynamics of viscous vesicles in shear flow. *Eur. Phys. J. E* 19:389–97

Marchioro M, Acrivos A. 2001. Shear-induced particle diffusivities from numerical simulations. *J. Fluid Mech.* 443:101–128

McNamara GR, Zanetti G. 1988. Use of the Boltzmann equation to simulate lattice-gas automata. *Phys. Rev. Lett.* 61:2332–5

Mei R, Yu D, Shyy W, Luo LS. 2002. Force evaluation in the lattice Boltzmann method involving curved geometry. *Phys. Rev. E* 65:041203

Mewis J, Frith W, Strivens T, Russel W. 1989. The rheology of suspensions containing polymerically stabilized particles. *AIChE J.* 35:415–422

Misbah C. 2006. Vacillating breathing and tumbling of vesicles under shear flow. *Phys. Rev. Lett.* 96:028104

Miyamura A, Iwasaki S, Ishii T. 1981. Experimental wall correction factors of single solid spheres in triangular and square cylinders, and parallel plates. *Int. J. Multiphas. Flow* 7:41–46

Möller T, Trumbore B. 1997. Fast, minimum storage ray-triangle intersection. *Journal of Graphics Tools* 2:21–28

Morris JF. 2009. A review of microstructure in concentrated suspensions and its implications for rheology and bulk flow. *Rheol. Acta* 48:909–23

Morris JF, Boulay F. 1999. Curvilinear flows of noncolloidal suspensions: The role of normal stresses. *J. Rheol.* 43:1213–37

Morris JF, Brady JF. 1998. Pressure-driven flow of a suspension: Buoyancy effects. *Int. J. Multiphas. Flow* 24:105–30

Morris JF, Katyal B. 2002. Microstructure from simulated brownian suspension flows at large shear rate. *Phys. Fluids* 14:1920–37

Nannelli F, Succi S. 1992. The lattice Boltzmann equation on irregular lattices. *J. Stat. Phys.* 68:401–7

Nguyen NQ, Ladd AJC. 2002. Lubrication corrections for lattice-Boltzmann simulations of particle suspensions. *Phys. Rev. E* 66:046708

Noble DR, Chen S, Georgiadis JG, Buckius RO. 1995. A consistent hydrodynamic boundary condition for the lattice Boltzmann method. *Phys. Fluids* 7:203–9

Nott PR, Brady JF. 1994. Pressure-driven suspension flow: Simulation and theory. *J. Fluid Mech.* 275:157–99

Nourgaliev RR, Dinh TN, Theofanous TG, Joseph D. 2003. The lattice Boltzmann equation method: theoretical interpretation, numerics and implications. *Int. J. Multiphas. Flow* 29:117–69

Nunan K, Keller J. 1984. Effective viscosity of a periodic suspension. *J. Fluid Mech.* 142:269–287

Onoda GY, Liniger EG. 1990. Random loose packings of uniform spheres and the dilatancy onset. *Phys. Rev. Lett.* 64:2727–30

Pal R. 2003. Rheology of concentrated suspensions of deformable elastic particles such as human erythrocytes. *J. Biomech.* 36:981–9

Papir Y, Krieger I. 1970. Rheological studies on dispersions of uniform colloidal spheres:: II. Dispersions in nonaqueous media. *J. Colloid. Interf. Sci.* 34:126–30

Parsi F, Gadala-Maria F. 1987. Fore-and-aft asymmetry in a concentrated suspension of solid spheres. *J. Rheol.* 31:725–32

Peskin CS. 2002. The immersed boundary method. *Acta Num.* 11:479–517

Phillips RJ, Armstrong RC, Brown RA, Graham AL, Abbott JR. 1992. A constitutive equation for concentrated suspensions that accounts for shear-induced particle migration. *Phys. Fluids A* 4:30–40

Phung T. 1993. *Behavior of concentrated colloidal suspensions by Stokesian Dynamics simulation.* Ph.D. thesis, PhD thesis, Californian Institute of Technology

Phung TN, Brady JF, Bossis G. 1996. Stokesian Dynamics simulation of Brownian suspensions. *J. Fluid Mech.* 313:181–207

Pozrikidis C. 1993. On the transient motion of ordered suspensions of liquid drops. *J. Fluid Mech.* 246:301–320

Pozrikidis C. 1995. Finite deformation of liquid capsules enclosed by elastic membranes in simple shear flow. *J. Fluid Mech.* 297:123–52

Prasad D, Kytömaa HK. 1995. Particle stress and viscous compaction during shear of dense suspensions. *Int. J. Multiphas. Flow* 21:775–85

Ramanujan S, Pozrikidis C. 1998. Deformation of liquid capsules enclosed by elastic membranes in simple shear flow: large deformations and the effect of fluid viscosities. *J. Fluid Mech.* 361:117–43

Roscoe R. 1967. On the rheology of a suspension of viscoelastic spheres in a viscous liquid. *J. Fluid Mech.* 28:273–93

Seifert U. 1999. Fluid membranes in hydrodynamic flow fields: Formalism and an application to fluctuating quasispherical vesicles in shear flow. *Eur. Phys. J. B* 8:405–15

Senff H, Richtering W. 1999. Temperature sensitive microgel suspensions: Colloidal phase behavior and rheology of soft spheres. *J. Chem. Phys.* 111:1705–1711

Sierou A, Brady JF. 2001. Accelerated stokesian dynamics simulations. *J. Fluid Mech.* 448:115–46

Sierou A, Brady JF. 2002. Rheology and microstructure in concentrated noncolloidal suspensions. *J. Rheol.* 46:1031–56

Sierou A, Brady JF. 2004. Shear-induced self-diffusion in non-colloidal suspensions. *J. Fluid Mech.* 506:285–314

Singh A. 2000. *Rheology of non-colloidal suspensions.* Ph.D. thesis, Indian Institute of Science, Bangalore, India

Singh A, Nott P. 2003. Experimental measurements of the normal stresses in sheared Stokesian suspensions. *J. Fluid Mech.* 490:293–320

So JH, Yang SM, Hyun JC. 2001. Microstructure evolution and rheological responses of hard sphere suspensions. *Chem. Eng. Sci.* 56:2967–77

Stickel JJ, Powell RL. 2005. Fluid Mechanics and Rheology of Dense Suspensions. *Annu. Rev. Fluid Mech.* 37:129–49

Succi S. 2001. *The lattice Boltzmann Equation for Fluid Dynamics and Beyond.* Oxford: Clarendon Press; New York: Oxford University Press

Sui Y, Chew YT, Low HT. 2007a. A lattice Boltzmann study on the large deformation of red blood cells in shear flow. *Int. J. Mod. Phys. C* 18:993–1011

Sui Y, Chew YT, Roy P, Chen XB, Low HT. 2007b. Transient deformation of elastic capsules in shear flow: Effect of membrane bending stiffness. *Phys. Rev. E* 75:066301

Sui Y, Chew YT, Roy P, Low HT. 2008. A hybrid method to study flow-induced deformation of three-dimensional capsules. *J. Comput. Phys.* 227:6351–6371

Tarbell JM. 2003. Mass transport in arteries and the localization of atherosclerosis. *Annu. Rev. Biomech. Eng.* 5:79–118

Vahala G, Keating B, Soe M, Yepez J, Vahala L, Ziegeler S. 2009. Entropic, LES and boundary conditions in lattice Boltzmann simulations of turbulence. *Eur. Phys. J. Special Topics* 171:167–71

Vahala G, Keating B, Soe M, Yepez J, Vahala L, et al. 2008. MHD turbulence studies using lattice Boltzmann algorithms. *Commun. Comput. Phys.* 4:624–46

Vlahovska PM, Gracia RS. 2007. Dynamics of a viscous vesicle in linear flows. *Phys. Rev. E* 75:16313

Wagner AJ, Pagonabarraga I. 2002. Lees–Edwards boundary conditions for lattice Boltzmann. *J. Stat. Phys.* 107:521–37

Wagner AJ, Yeomans JM. 1999. Phase separation under shear in two-dimensional binary fluids. *Phys. Rev. E* 59:4366–73

Wu J, Aidun CK. 2009. Simulating 3D deformable particle suspensions using lattice Boltzmann method with discrete external boundary force. *Int. J. Numer. Meth. Fluids* 62:765–83

Wu J, Aidun CK. 2010. A method for direct simulation of flexible fiber suspensions using lattice-Boltzmann equation with external boundary force. *Int. J. Multiphas. Flow* 36:202–9

Young W, Budynas R. 2002. *Roark's Formulas for Stress and Strain.* McGraw-Hill

Yurkovetsky Y, Morris JF. 2008. Particle pressure in sheared Brownian suspensions. *J. Rheol.* 52:141–64

Zarraga I, Hill D, Leighton D. 2000. The characterization of the total stress of concentrated suspensions of noncolloidal spheres in Newtonian fluids. *J. Rheol.* 44:185–220

Ziegler DP. 1993. Boundary-conditions for lattice Boltzmann simulations. *J. Stat. Phys.* 71:1171–7

Zinchenko A, Davis R. 2000. An efficient algorithm for hydrodynamical interaction of many deformable drops. *J. Comput. Phys.* 157:539–587

Zinchenko A, Davis R. 2002. Shear flow of highly concentrated emulsions of deformable drops by numerical simulations. *J. Fluid Mech.* 455:21–62

Zuzovsky M, Adler P, Brenner H. 1983. Spatially periodic suspensions of convex particles in linear shear flows. III. Dilute arrays of spheres suspended in Newtonian fluids. *Phys. Fluids* 26:1714